Development of a standard test and calibration procedure for the hardware of the Radio Neutrino Detector RNO-G

Master's Thesis in Physics

Presented by
Nora Marie Feigl
December 16th, 2020

Experimental Astroparticle Physics -
Radiodetection of Neutrinos
Friedrich-Alexander-Universität Erlangen-Nürnberg

Supervisor: Prof. Dr. Anna Nelles

Contents

Contents I
List of Tables III
List of Figures V
List of Abbreviations IX

1 Introduction **1**

2 Radio Detection of Neutrinos and RNO-G **4**
2.1 General Physics Case 4
2.1.1 Ultra-High-Energy Neutrinos in Multi-Messenger Astrophysics 4
2.1.2 Cosmic Neutrino Production 7
2.1.3 Radio Emission of Neutrino Interactions 9
2.1.4 Radio Detection of Neutrinos in Ice 10
2.2 The Radio Neutrino Observatory in Greenland 11
2.2.1 Science Case 11
2.2.2 Experimental Design and Construction 12
2.2.3 Radio-Frequency Front-End Design 15

3 Theory of Electronic and Amplifier Properties **18**
3.1 S-Parameters 19
3.2 Gain 21
3.3 Group Delay 21
3.4 Crosstalk 22
3.5 Noise Figure 22
3.6 Temperature Dependence of Amplifiers 23

4 Measurements **25**
4.1 Data File Naming 26
4.2 Function Test and Stress Test 27
4.3 Performance Tests 29
4.3.1 S-Parameter Measurements 30
4.3.2 Gain Measurements 34
4.3.3 Group Delay Measurements 40
4.3.4 Crosstalk Measurements 45

4.3.5 Noise Figure Measurements 49
4.4 Testing Different Parameters and Components 50
4.4.1 Fiber Influence 51
4.4.2 Random Errors 52
4.4.3 IGLU Influence 54
4.5 Temperature Dependence 58
4.5.1 SURFACE Boards 59
4.5.2 DRABs and IGLU Boards 78

5 Summary and Conclusions **90**

6 Appendix **95**
6.1 Effects of the COVID-19 pandemic 95
6.2 Additional Figures 96

7 Bibliography **125**

List of Tables

4.1 File Naming: Temperature References 27
4.2 Calibration Settings 30
4.3 Frequency Sweep Settings 30
4.4 Noise Figure Settings 49
4.5 Temperature Dependence SURFACE Boards: Constant Factors . . 63
4.6 Temperature Dependence SURFACE Boards: Fit Functions 69
4.7 Temperature Dependence SURFACE Boards: 68 % Quantile 74
4.8 Temperature Dependence SURFACE Boards: Maximum Deviation . 77
4.9 Temperature Dependence DRABs: Fit Functions and 68 % Quantile 88

List of Figures

2.1 Multi-Messenger View of the High-Energy Universe 6
2.2 Cosmic Ray Energy Spectrum 7
2.3 Neutrino Induced Showers 10
2.4 Station Design 13
2.5 Amplifier Boards 15
2.6 SURFACE Board in Enclosure 16
2.7 IGLU Board in Enclosure 16
2.8 DRAB in Enclosure 17

3.1 Concept of S-Parameters 20

4.1 IGLU Function Test 29
4.2 S-Parameters of the SURFACE Boards (mag) 31
4.3 S-Parameters of the SURFACE Boards (dB) 32
4.4 S-Parameters of the DRABs (mag) 33
4.5 S-Parameters of the DRABs (dB) 34
4.6 Gain of SURFACE Boards (mag) 36
4.7 Gain of DRABs (mag) 37
4.8 Measurement of Amplifier Boards: Gain and Deviation 38
4.9 Gain of a SURFACE Board and Gain of a DRAB 39
4.10 Deviation from the Average: SURFACE Boards 41
4.11 Deviation from the Average: DRABs 42
4.12 Group Delay 43
4.13 Anti-Resonance 44
4.14 Crosstalk SURFACE Board Channel 2 46
4.15 Crosstalk DRAB Board Channel 2 47
4.16 Crosstalk DRAB Board Channel 4: Absorber Test 48
4.17 Noise Figure 50
4.18 Noise Figure (Chicago) 51
4.19 Fiber Influence: Gain and Group Delay 52
4.20 Fiber Influence: Gain 53
4.21 Random Error 54
4.22 IGLU Influence on Gain (dB) 55

4.23 IGLU Influence: Zoom on Gain Measurements . . . 56
4.24 Comparison of Different IGLUs . . . 57
4.25 Comparison of Different IGLUs . . . 58
4.26 Temperature Dependence SURFACE Boards (mag) . . . 60
4.27 Temperature Dependence SURFACE Boards (dB) . . . 61
4.28 Temperature Dependence: Constant Factor Search . . . 62
4.29 Temperature Dependence: Constant Factor . . . 64
4.30 Temperature Dependence: Deviation (Constant Factor) . . . 65
4.31 Temperature Dependence: Dynamic Factor . . . 67
4.32 Temperature Dependence: Deviation (Dynamic Factor) . . . 68
4.33 Temperature Dependence: Fit Functions . . . 70
4.34 SURFACE Boards: Fit Parameters a(T) and b(T) . . . 71
4.35 Temperature Dependence: Fit Functions . . . 72
4.36 Temperature Dependence: Deviation (Fit Function) . . . 73
4.37 Histograms: Deviation Comparison . . . 75
4.38 Histograms: Deviation Distribution . . . 76
4.39 Temperature Dependence DRAB and IGLU Board (mag) . . . 79
4.40 Temperature Dependence DRAB and IGLU Board (dB) . . . 80
4.41 DRAB or DRAB and Fiber Cooled Down . . . 81
4.42 IGLU or IGLU and Fiber Cooled Down . . . 82
4.43 DRAB, IGLU and Fiber Cooled Down . . . 83
4.44 Temperature Dependence DRABs: Fit Functions . . . 86
4.45 DRABs: Fit Parameters a(T) and b(T) . . . 87
4.46 Temperature Dependence DRABs: Deviation (Fit Function) . . . 89

5.1 Flow Chart: Standard Test Procedure . . . 94

6.1 Gain of SURFACE Boards (mag) . . . 96
6.2 Gain of DRABs (mag) . . . 97
6.3 Gain of DRABs (mag) . . . 98
6.4 Gain of DRABs (mag) . . . 99
6.5 Deviation from the Average: Surface Boards . . . 100
6.6 Deviation from the Average: Surface Boards . . . 101
6.7 Deviation from the Average: Surface Boards . . . 102
6.8 Deviation from the Average: DRABs . . . 103
6.9 Deviation from the Average: DRABs . . . 104
6.10 Deviation from the Average: DRABs . . . 105
6.11 Deviation from the Average: DRABs . . . 106
6.12 Deviation from the Average: DRABs . . . 107
6.13 Deviation from the Average: DRABs . . . 108
6.14 Deviation from the Average: DRABs . . . 109

6.15 Crosstalk Surface Board Channel 1 110
6.16 Crosstalk Surface Board Channel 3 111
6.17 Crosstalk Surface Board Channel 4 112
6.18 Crosstalk Surface Board Channel 5 113
6.19 Crosstalk DRAB Board Channel 1 114
6.20 Crosstalk DRAB Board Channel 3 115
6.21 Crosstalk DRAB Board Channel 4 116
6.22 Crosstalk DRAB Board Channel 1: Absorber Test 117
6.23 Crosstalk DRAB Board Channel 2: Absorber Test 118
6.24 Crosstalk DRAB Board Channel 3: Absorber Test 119
6.25 IGLU Influence: Gain (mag) 120
6.26 IGLU Cooled Down 121
6.27 IGLU Cooled Down 122
6.28 IGLU and Fiber Cooled Down 123
6.29 IGLU and Fiber Cooled Down 124

List of Abbreviations

AGN	Active Galactic Nuclei
ANITA	Antarctic Impulsive Transient Antenna
ARA	Askaryan Radio Array
ARIANNA	Antarctic Ross Ice Shelf Antenna Neutrino Array
CERN	European Organization for Nuclear Research (*Conseil Européen pour la Recherche Nucléaire*)
CMB	Cosmic Microwave Background
dB	decibel
DAQ	Data-Acquisition system
DRAB	Downhole Receiver and Amplifier Board
DUT	Device Under Test
F	noise factor
FSRQ	Flat Spectrum Radio Quasar
GRB	Gamma-Ray Burst
GZK	Greisen-Zatsepin-Kuzmin
H.E.S.S.	High Energy Stereoscopic System
Hpol	Horizontal polarized (antenna)
IceCube	IceCube Neutrino Observatory
IGLU	In-ice Gain with Low-power Unit
LHC	Large Hadron Collider
LNA	Low-Noise Amplifier
LPDA	Log-Periodic Dipole Antenna
MAGIC	Major Atmospheric Gamma Imaging Cherenkov Telescopes
NF	noise figure

RF	Radio Frequency
RFoF	Radio Frequency over Fiber
RICE	Radio Ice Cherenkov Experiment
RNO-G	Radio Neutrino Oberservatory in Greenland
S-parameters	Scattering-parameters
SNR	Signal to Noise Ratio
SURFACE board	No acronym. Full-chain amplification and filtering board
TA	Telescope Array
VNA	Vector Network Analyzer
Vpol	Vertical polarized (antenna)
γ**-ray**	Gamma-ray

1 Introduction

Every second more than 10^{12} neutrinos are passing through the body of every human without affecting them in any way [1]. Because of their low interaction rate neutrinos remained unknown for a long time. Neutrinos were proposed by Pauli to explain the beta decay. Since their first detection years later, many puzzles concerning these particles have been solved like the solar neutrino problem or if neutrinos have mass. Nowadays, neutrinos of various origins are studied by scientists around the world such as solar neutrinos, geoneutrinos and neutrinos from outside the solar system. The latter ones are supposed to help understand some of the most energetic events and objects in the universe.

During the search for the highest energies in the universe one comes across cosmic rays. The highest energy that particles in human made accelerators can reach is a maximum collision energy of 13 TeV ($13 \cdot 10^{12}$ eV) at the LHC at CERN [2] - while the energy of cosmic rays reaches far into the EeV range ($> 10^{20}$ eV) [3].

Cosmic rays were discovered more than 100 years ago: in 1912 Victor Hess measured the radiation in the atmosphere during balloon flights. The expectation was that the radiation would decrease at higher altitude due to the supposed origin of the radiation: the Earth's crust. But the opposite was the case - the data showed that the ionizing radiation increased with height, therefore the radiation is entering the atmosphere from above: Hess had discovered cosmic rays [4].

Their origin however is yet to be found. Neutrinos, which share their origins with cosmic rays, are supposed to play a crucial role in this search since they travel without deflection through the universe. With the observation of ultra-high-energy neutrinos the astronomical objects which produce cosmic rays could be revealed. The research field that approaches this search and began with Hess' discovery has developed into astroparticle physics.

Astroparticle physics is a field of research in physics located at the intersection of astrophysics and particle physics with the influences of other physical subfields. In astronomy celestial objects are observed through the electromagnetic rays they emit. In particle physics human-made accelerators are used to generate specific particles. In astroparticle physics detectors are build to observes particles related to astronomical objects. These particles can reach energies higher then those which have been accelerated in particle colliders on Earth, but the mechanisms of these accelerations are yet not fully understood.

To understand these mechanisms and to find the sources of cosmic rays, particles

from various parts of the universe are measured with different detector types all over the globe. From the hunt for cosmic rays near the Andes (Pierre Auger Observatory) [5] to the examination of γ-rays in the highland of Namibia (H.E.S.S.) [6] to the observation of neutrinos in the ice of the South Pole (IceCube Neutrino Observatory) [7] and many more.

Neutrinos as undeflected messengers of ultra-high-energy sources play an important role in astroparticle physics. For a long time, the search for high-energy neutrinos was mainly executed with optical detectors of increasing size. IceCube in particular has shaped neutrino astronomy in recent years. But with increasing energy, the flux of neutrinos becomes so small that even these giant detectors observe areas that are not large enough. To detect these ultra-high-energy neutrinos the detector scale would have to be about a hundred times larger than IceCubes' effective volume.

This means that a detection method is required that makes a detector of this size realistic - hardware and monetary wise. The radio emission of particle showers induced by fast travelling neutrinos in dense media provides the possibility of larger neutrino detectors than ever before. While the effect was predicted in the 1960s, technology had to improve for the first detectors to be built. The detection via radio emission promises to be an excellent method for measuring the properties of ultra-high-energy neutrinos. Radio detectors can be built nowadays with the necessary sensitivity to detect neutrinos. Laying the foundation for the first large, radio technique, low-threshold and in-ice detector to observe ultra-high-energy neutrinos: the Radio Neutrino Observatory in Greenland (RNO-G).

RNO-G will be able to detect the radio emission of neutrinos with energies above 10 PeV in the Greenland ice. The observatory is meant to play a unique role in multi-messenger astrophysics as a pathfinder project to detect the highest energy cosmic neutrinos. RNO-G will not only observe as first ultra-high-energy neutrino detector the Northern sky but also works as a pathfinder for the radio component of the next-generation neutrino detector IceCube-Gen2.

The deployment of the first of the overall 35 stations of RNO-G starts in summer 2021. Much of the hardware was tested in spring and summer 2020. For the effects of the COVID-19 pandemic on the tests performed for this thesis see section 6.1. Based on the experiences of the first stations the second generation of hardware will be improved and future detectors, such as IceCube-Gen2, can be designed with the knowledge and experience gained in the RNO-G project. So it is important to develop early on a reproducible and exact testing and calibration procedure to evaluate the performance of the detector stations.

In this master's thesis the development of a such a standard test and calibration procedure for the hardware of the radio neutrino detector RNO-G will be described. For that the three different types of amplifier boards, which will be used in the

detector, were tested with a vector network analyzer and in a temperature chamber. The thesis describes how the influence of different components, the characteristics and the variations of the boards were tested.

The thesis begins by describing the science case of RNO-G (chapter 2) and discussing the role of ultra-high-energy neutrinos in multi-messenger astrophysics. The radio emission of neutrino interactions in dense media is outlined and how this emission can be used to detect neutrinos in ice via the radio technique, as in the case of RNO-G. The detector setup and the hardware that were tested in this thesis are described. This is followed by chapter 3 in which the different measurements that were done to analyze the properties of the amplifier boards are explained. The interpretation of these properties like the reflection and transmission characteristics as well as the signal increase that the amplifiers provide are outlined. Additionally the origins of signal deformation are examined. The structure of the next chapter (chapter 4) follows the four-phase test procedure it describes. All measurement results are discussed. First, a functionality test to check for broken boards and boards with insufficient temperature resistance was done. Then the performance of the boards was reviewed as well as the features and characteristics of the different board types were studied. After that the influence of different hardware components and parameters were investigated. The last tests focused on the temperature dependence of the measurements. The thesis finishes with a conclusion (chapter 5) in which the measurement results are summarized and an outlook on future tests is given.

2 Radio Detection of Neutrinos and RNO-G

To motivate the construction of the Radio Neutrino Observatory in Greenland, for which the hardware test in this thesis were performed, a general overview of the physics case explains the role of ultra-high-energy neutrinos in astroparticle physics and how they may help to answer questions about the high-energy universe. It will further be explained how these neutrinos can be measured on Earth and the detection principle and the design of the detector will be described.

2.1 General Physics Case

More than one hundred years after Hess discovered cosmic rays, astroparticle physics has grown into a research field dealing with many different questions like: What are the sources of ultra-high-energy cosmic rays and how does their production and acceleration work? What is the relation of cosmic rays and the astrophysical neutrino flux? But high-energy neutrinos are not only useful messenger particles to study cosmic rays, they could also help to understand fundamental neutrino properties like whether neutrinos are stable [8], their flavors mixing [9] at high energies and the behavior of their cross sections [10] at high energies. As well as they might help with broader issues like the fundamental symmetries of nature [11], dark matter [12] or possible hidden interactions with cosmic backgrounds [13].

2.1.1 Ultra-High-Energy Neutrinos in Multi-Messenger Astrophysics

Neutrinos are electrically neutral fermions which only interact via the weak subatomic force and gravity. Since neutrinos are nearly massless and the weak force only works short range, neutrinos rarely interact. The characteristic low interaction cross-section of neutrinos makes their detection on one hand quite complicated but on the other hand it makes them ideal messenger particles. The term *ultra-high-energy neutrinos* is usually used to describe neutrinos with energies in the EeV-range and above [14]. In multi-messenger astrophysics the signals of cosmic

rays, gravitational waves, photons and neutrinos are detected and interpreted. *Cosmic rays* are charged high-energy particles originating from astronomical objects. Detecting these powerful messengers helps to answer questions concerning the high-energy universe.

The observation of cosmic rays bares the problem, that these particles interact on their way to Earth with magnetic fields, radiation and intervening matter and therefore they do not point back to their high-energy sources. Additionally cosmic rays of a certain energy get attenuated due to the *GZK-effect* (Greisen-Zatsepin-Kuzmin) (see section 2.1.2).

Gamma rays (γ-rays) from astronomical objects pose the difficulty that they can be created not only in cosmic accelerators but also by inverse Compton scattering and they can get attenuated when interacting with the cosmic microwave background (CMB).

Neutrinos play a vital role in the exploration of the high-energy universe since they do not get deflected in galactic and extra-galactic magnetic fields when traveling from their sources to Earth. They propagate unaffected through regions of the universe with considerable matter density. Therefore they can be used to identify ultra-high-energy sources since they point straight back to the accelerators they are produced in, even over huge distances. The disadvantages of neutrinos as messenger particles are their predicted rapidly falling flux at increasing energy and their tiny cross section.

The first coincident measurement of a source flaring in neutrinos and γ-rays was the blazar TXS 0506+056, measured in September 2017 [15, 16]. A PeV neutrino event detected by IceCube coincided with a γ-ray event measured by the Fermi Gamma-ray Space Telescope (Fermi) [18] and the Major Atmospheric Gamma Imaging Cherenkov Telescopes (MAGIC) [17] in a five day time-window. This multi-messenger event as well as the measurements of a diffuse astrophysical neutrino flux [19] along with the detection of some potential neutrino sources by IceCube have emphasized neutrinos as a crucial messenger.

So for source identification and the exploration of acceleration mechanisms neutrinos are needed as part of a broad multi-messenger observation program over a wide range of energy. Measurements of γ-rays by Fermi [20], cosmic rays by the Pierre Auger Observatory (Auger) [5] and neutrinos by the IceCube Neutrino Observatory (IceCube) [7] show spectra whose energy densities look strikingly alike (see figure 2.1). This indicates a common origin of these diffuse fluxes of different particles. The connecting mechanism is the interaction of cosmic rays with matter in which pions are produced. These decay to γ-rays and neutrinos. The energy spectrum of cosmic rays [3] shows a decreasing flux over a wide range of increasing energy and follows a broken power law (see figure 2.2). The general evenness of the spectrum features characteristics like the *knee* (above 10^{15} eV) and the *ankle*

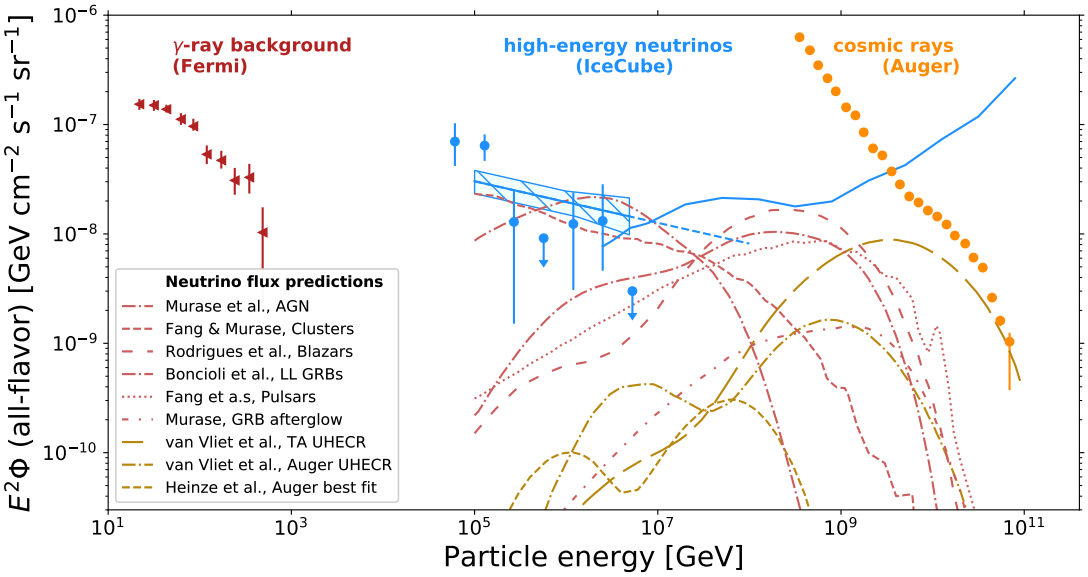

Figure 2.1: The science reach of the radio detection of neutrinos illustrated by a multi-messenger view of the high-energy universe. The figures shows the measurements of different detectors: the γ-ray measurements from Fermi [20], the neutrinos measurements from IceCube together with the fit to the muon neutrino spectrum [19] and ultra-high-energy cosmic ray measurements by the Pierre Auger Observatory [5]. Additionally models predicting neutrinos from sources (light red) are shown as well as models predicting neutrinos as products from the interaction of ultra-high-energy neutrinos with photon backgrounds (dark yellow). Figure from [21].

(above $5 \cdot 10^{18}$ eV) [22]. The quite sudden end of the known energy spectrum is just above 10^{20} eV. The particle composition of the cosmic ray flux changes with energy. The composition at ultra-high-energies is still under debate while it is at low energies familiar: cosmic rays consist mostly of protons (ionized hydrogen) follwed by helium nuclei [23]. At low energies (<100 MeV) the main part originates from the sun, at higher energies cosmic rays from other galactic sources dominate. The particle composition changes somewhere in the PeV- to EeV-range: the origin of the particles transists from mostly galactic to mostly extra-galactic [24]. The precise location of the transition remains unknown. Neutrinos might help to study the transition region. If a detected neutrino is a decay product it must have been produced by hadrons that had at least a 20 times higher energy [25]. This would mean a neutrino with an energy in the PeV-range would derive from a cosmic ray with an energy from the suspected transition region.

The end of the cosmic ray energy spectrum and the composition of these ultra-

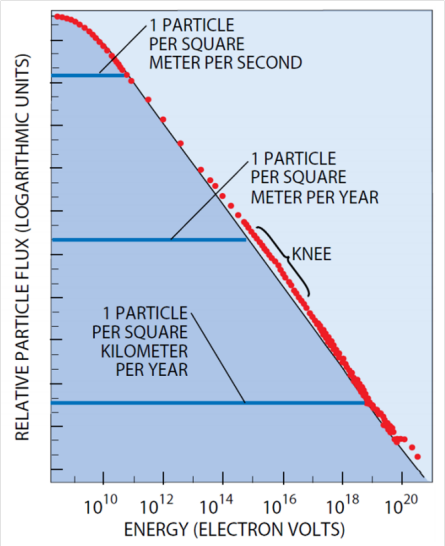

Figure 2.2: Cosmic ray energy spectrum. Overview of the entire measured energy spectrum of cosmic rays which is strikingly smooth and is steeply droping. Figure from [22].

high-energy cosmic rays is not fully understood yet. The end could on one hand determine the limits of the acceleration power of the particles origin. On the other hand: when cosmic rays with a very high energy travel through the universe the probability for an interaction with photons of the CMB increases. This could also explain the end of the energy spectrum.

2.1.2 Cosmic Neutrino Production

Ultra-high-energy neutrinos with energies up to the EeV-range either directly from the cosmic ray sources (*astrophysical neutrinos*) [26] or as interaction products of propagating cosmic rays with photon backgrounds (*cosmogenic neutrinos*) [27] are important messengers as they bare informations about the most distant, powerful energy sources throughout the universe.

Astrophysical neutrinos emerge at (or in the direct vicinity to) the sources of ultra-high-energy cosmic rays in interactions with photons and matter. So detecting these neutrinos may help to find cosmic ray sources. Astrophysical neutrinos contribute to a constant diffuse flow rather then necessarily coinciding with explosive events. There are several theories about which astronomical objects are the origins of astrophysical neutrinos, including pulsars [28], Active Galactic Nuclei (AGN) [29], various types of gamma-ray bursts (GRBs) [30, 31], Flat Spectrum Radio Quasars (FSRQs) [32], clusters [33] and blazars [34].

Neutrinos with energies in the PeV-range could be produced in pion photo production caused by protons with energies around 10^{17} eV.

While in the same energy range, cosmogenic neutrinos tend to be of higher energy than astrophysical neutrinos. Cosmogenic neutrinos have not yet been observed but their flux is expected to be higher then that of astrophysical neutrinos at energies above 100 PeV, being the main neutrino source at this energy regime [35]. They are supposed to reach record-high energy, up to at least 50 EeV [36]. While the neutrino with the highest detected energy so far had an energy below 10 PeV [37]. The resulting question is, if the flux is so small, that the existing detectors have been too small to measure those rare neutrinos or if neutrinos of such high energies do not exist.

Cosmogenic neutrinos are supposed to be created by extra-galactic cosmic rays in interactions with the CMB due to the GZK-effect [38, 39]. The GZK-cutoff also predicts the upper energy limit for protons from far away sources while heavier nuclei interact with the infrared background or the CMB via other effects.

The GZK-cutoff is a characteristic drop in the spectral distribution of cosmic rays, expected at the highest energies at about 10^{20} eV. Protons with very high energies interact with photons of the CMB and excite a delta resonance, the limit results from the necessary energy (50 EeV) for the delta resonance production, the resonance lasts extremely short (10^{-23} seconds) [36].

The resonance breaks down into a pion and a nucleon via:

$$\begin{aligned} \mathrm{p} + \gamma_{\mathrm{CMB}} \rightarrow \Delta^{+} &\rightarrow \mathrm{n} + \pi^{+} \\ &\rightarrow \mathrm{p} + \pi^{0}. \end{aligned} \tag{2.1}$$

The reactions between the proton and photons cause the ultra-high-energy proton to lose kinetic energy as long as the energy is above the threshold. Therefore protons with higher energies are missing in the distribution of cosmic rays since the probability for this interaction to take place for protons propagating through the universe increases with distance. Cosmic rays with a closer origin could travel unimpeded and cause some few observations above the limit. But if the GZK-cutoff is in fact the main reason for the steep drop in the spectrum above 10^{20} eV is not for sure.

Cosmogenic neutrinos are created in the GZK-process: while the neutral pion decays into γ-rays, the charged pion decays into high-energy neutrinos. The energy spectrum and the flux of cosmogenic neutrinos are based on the mass composition of ultra-high-energy cosmic rays, but they also depend on assumptions about the origins of cosmic rays concerning their chemical evolution and their cosmological luminosity. These parameters may differ outside of the local universe [40]. In addition, the composition of cosmic rays at high energies is only assumed to be mostly protons.

Questions hoped to be answered with the observation of cosmogenic neutrinos concern the upper extent of the energy spectrum as well as the composition of ultra-high-energy cosmic rays setting constraints on the models of either a lighter proton-rich or a heavier composition of cosmic rays. Composition predictions based on measurements by the Telescope Array (TA) [41] (proton-rich) and Auger [42] (heavier) seem to show opposite tendencies. Yet both models are still compatible within systematic uncertainties [43] (for other models see [44]).

The observation of any of these diffuse neutrino fluxes would further help to understand the production and acceleration mechanisms of high-energy neutrinos and their yet to be identified sources. The detection of high-energy cosmic neutrinos offers the unique opportunity to explore fundamental particles and interactions in otherwise unreachable energy and distance regimes (more can be found in [45]).

2.1.3 Radio Emission of Neutrino Interactions

An optical detector with the sensitivity to observe cosmic neutrinos above 10^{17} eV would have to be extremely large and very expensive considering the detector spacings which are determined by the scattering and absorption lengths of light in ice. So to build a detector with the necessary size to accomplish the wanted sensitivity at a reasonable price another detection method has to be used. A larger detector volume is possible using the radio technique, which is based on particle showers producing via the *Askaryan effect* radio emission, to detect neutrinos [46].

The Askaryan effect is named after Gurgen Askaryan, a Soviet-Armenian physicist who predicted in 1962 that a neutrino that interacts with a dense dielectric material induces an particle cascade which emits a detectable, coherent radio signal in the MHz to GHz frequency range.

The effect has been verified in accelerator experiments [47, 48, 49] and observed in air showers as secondary emission mechanism [50]. Neutrinos of all flavors induce electromagnetic or hadronic particle showers in dense, radio transparent media [14].

In the interaction of a EeV-neutrino and a nucleon, a lepton and a jet are produced or a neutrino and a jet. Neutrinos can interact with the nucleon either by exchanging a charged or a neutral Boson. The jet of secondary particles is caused by the fragmentation of the nucleon. In a charged-current interaction the neutrino energy gets distributed to the developing cascade. In neutral-current interactions only a part of the neutrinos energy transits to the cascade - how much depends on the collisions inelasticity. In addition secondary particles like muons or taus may induce showers as well [52]. The neutrino and neutrino induced shower interactions are summarized in: [51].

The shower develops a charge anisotropy as electrons of the surrounding medium get either collected by the shower as they get Compton scattered or they annihilate with shower positrons. The shower front becomes increasingly negative as can be

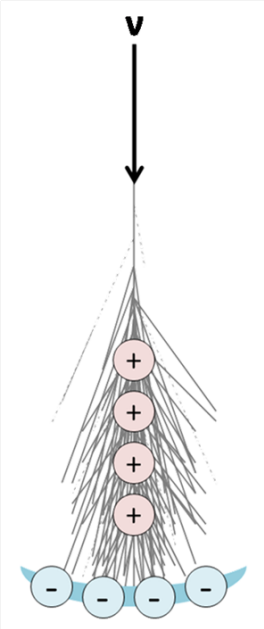

Figure 2.3: Askaryan effect. A time varying net-charge is caused by a longitudinal unbalanced charge distribution in the neutrino induced shower in a dielectric medium (such as salt [48] ice [49] or the lunar regolith [53]), which generates a radio signal.

seen in figure 2.3 and emits radio radiation when the charge excess is propagating faster then the phase velocity of light in that medium. Since the shower front is smaller than the wavelength of the radiation at MHz frequencies, the emissions in this range are coherent. The radio pulse that the time variation of the shower's net charge causes is broadband bipolar and only a few nanoseconds short. The signal is strongest when all frequencies arrive in phase which is close to the Cherenkov angle. There, the signal is coherent over all frequencies (about tens of MHz to tens of GHz). At lower frequencies the Cherenkov ring is broader while at high frequencies it is quite narrow since coherence gets lost off the Cherenkov angle at higher frequencies.

The amplitude scales (as a coherent effect) linearly with the number of excess electrons, which in turn is linear in shower energy [54].

2.1.4 Radio Detection of Neutrinos in Ice

The radio pulse is most prominent in the MHz frequency range. To measure these signals an array of radio antennas form a detector. The times when the individual antennas were triggered are used to determine the direction where the neutrinos

are from.

The advantage of the radio detection method is the possibility of a large effective detector volume at a reasonable price point. Ice is a suitable medium for a radio neutrino telescope since it exists in the needed large volumes in nature, is very uniform and radio clear. Only a small number of detector stations is needed which is determined by the attenuation length in ice. The attenuation length to a measurable neutrino interaction is about 1 km [55, 56, 57] and scales inversely with temperature. It also has to be considered that ice in nature follows a density gradient with depth. The radio signals bent towards the denser medium and signal disturbances may occur as it is a natural material, therefore reconstruction is not simple. All considered a thick, cold, smooth and homogeneous ice with a small top layer firn is favored.

The Earth is opaque to neutrinos with energies above 1 PeV therefore a radio detector does not offer full sky coverage, but only sensitivity to a ring of elevations above the local horizon. With increasing deployment depth the number of vertically incoming neutrino directions grows.

To resolve the radio pulses fast and broadband measuring systems are needed. At the time this method was first proposed neither was possible. In addition, it was not possible to filter the growing human-made interferences. Since then the technological possibilities that have developed over the past few decades and new experiments to understand the radio emission have revived the research field of the neutrino detection via radio emission.

2.2 The Radio Neutrino Observatory in Greenland

Assuming that the astrophysical neutrino flux follows an E^{-2} spectrum and the EeV part of the cosmogenic flux of neutrinos is of order $10^{-9}\,\mathrm{GeV\,cm^2\,sr^{-1}\,s^{-1}}$ an effective volume of the scale of hundreds of cubic kilometers is required to make observations in the PeV to EeV energy range. The long attenuation length of radio signals in ice, about 1 km, makes it possible to achieve such a detector volume by a reasonable number of radio stations in glacial ice.

2.2.1 Science Case

The goal of the *Radio Neutrino Observatory in Greenland* (RNO-G) [21] is to detect neutrinos with energies of several PeV up to the EeV range via the Askaryan effect. This large-scale implementation of the in-ice radio neutrino detection technique therefore targets neutrino energies beyond the reach of IceCube. Due to the kilometer scale attenuation length of radio waves in ice, very sparse radio detectors cover large volumes of material, providing huge effective volumes. RNO-Gs

observation of the diffuse flux of ultra-high-energy neutrinos will be unprecedented and a milestone in multi-messenger astrophysics. With exceptional sensitivity to neutrino signals above 10 PeV, RNO-G aims to detect astrophysical neutrinos with energies that exceed all previous measurements. RNO-G will use its vast field of view and broad energy regime to search for transients as well as for point sources of ultra-high-energy neutrinos. Very important in multi-messenger astrophysics are neutrino measurements coinciding in space or time with explosive events. Models predicting neutrinos in the PeV to EeV range exist that assume binary neutron star mergers [58, 59] and tidally disrupted stars [60, 61] causing transient neutrino bursts. Also under multi-wavelength investigation are several blazar populations [32, 34]. Since RNO-G will have a lower energy threshold, probing previously measured γ-ray bursts (GRBs) with lower neutrino luminosity is also a possibility [30, 31].

RNO-G is built to achieve, through high efficiency and a low threshold, the worldwide best ultra-high-energy neutrino sensitivity and to test the scalability of a radio detector array and deployment strategies. RNO-G will on one hand observe as the first ultra-high-energy neutrino detector the Northern hemisphere and on the other hand will serve as a technology pathfinder for the next-generation neutrino detector IceCube-Gen2. The experiences made with RNO-G will help to design and deploy the radio component of IceCube-Gen2 [62].

RNO-G has been designed with the gained competences and experiences of successful radio neutrino detecting projects like the pioneering Radio Ice Cherenkov Experiment (RICE) [63, 64], the Antarctic Ross Ice-Shelf Antenna Neutrino Array (ARIANNA) [65, 66], the Antarctic Impulsive Transient Antenna (ANITA) [67, 68] and the Askaryan Radio Array (ARA) [55, 69, 70]. The idea of RNO-G was to combine the best technologies from previous radio neutrino detectors. While these previous detectors (RICE, ARA, ARIANNA, ANITA) are all located in the Southern hemisphere, RNO-G will observe as first ultra-high-energy neutrino detector the Northern sky.

2.2.2 Experimental Design and Construction

RNO-G will be constructed in Greenland in three deployment seasons starting 2021. The RNO-G detector will eventually consists of 35 stations, each with borehole antennas coupled with surface antennas. The detector is located at Summit Station at the peak of the Greenland ice cap. Below a 100 m firn layer are more than 3 km of strikingly radio transparent glacial ice [57]. The density profile of the ice is not homogeneous therefore the radio signal gets refracted in the ice. In addition the signal gets reflected at the ice-air boundary.

The detector stations will be deployed in an approximately 1 km spaced grid. The stations all work autonomously and have two components: a surface one and

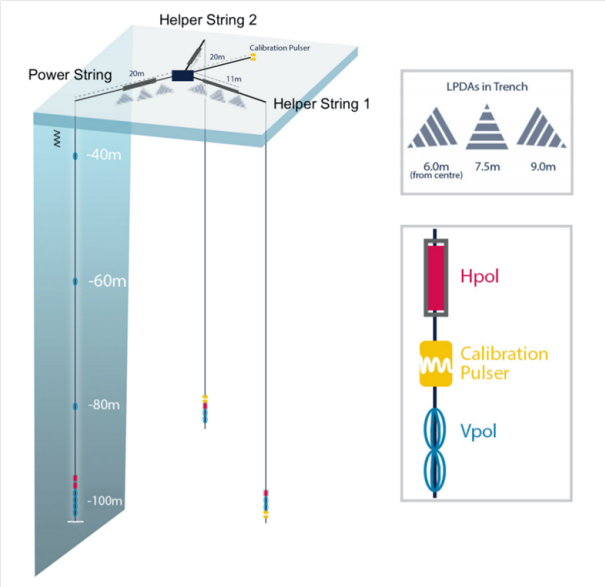

Figure 2.4: RNO-G station design. Every RNO-G detector station is composed of three antenna strings (with Hpol and Vpol antennas) in the boreholes: two *support strings* and one *power string* containing the phased array trigger as well as surface antennas (LPDAs) and three calibration pulsers on the surface and deep in the ice. Figure taken from [21].

.

a down-hole one. The station design is schematically displayed in figure 2.4.

The combination of a low threshold deep trigger and the surface antennas accomplish a cosmic ray veto, a high trigger efficiency and make a precise reconstruction of events possible. The three major background sources are: man-made noise, incoherent thermal noise and radio signals from cosmic ray induced air showers. To accomplish with high efficiency the distinction of neutrino signals and backgrounds, RNO-G uses the surface component for background veto (non-thermal backgrounds by man-made sources or air shower remnants) and triggers from deep below the surface, where the backgrounds are smaller compared to above [73].

At each station 100 m down into the ice the deep component is positioned which provides for a large effective detector volume of about 1 km^3 per station.

For polarization measurements vertically (Vpol) and horizontally (Hpol) polarized antennas are being used as deep component antennas. The design of the borehole antennas is restricted by the borehole size. The Hpol antenna design is optimized for azimuthal symmetry, simple modeling and simple construction. It is a tri-slot, ferrite-less cylindrical antenna. The Vpols are fat dipoles and since they have a broader bandwidth than the Vpol antennas they are used for the trigger.

There is enough overlap between the Vpol and Hpol band for signal polarization measurements.

In the boreholes are three strings installed, one main string and two support strings. The support strings are required for azimuth reconstruction. At the down-hole end of the main string four Vpol antennas for interferometric triggering are installed while the other antennas and strings are intended for calibration and reconstruction.

The strings are supplied, as well as the surface antennas, by a central data aquisition system (DAQ). The DAQ will be positioned in a weatherproof housing on the surface. The antennas and strings are positioned and spaced in a way that allows a good reconstruction of the arrival direction and energy of the particle for the separate stations.

Because of the high gain that is possible without the borehole restrictions, the nine log-periodic dipole antennas (LPDAs) of the surface component, arranged with different orientations, will measure all polarization components exact and provide a clear separation between signals coming from above or from below. Since the LPDAs are the largest out of the antennas used, they have the largest gain and offer the vastest frequency coverage for the measured signals.

Air shower signals follow the same radio emission mechanism as neutrino induced showers in the ice (even the dominating effect is the geomagnetic effect over the Askaryan effect [71, 72]) and appear therefore quite similar. Due to their similarity and since they are more frequent, they can be used as a calibration signal. At the same time the similarity entails the risk of wrongly identifying a refracted air shower signal as neutrino signal. Hence, the surface antennas serve as air shower array for calibration and are important for the event characterization and reconstruction as they help to reduce background by functioning as a cosmic ray veto.

The signals from the borehole antennas are transmitted via a radio frequency (RF) chain and the surface as well as the down-hole signal chain use custom developed amplifier boards (see section 2.2.3).

Since neutrinos rarely interact most just pass through the Earth unattenuated but at the PeV energy range and above, the Earth becomes opaque to neutrinos, hence detectors operating in this energy range are most sensitive to neutrinos coming from above. Therefore the area RNO-G will observe overlaps with the peak of IceCube's field-of-view and RNO-G's measurements will be a continuation at higher energies of IceCube's measurements.

RNO-G will help to define the neutrino energy flux at ultra-high-energies, therefore even one detected neutrino or no detection at all will be of scientific importance by narrowing down the allowed flux. The measurements of RNO-G will help to set limits on several astrophysical neutrino models like presuming their origin to be pulsars [28] or jets of active galactic nuclei [29]. RNO-G will help further to set

constraints on the models of either a lighter proton-rich TA [41] or a heavier Auger [42] composition of cosmic rays and will restrict the upper energy cutoff of cosmic rays. These parameters will also be limited in the case if RNO-G does not detect any neutrinos.

2.2.3 Radio-Frequency Front-End Design

There are two different signal chains in RNO-G: one for the signals measured with the surface antennas and one for the signals measured with the borehole antennas.

The signals from the surface LPDAs are transmitted via short coaxial cables of less than 20 m to the Data Acquisition box (DAQ box). The signals are amplified only once after they have been fed into the DAQ box by the two SURFACE amplifier boards (see figure 2.5 (left) and figure 2.6) per station.

Each detector station contains 15 down-hole antennas distributed over three boreholes. The signals coming from the antennas in the in-ice boreholes travel through a short coaxial cable to a down-hole front-end where the low-noise amplifier (LNA) of the IGLU board (one IGLU per antenna, see figure 2.5 (center) and figure 2.7) increases the signal strength to minimize the system noise temperature.

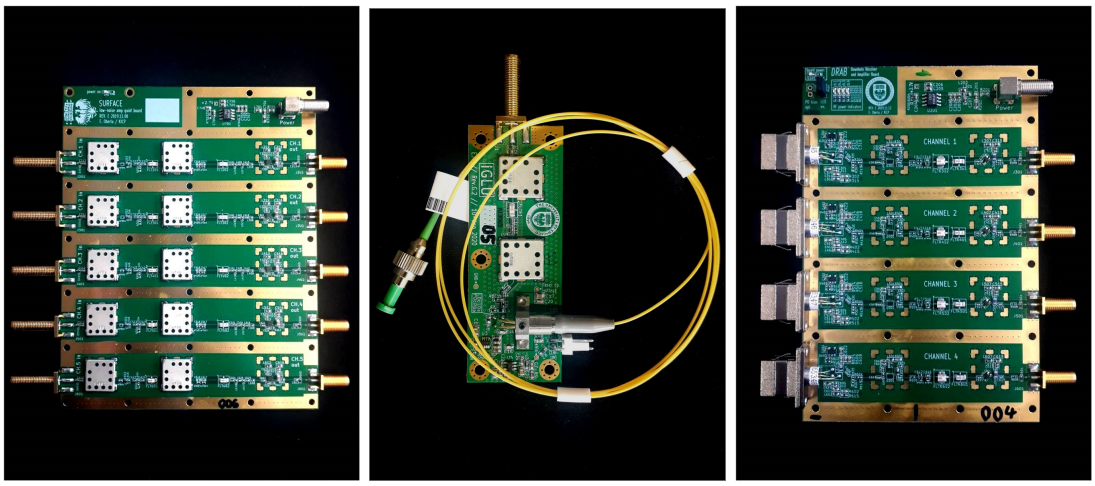

Figure 2.5: Custom designed amplifier boards for RNO-G. Left: a SURFACE board (5-channel full-chain amplification and filtering board) for the signals coming from the surface antennas. Center: an IGLU board (In-ice Gain with Low-power Unit) that converts the signals from the borehole antennas to analog RF signals and feeds them into a fiber. Right: a DRAB (4-channel Down-hole Receiver and Amplifier Board) that amplifies the signals coming from the IGLUs and converts them back to analog signals. All amplifier boards are shown without their environmental enclosures.

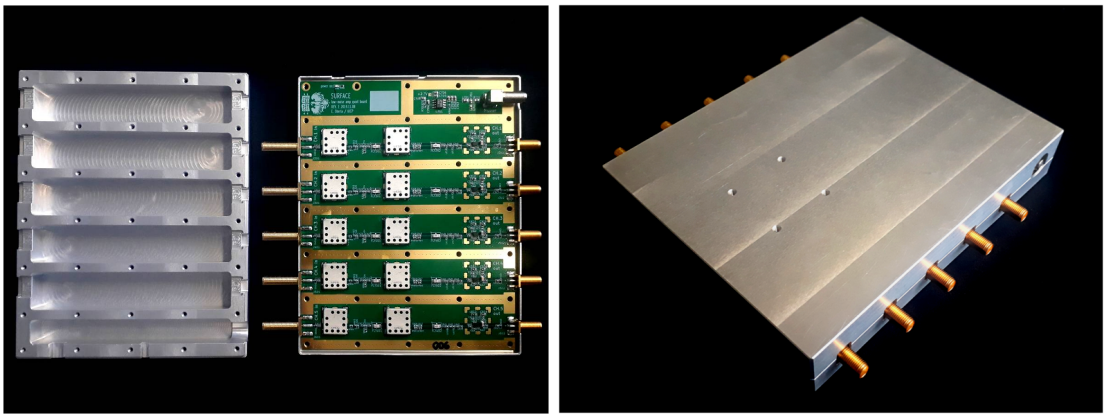

Figure 2.6: SURFACE board in enclosure. Left: a SURFACE board in its open enclosure before an absorber foil was put in. The absorber was placed in the enclosures of all IGLUs, DRABs and SURFACE boards before they were sealed. Right: closed SURFACE board housing.

The signals are converted at the front-end to analog RF signals and feed via a Radio Frequency over Fiber (RFoF) transmitter into a fiber. The radio signal modulates the light which transfers the signal with very low attenuation over an optical fiber connection.

The low transmission losses compared to other transmission methods such as metal cable or wireless transmission and further the reduced electromagnetic interference and less noise sensitivity are the main advantages of radio over fiber technology.

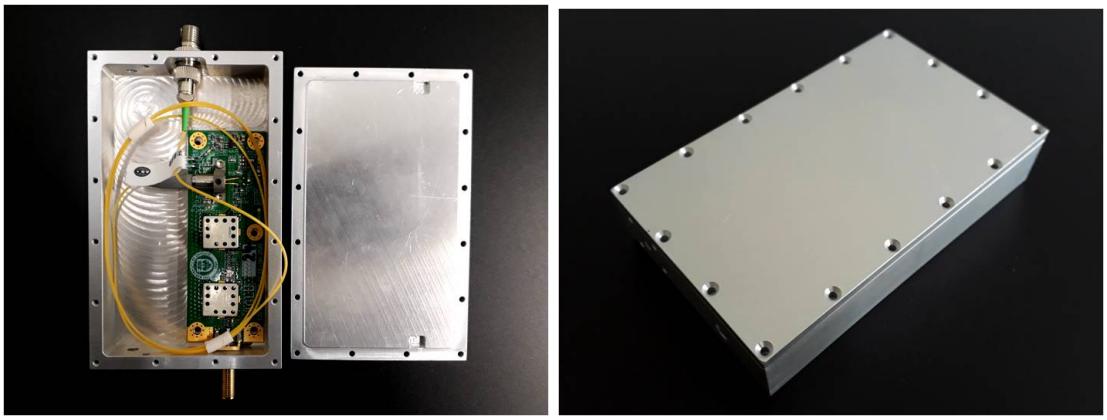

Figure 2.7: IGLU board in its enclosure: the IGLU board is the only board that will be placed in the borehole. Left: IGLU board in housing before sealing. Right: IGLU board in closed housing, the enclosure will protect the board from the environment when it is installed in the borehole.

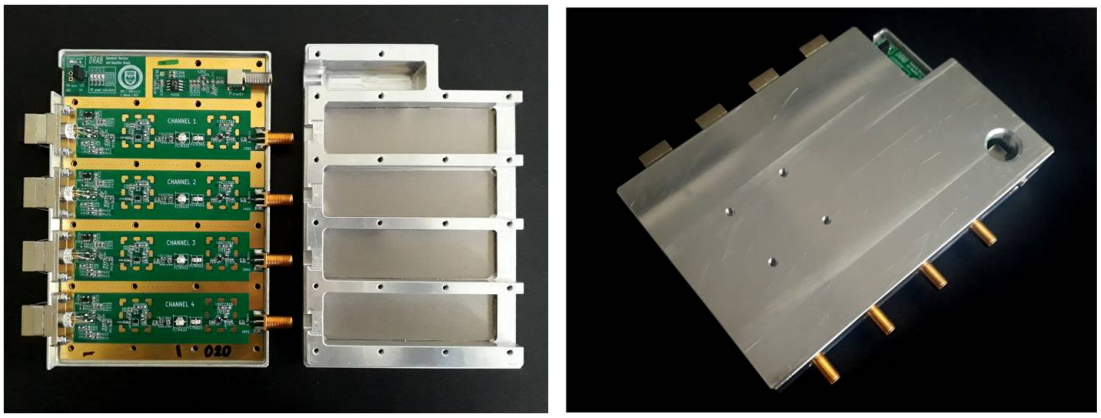

Figure 2.8: DRAB in enclosure. Left: DRAB in enclosure before closing. The gray absorber foil is put in to reduce crosstalk between channels as well as the enclosures themselves are supposed to reduce crosstalk. Right: closed DRAB housing.

RFoF technology is therefore used to bridge larger distances without additional amplifiers and repeaters. The only through-going coaxial cable in the array is used to power the RFoF link and LNA from the surface via a DC connection. To have an optimized noise temperature of $\leq$150 K as well as low power the LNA and RFoF are custom designed.

After transmission through a tactical fiber bundle, the signals are received by the DRAB-amplifiers (see figure 2.5 (right) and figure 2.8) where the signal strength gets increased and the signals are converted back to analog ones. The four DRABs per station are located in the DAQ-box like the SURFACE-boards.

All amplifier boards are put in custom-designed RF-tight enclosures made of iridited aluminium (chromate conversion coating). The housings shelter the IGLU boards in the boreholes from the environment and reduce the influence of noise considerably.

This thesis describes the measurements of different properties of these amplifier boards in order to characterize the different board types and to develop a standard test and calibration procedure. The next chapters will describe the properties that were measured, the procedure in which the boards were tested and furthermore the measured data will be interpreted.

The boards were tested with a vector network analyzer to evaluate the differences between the individual boards and to test their performance. To test the resistance of the boards to extremely low temperatures and to analyze their temperature dependence they were tested in a temperature chamber. All tests were done to characterize the different board types (DRAB, IGLU and SURFACE board) and the individual boards.

3 Theory of Electronic and Amplifier Properties

The three different types of amplifier boards (see section 2.2.3) which will be used in RNO-G were tested with a vector network analyzer. Different measurements were done to analyze the properties of the amplifiers. In this chapter these properties and their interpretation will be explained. Different measures at different frequencies (between zero and one GHz) helped to find defect boards or defect channels. The reflection and transmission features were characterized as well as the signal increase that the amplifiers provide were studied. Additionally the origins of signal deformation were examined.

A *network analyzer* is an equipment that offers significant insights into the characteristics and the performance of a *device under test* (DUT). The network analyzer enters a stimulus into the device and then reviews its response to examine the performance of the device. Dependent on the impedance match, a part of the power is reflected back to its source, when power enters the DUT. To examine the characteristics of a device the transmitted and the reflected signal at the input and the output are measured across the bandwidth of interest and often beyond. For a complete characterization of a device measurements of magnitude as well as of phase are necessary. A *vector network analyzer* (VNA) therefore measures both: additional to the amplitude it determines the phase, since phase is a crucial element in network analysis. Low level signal measurements such as crosstalk (see section 3.4) can be done with high accuracy with a VNA. Network analyzers usually operate at high frequencies (radio and microwave). The performance of devices with multiple ports can be tested with network analyzers but they are typically used for two-port devices. More details about (vector) network analyzers can be found in [74, 75].

If a measurement is repeated the results will be slightly different, which will affect the accuracy of the measurements. How close a measurement is to the true value and how close the results of a number of measurements of the same setup correspond to each other depends on the systematic and random error of a measurement.

Defects in the experiment setup or in the network analyzer are the reason for systematic errors. Systematic errors are always the same within the same test

setup and therefore predictable. Since they are repeatable they can automatically be characterized during calibration in order to be subtracted from the subsequent measured data. For further details on systematic errors and their elimination, see: [74].

Hence, before the measurements with the DUT are started a calibration is done to remove systematic errors. In the case of this thesis the calibration was done with a mechanical calibration kit.

Random errors, opposed to systematic errors, differ between different measurements with the same setup. They become visible as variations in the results of a repeated measurement. Unpredictable and unidentified differences in the measuring equipment or in the environment of the experiment cause random errors. The major origins of random errors are instrument noise errors, switch repeatability errors and connector repeatability errors. Since random errors vary with time unpredictably, calibration can not be used to eliminate these errors hence random errors can not be easily removed from the measurement. The comparison of repeated measurements helps to determine random errors and averaging over several measurements helps to assess the actual value. More information on the causes of random errors can be found in [76, 77].

3.1 S-Parameters

Scattering-parameters, usually abbreviated to *S-parameters*, provide information about the transmission and reflection attributes of a DUT in form of a complex matrix. S-parameters are used to design and analyze devices and circuits. When a device is exposed to stimuli by a VNA, the S-parameters are used to characterize its behavior like its gain (see section 3.2) or return loss. The S-parameters are used to quantify how signals are scattered or reflected when a device is put in the signal's transmission line. The word *scattering* therefore indicates the influence of the insertion of the DUT as a discontinuity in the transmission line. Each S-parameter is represented by a complex number that is depicting amplitude and phase. While the angle is usually expressed in degrees, the amplitude may be expressed in linear form or logarithmic form. The logarithmic form is measured in decibels (dB) and it is very often used. But to study certain features in the data it sometimes makes more sense to use the linear form, in magnitude.

The S-parameter S_{ij} in logarithmic form is:

$$S_{ij}\ [\text{dB}] = 20 \cdot \log_{10}(S_{ij}\ [\text{mag}]). \tag{3.1}$$

The number of matrix-elements and thus S-parameters depends on the number of ports. A device with N ports has N^2 S-parameters stored in a square matrix of dimension N. A device with two ports accordingly has four S-parameters:

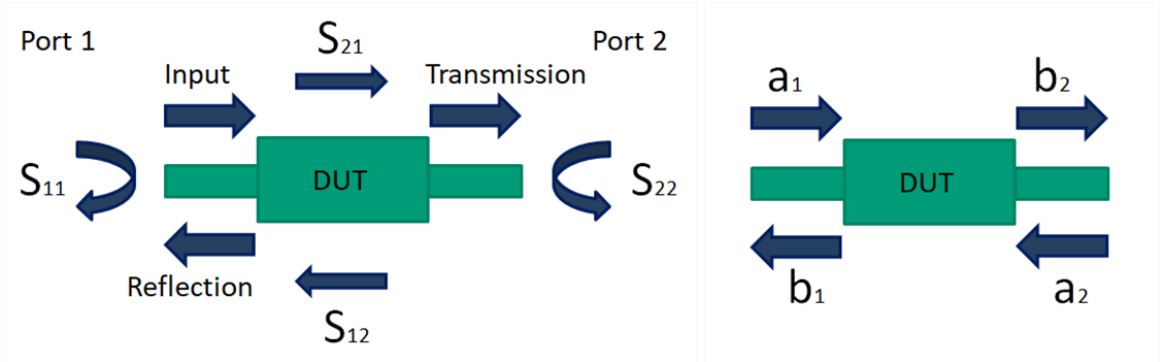

Figure 3.1: Signal flow graphs showing the concept of S-parameters for a 2-port device, with port 1 being the source port and port 2 being the terminating port. Left: The input, the reflected and the transmitted signal and the concept of the four S-parameters. Right: The relation between input, output and the S-parameter matrix. (Figures adapted from [80].)

S_{11}, S_{12}, S_{21} and S_{22}. The first number displays the port at which the signal leaves the device (output port). The signal is inserted at the port with the second number (input port). Hence, S-parameters with different numbers are transmission measurements, S-parameters with two identical numbers belong to reflection measurements. Therefore S_{12} and S_{21} are the transmission coefficients and they are calculated by dividing the transmitted by the input signal while S_{11} and S_{22} are the reflection coefficients and they are the ratio of the reflected and the input signal. The measurement of amplitude and phase of the incident, reflected and the transmitted signal at port 1 determines S_{11} and S_{21} while S_{22} and S_{12} are determined analogously with the source port being port 2 (see figure 3.1 (left)). The S-parameters depend on the frequency at which they are measured and the changes in amplitude and phase that the device causes in the signal are not the same for all frequencies. Hence, the waveform in the time domain can be very distorted when a time-varying signal passes through the device. Information on amplitude or phase characteristics are of importance in the frequency domain. To determine the phase distortion the group delay (see section 3.3) of a device is measured. S_{11} and S_{22} are the input and output reflection coefficients while S_{12} and S_{21} are the reverse and forward transmission coefficients.

The relation between the incoming and outgoing signals and the S-parameter matrix for a 2-port device can be seen in figure 3.1 (right) and is given by:

$$\begin{pmatrix} b_1 \\ b_2 \end{pmatrix} = \begin{pmatrix} S_{11} & S_{12} \\ S_{21} & S_{22} \end{pmatrix} \begin{pmatrix} a_1 \\ a_2 \end{pmatrix}. \tag{3.2}$$

S_{11} is the reflected voltage at port 1 divided by the voltage input at port 1, while

there is no input at port 2 ($S_{11} = b_1/a_1$). S_{12} is the output of port 1 divided by the input at port 2, while there is no input at port 1 ($S_{12} = b_1/a_2$). S_{22} and S_{21} work analogous with switched numbers ($S_{21} = b_2/a_1$ and $S_{22} = b_2/a_2$). If S_{11} or S_{22} is equal to zero this means there is no reflection at all, while if S_{11} or S_{22} is equal to one would mean the signal is completely reflected. If S_{12} or S_{21} is equal to zero this means no signal is transmitted through the DUT. A transmission coefficient between zero and one means the signal is damped by the device: the absolute value of the transmitted voltage is smaller than the absolute value of the input voltage (attenuation or insertion loss). While a coefficient greater than one, meaning the absolute value of the transmitted voltage is larger than the absolute value of the input voltage, indicates an amplification of the signal. This section about S-parameters has been written using information from: [78, 79, 80, 81], a summary of how and why S-parameters are measured can be found in [74].

3.2 Gain

The purpose of an amplifier is to increase the strength of the signal that is applied to it. The amount of amplification provided by an electronic device like an amplifier is quantified by its *gain*. Gain is the ratio of the transmitted voltage V_{out} to the incident voltage V_{in}: the S-parameter S_{21}. *Amplification* describes a S_{21} measurement greater than one (linear) or greater than zero decibel (logarithmic). The gain varies with the frequency of the applied signal. The flatness or the variation of the gain over a specified frequency range determines the distortion of the signals passing through the DUT. When the frequency components are not amplified uniformly deviations in the intended operating frequency range, the passband of the device, lead to a distortion in the transmitted signal. Therefore an even and flat gain in the passband is preferred, the variation in the passband of the amplitude is called *passband ripple*. The gain is often given in decibels, which expresses the ratio on a logarithmic scale:

$$\text{gain [dB]} = 20 \log_{10} \frac{V_{out}}{V_{in}}. \tag{3.3}$$

The gain of an amplifier depends on the temperature it is measured at and varies over a range of different temperatures (see section 3.6). This section has been written using information from [81, 82, 83, 84].

3.3 Group Delay

Group delay describes the time a signal needs to propagate through a device versus frequency, it quantifies the phase distortion of said device. To compute the group

delay the slope of the transmission phase ϕ is needed. Group delay is the negative derivative of the device's phase response with respect to frequency f:

$$\text{group delay [s]} = -\frac{d\phi}{df}. \tag{3.4}$$

In the case of an ideal device signals passing through would maintain their shape. But in reality all frequency components of a signal are delayed when it transits through a device such as an amplifier. The signal delay in transmission is usually different for different frequencies: Signals that consist of various frequency components change their shape if the different components have different delay times. The ripples in the group delay measurement indicate how much the frequency components of a signal become misaligned due to the DUT. The phase misaligning of a signal's different frequency components causes variations in the group delay which translates into signal distortion. The distortion is the same for all signals propagating through the device. Hence, the concern when doing a group delay measurement is not so much about the delay time itself, but if all frequency components of a signal require the same amount of time to pass through the DUT so that their phase relative to one another and therefore the signal's shape is maintained. A constant group delay at all frequencies would mean the signal shape would not be deformed. This section has been written using information from [80, 85, 86].

3.4 Crosstalk

Crosstalk describes the signal leakage between one circuit or channel of a transmission system during signal propagation into any other circuit or channel. It is any undesired effect caused by accidental (capacitive, inductive, or conductive) coupling between circuits or channels and it depends on the signal's frequency. An ideal device with several channels would have no output signal at the channels without an input signal. In reality, however, the signals interfere in channels close to each other. A crosstalk measurement determines the disturbance due to other channels. To measure crosstalk, one applies a signal at one channel and measures the output signals at the other channels without any input. Crosstalk, as a measure of the amount of unwanted coupling, is the ratio between the quiet channel and the channel with a signal and is usually given in decibels. This section has been written using information from [87, 88, 89].

3.5 Noise Figure

All electronic devices generate noise. The decline of the *signal to noise ratio (SNR)* due to a device can be defined by the *noise factor (F)* or the *noise figure (NF)*.

The noise figure and factor describe the *SNR* at the input compared to the *SNR* at the output. Both describe basically the amount of noise a device adds to signals propagating through that device or that a component adds to a whole system. It is the difference between the output noise of the actual device to the noise output of an ideal device. In an ideal system the *SNR* of output and input would be the same since no noise would be added to the signal when being transmitted through a device. In reality every component in an electronic circuit adds noise. The noise factor is the ratio of the input *SNR* (SNR_{in}) to the output *SNR* (SNR_{out}):

$$F = \frac{SNR_{\text{in}}}{SNR_{\text{out}}}. \tag{3.5}$$

The *SNR* at the input is always better than the *SNR* at the output, hence the noise factor is constantly greater than one. The noise factor represented in decibels is the noise figure:

$$NF\ [\text{dB}] = 10 \cdot \log_{10}(F). \tag{3.6}$$

Noise figure is used to quantify the performance of devices like amplifiers, with smaller values indicating better performance. More details about the noise figure can be found in [90].

3.6 Temperature Dependence of Amplifiers

The amplifier gain depends on the temperature at which it is measured and changes over a range of various temperatures. Therefore the cooling of the amplifiers deployed in or on the Greenland ice will affect the amplifier gain. Typically, the gain of an amplifier decreases over increasing temperature and the noise figure increases. On the other hand, the gain of an amplifier increases with decreasing temperatures. For the amplifiers of ARIANNA [91] on the Ross Ice Shelf, for example, there is an uncertainty of up to +15 % of the amplitude scale for the local ice temperature. But how much the gain changes depends on the used amplifier. Therefore the gain has to be measured at different temperatures in the lab in order to obtain precise gain curves. The dependence of the gain on temperature can also vary somewhat between individual amplifiers. Adjustments can be carried out by developing a model for the changes in the gain of the tested amplifiers due to temperature variations. This section has been written using information from [91, 92, 93].

This chapter gave a brief overview of how amplifier properties can be measured and interpreted. In the following chapter the measurements of said properties

will be discussed. The different tests to characterize the amplifier boards will be described and the measured data will be analyzed.

The testing process is supposed to verify the functionality of the boards as well as review their performance. In addition, several parameters were varied. For example the differences between the individual boards was tested and the influence of the used fiber connecting the DRAB and the IGLU board was studied.

The results of the data of these tests were compared to the expectations, the variation range within one board type was determined, different possible origins of signal distortion were checked and the influence of various parameters was analyzed.

4 Measurements

The tests that will be discussed in this chapter were done with 12 SURFACE boards, 47 IGLU boards and 23 DRABs. The DRABs and the IGLU boards are connected via a fiber cable and they can only be tested together. The tests were carried out in Erlangen after some inital tests with a few of the boards had previously been done in Chicago where the boards have been designed and manufactured.

During the measurements with the vector network analyzer, the SURFACE boards and DRABs were in their enclosures. While the IGLU boards were not in their enclosures for any tests that are described in this thesis (see section 6.1). A calibration was performed before testing with the VNA started. To examine the impact of the enclosures as a shield against signal interference, some crosstalk measurements (see section 4.3.4) were done without the enclosures too.

The four-phase test procedure started with a functionality test to check for broken boards and boards with insufficient temperature resistance for deployment in Greenland. Therefore a first function test was done followed by a temperature stress test. Afterwards another function test was then carried out.

After this basic survival test the performance of the boards was tested. In this next test phase boards which worked not correctly or whose measured values differ very much from the average were meant to be found. Additionally the characteristics and features of the different board types were identified. Measured were the group delay, the S-parameters with a focus on the gain of the amplifiers and the gain variation between boards. Some boards were tested for crosstalk as well as the noise figure of a few boards was measured.

The third testing phase focused on learning about the influence of different parameters and components like the used fiber in the IGLU and DRAB measurements and how large the random error is. For the down-hole signal chain the influence of the used IGLU on the results of the measurements were tested.

The last tests studied the influence of the temperature at which the data was measured in temperature dependence tests in a temperature chamber. The SURFACE board temperature tests concentrated on finding an easy way to take temperature related changes in the amplifier measurements into account instead of measuring every single board at multiple temperatures. The tests with the DRABs and IGLU boards on the other side focused on studying the influence of the temperature of different components on the measurements.

4.1 Data File Naming

The data of the tested hardware that will be installed in the RNO-G detector will be stored in a database that is currently under construction. All function, calibration and performance tests that were done with the boards for this thesis as well as future revisited board measurements will be stored in this database to be available for various members of the collaboration. For some tests (function test, stress test) the database entry only notes if the board passed the test (yes/no). While the S-parameter files of all boards will be uploaded. Some tests (crosstalk, noise figure, temperature dependence) were only done with a few boards and are an optional entry. The database also records for each board whether all mandatory tests have been passed.

Uniform naming and labeling of the individual components is essential for a large and growing database. The naming system includes the general type of hardware as well as an individual number.

The structure of the item specific label is: three letters for the **general type** of the component, the **specific type**, a combination of the **version** (letter, beginning with A) and an **identification number** (four digits, beginning with 0001). The version and ID number are combined, the object number therefore becomes:

$$\text{(general type)\_(specific type)\_(version and ID number).} \tag{4.1}$$

The general type is a three letter abbreviation of the tested hardware type (*Amp, Ant, Cab, DAQ, RFo, Cal, Fil*). The specific type specifies the component: for the amplifiers (*Amp*) for example: *Surf, DRAB* or *IGLU* for the exact type of amplifier board (SURFACE board, DRAB or IGLU board). The version and ID number starts with a letter (beginning with A), referencing the revision of the hardware component. The last four digits reference the individual item (beginning with 0001). For example the 23 tested DRABs in this thesis have the version and ID numbers: A0001 to A0023.

This form of component labelling for all items enables a simple handling in the database and automated testing as well as easy readability.

The boards tested in this thesis are therefore labeled as the following: The SURFACE boards have the object numbers Amp_Surf_A0001 to Amp_Surf_A0012, the DRABS have the object numbers Amp_DRAB_A0001 to Amp_DRAB_A0023 and the IGLU boards are labeled Amp_IGLU_A0001 to Amp_IGLU_A0047. These object numbers are printed on cryogenic labels together with a QR-Code containing the number and the ECAP-logo. The labels are sticked on the enclosures of the boards (see section 4.2).

The naming of the data files is based on the object number. The files are currently sorted into different folders (S-parameter, group delay, crosstalk...) and further

divided into Surface and DRAB measurements. Therefore the file names reference the version and ID number and the measured channel. The SURFACE board files are therefore named: A0001_chan1.csv while the DRAB files also consider the used IGLU: IGLU01_A0001_chan1.csv. Some tests need further information in the file names: Since for the crosstalk measurements (see section 4.3.4) input and output channel are not the same, the file name has to note both and becomes: A0001_chan1_chan2.csv. The first channel thereby references the channel with the signal input, the second channel is the channel where the output is measured.

The temperature dependence measurements (see section 4.5) also include a reference for the temperature at which the data was taken: A0001_chan1_T0.csv. All references for the different temperatures can be found in table 4.1.

room temperature	_roomT
0 °C	_T0
-10 °C	_T10
-20 °C	_T20
-30 °C	_T30
-40 °C	_T40
-50 °C	_T50

Tables 4.1: The references for the measured temperatures in the file name.

4.2 Function Test and Stress Test

Testing started with the function test of the boards. The first function tests before and after the stress tests to check the functionality of the boards were performed with an oscilloscope and a sine wave generator (see section 6.1).

Measured was the nominal current draw of the IGLUs. The function tests of the SURFACE boards and the DRABs were done with an oscilloscope (peak-to-peak, root mean square). Additionally the signal of a sinus generator was applied. So boards with unusual high or low signals, compared to the other boards, would stick out.

All *SURFACE boards* worked, but one board (board A0007) had two slightly offbeat channels: channel 4 had the highest and channel 5 the lowest signal of all boards, meaning this board showed the lowest uniformity of all 12 SURFACE boards. Channel 5 in particular stood out as its signal was by far the lowest. The channel with the maximum deviation of the SURFACE boards was therefore channel 5 with -11 %, while channel 4 deviated +7 % from the average of all boards.

All *DRABs* worked except for channel 2 of board A0008 which did not work due to a broken connection on the board, this was fixed after the function tests.

The nominal current draw for the SURFACE boards is 188±5 mA, for the IGLUs: 43±2 mA. First tests in Chicago showed a potential amplifier issue with some SURFACE and IGLU boards. Both of these issues appeared to be related: the first-stage amplifier seemed to be non-powered. The problem was obvious in the current draw of the boards. All SURFACE boards in Erlangen were already checked for that issue while the IGLUs had to be examined for that too. The broken IGLUs showed a current draw of about 32 to 33 mA.

Out of the 47 tested *IGLU boards*, four boards showed an unexpectedly low current draw of around 32 to 33 mA (IGLUs: A0033, A0009, A0012, A0037) and were therefore no further tested. While two boards with the expected current draw showed no signal (IGLUs: A0045, A0002), these two boards were fixed later.

The detector will be deployed in the Greenland ice. That means the hardware has to resist extreme low temperatures and temperature changes have to be considered (see section 4.5).

The weather at Summit Station is harsh and reaches very low temperatures. The climate is polar with a daily maximum temperature of about -10 °C in summer (July) and -35 °C in winter (January). The minimum temperature in winter is around -45 °C. [94]

In order to be prepared for these weather conditions the amplifier boards were all examined in a temperature chamber. Most important was to make sure all boards survive extreme low temperatures so every board had to pass a stress test. In the case of bad solder joints or chips the boards were expected to not work after the test.

For the stress test the boards were put without their enclosures in a temperature chamber, which was then cooled down to -40 °C. After they reached the targeted temperature it was waited until the boards had warmed up again to room temperature, the boards were not reheated by the temperature chamber. After that another function test was done.

All IGLUs were additionally cooled down five times in a row to -50 °C as the IGLU boards have to resist colder temperatures than the DRABs and SURFACE boards since they will be located in the boreholes deep in the ice not in the DAQ box on the surface.

All boards survived the stress tests: they worked before and after the temperature drop. Therefore a weather related failure after the deployment in Greenland is unlikely.

The IGLU boards showed the same current draw before and after the stress test in the temperature chamber which can be seen in figure 4.1.

All boards are labeled with an object number on the enclosure for identification

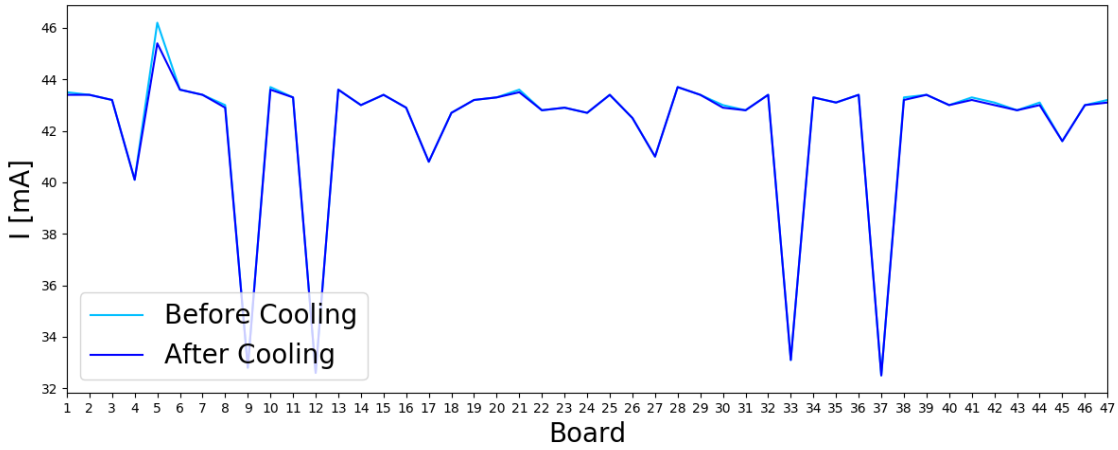

Figure 4.1: IGLU board function test: the measured current of the IGLUs before and after the boards were in the temperature chamber.

(see section 4.1). On the labels printed are the object number and a QR-Code for simple handling in the planned RNO-G database and for automated testing.

These labels, sticked on the enclosures, were also tested to make sure they would stay attached to the housings and remain readable after staying a long time outdoors in Greenland. The used cryogenic labels are according to the manufacturer (*labid*) waterproof, can sustain repeated freeze-thaw cycles and are meant for laboratory use in freezers and liquid nitrogen to extreme temperatures (-196 °C to +70 °C). They stayed in the temperature chamber at -75 °C for about 31 hours attached to a piece of aluminum and sticked on a board to guarantee the labels get not detached at extreme cold temperatures. Additionally they were put for about two days under an UV-lamp to make sure the used ink is not in risk of fading away in the foreseeable future.

4.3 Performance Tests

After the functionality and temperature resistance of the boards were verified the performance tests focused on characterizing the different board types and on studying their uniformity. Functioning boards with unwanted features or boards that differ very much from the other ones could be identified.

The transmission and reflection characteristics were studied by measuring the S-parameters of all boards. The focus hereby lay on the amplifiers' gain measurements and their variation. Furthermore the group delay of all boards was measured. The crosstalk and the noise figure of a few boards was determined to study signal disturbance.

Connector	3.5 mm
Cal Kit	85521A
Port 1	Female
Port 2	Female
Cal Types	SOLR

Tables 4.2: Calibration settings for cal kit 85521A.

All tests were done with a vector network analyzer (Keysight Technologies: *P5020A Vector network analyzer, 9 kHz to 4.5 GHz*). First of all a calibration with the two cables which are used to connect port 1 and port 2 to the input and output of the boards had to be done (*Response*, *Basic Cal*). The calibration settings for the used cal kit (Keysight Technologies: *85521A*) can be found in table 4.2. After this selection, the calibration is carried out by following the steps given by the program. The calibration can then be saved and is used (*Correction: On*) for all measurements. For measurements with port 3 and port 4 or for measurements with different cables, a new calibration has to be done.

After setting the receiver gain (*Setup*, *Internal Hardware*) for source port 1 and receiver port 2 to *Low*, the measurement selection can start. The frequency sweep settings (*Instrument*, *Quick Start*) are chosen for a *2-port S-parameter* measurements and can be found in table 4.3. Before each measurement the *Averaging* function is used (*Factor: 50*) to reduce the noise. All tests were performed with these settings.

Start Frequency	1 MHz
Stop Frequency	1 GHz
Center Frequency	500.5 MHz
Span Frequency	999 MHz
Sweep Type	Lin Frequency
Power	-60 dBm
IF Bandwidth	50 kHz
Number of Points	2001

Tables 4.3: Frequency sweep settings.

4.3.1 S-Parameter Measurements

The S-parameters of all channels of all SURFACE boards were measured. As well as all channels of all DRABs were measured with the same IGLU board. For

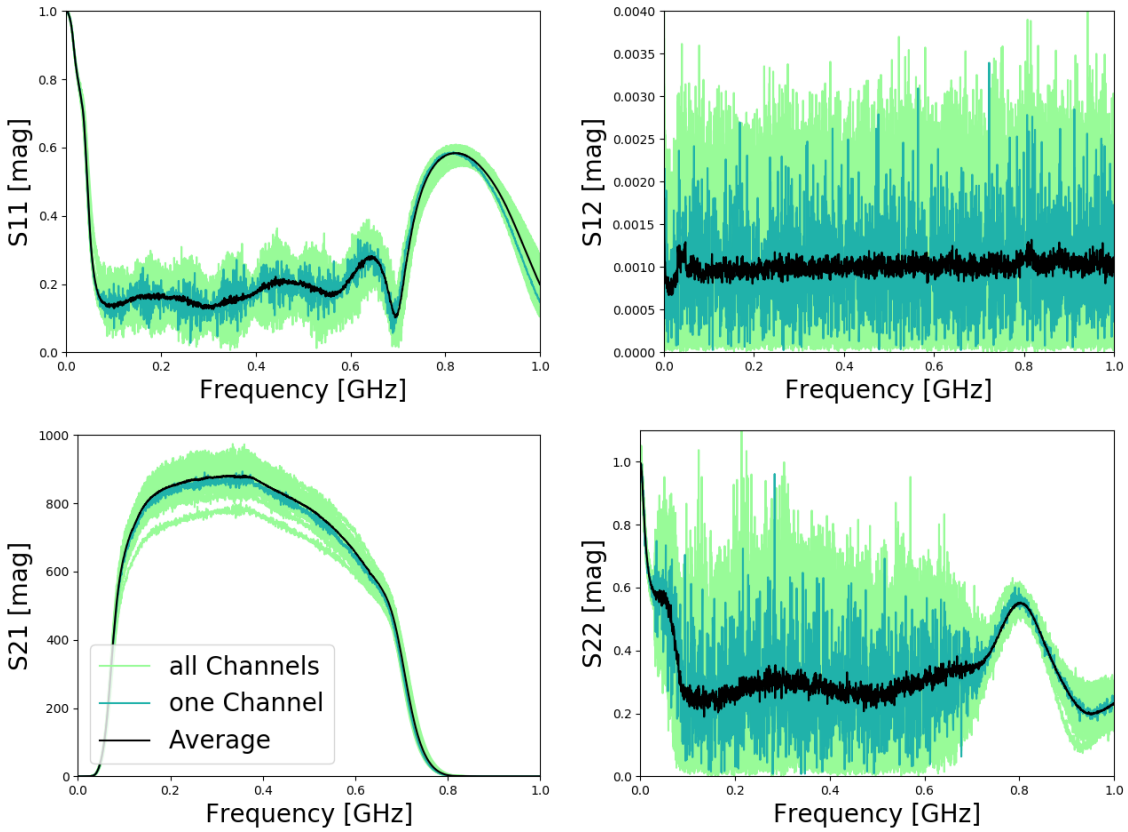

Figure 4.2: S-parameters of the SURFACE boards [mag]. All reflection and transmission measurements of all 12 SURFACE boards and their average.

measurements with different IGLUs see section 4.4.3.

In figure 4.2 (linear form) and in figure 4.3 (logarithmic form) are the same S-parameter measurements of all SURFACE boards in different forms.

In figure 4.4 (linear form) and in figure 4.5 (logarithmic form) are the S-parameter measurements of the DRABs measured with the same IGLU.

Displayed are in both figures: The measurements of all boards, to show the variation between the individual boards, the S-parameters of one single channel, to show a typical measurement and the average of all boards.

A bandpass filter suppresses the frequencies outside the passband (80 MHz to 700 MHz). Lower frequencies are suppressed to decrease galactic radio background noise radiation while higher frequencies are suppressed because of the LTE data transfer at 880 MHz, that RNO-G uses.

All measurements of one board type - SURFACE or DRAB - look quite similar, within some variation. For the SURFACE boards the variations are always below

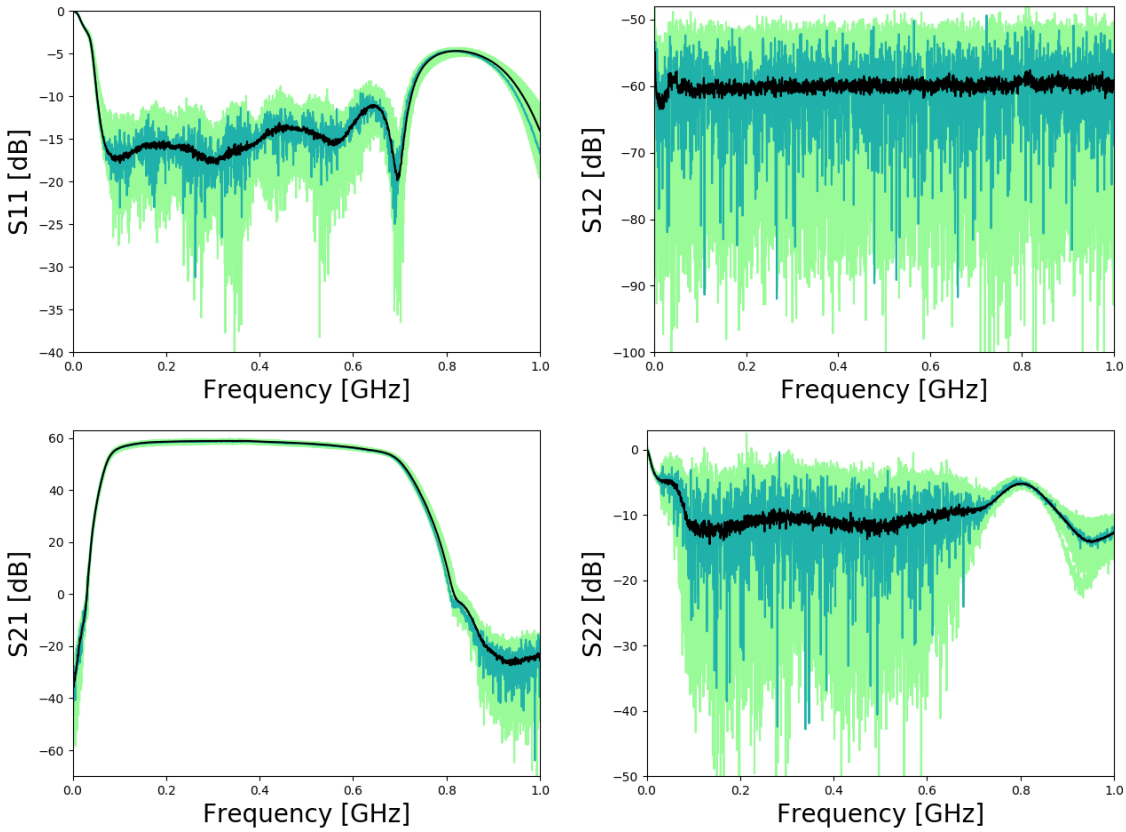

Figure 4.3: S-parameters of the SURFACE boards [dB]. The same measurements as in figure 4.2 in logarithmic form. The passband of the gain (bottom left) is very even and flat.

10 %, the measurements of the DRABs vary in the same range, but the gain of several boards deviates more than 10 %, but below 20 % (see section 4.3.2). Only one SURFACE board channel clearly has a lower gain (S_{21} measurement) than the other channels.

The input reflection coefficient S_{11} and the output reflection coefficient S_{22} describe how much the amplifier input and output differ from each other due to signal reflection losses. A low value indicates that the input signal is hardly reflected at all.

The reflection coefficients S_{11} and S_{22} are quite low in the passband between about 100 MHz and 700 MHz. In the case of the SURFACE boards the reflection at port 1 and port 2 is of similar height in the passband. In the case of the DRABs the reflection at both ports is of comparable size, but varies a bit more.

For a passive bidirectional device the backward transmission coefficient S_{12} would

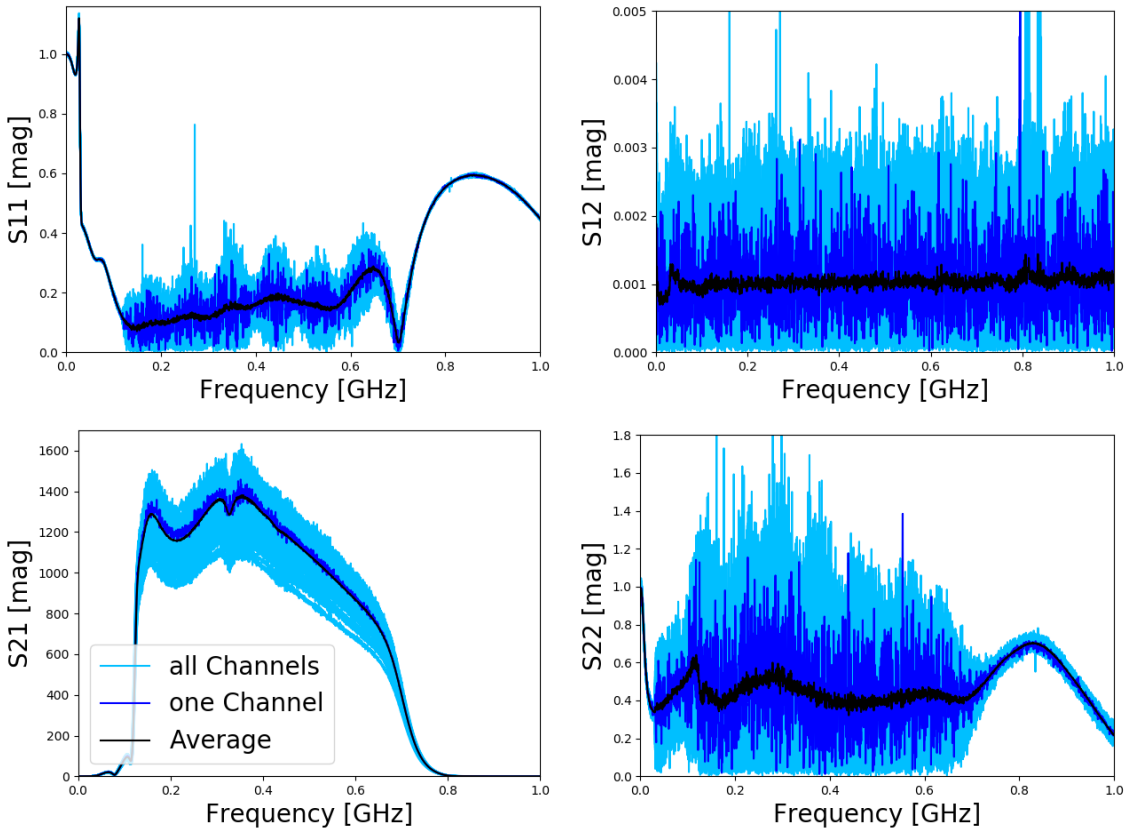

Figure 4.4: S-parameters of the DRABs [mag]. All reflection and transmission measurements of all 23 DRABs and their average measured with the same IGLU.

correspond to the forward transmission coefficient S_{21}, but not in the case of an amplifier. Forward transmission (S_{21}) describes the amplification or attenuation of the input signal. In the case of a passive device: the insertion loss. In the case of an amplifier - like in these measurements - S_{21} describes the gain of the amplifier. Would the input and the output port be absolutely isolated from each other, the S_{12} parameter in linear form would be zero. The backwards transmission from port 2 to port 1 (S_{12}) is for both board types very small, but not zero since the isolation of a practical amplifier is finite.

Apart from the one channel that has a lower gain than the others, the S_{21} measurements of the SURFACE boards show uniformity and have a gain of about 59 dB. The gain of all DRABs is a bit less uniform and varies between 61 dB and 63 dB. Characteristic for the DRABs is a small anti-resonance at 326 MHz which is featured in all gain measurements (see section 4.3.3). More details on the gain of the amplifiers can be found in the following section 4.3.2.

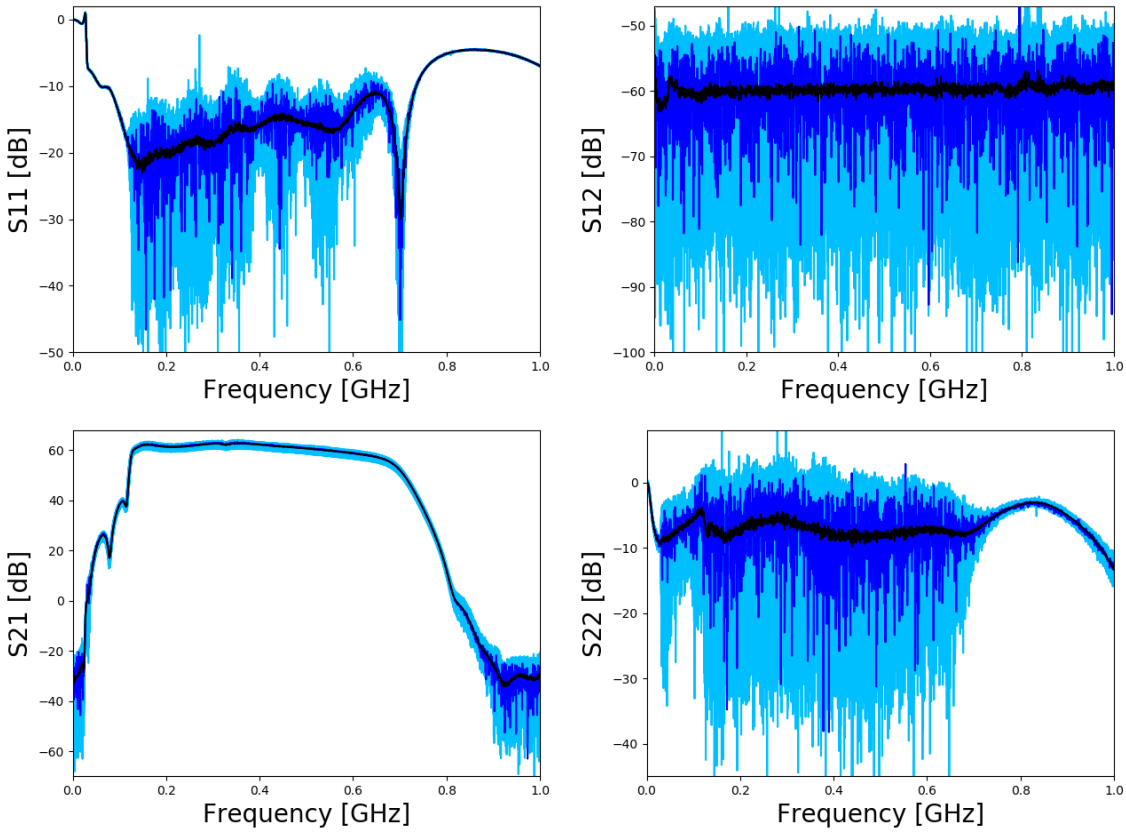

Figure 4.5: S-parameters of the DRABs [dB]. The same measurements in logarithmic form. The gain of the DRABs (bottom left) features a small characteristic drop at 326 MHz.

Additionally the S-parameters of a board without its enclosure were measured. The measurement showed the same result: there was no recognizable difference in the S-parameter data of the measurement with or without an enclosure.

The first amplifier measurements with the VNA looked as expected. The S-parameter measurements show an overall high uniformity, with slightly better results from the SURFACE boards. Almost all channels of all DRABs and SURFACE boards are close to the average of all boards.

4.3.2 Gain Measurements

In the last section the gain of the SURFACE boards (about 59 dB) and the gain of the DRABs (between 61 dB and 63 dB) has been determined. To further analyze how much the channels of one board differ from each other and how large the deviation between all individual SURFACE boards and DRABs is, this section

examines the gain measurements of all boards in more detail.

In figure 4.6 are the S_{21}-measurements of six SURFACE boards shown. There is one figure for every board showing all five channels. Displayed are the gain measurements in linear form for board A0007 to A0012 (while board A0001 to A0006 can be found in the appendix figure 6.1.) The gain of all channels per board is in most cases quite similar. Only the gain of channel 5 of board A0007 is clearly lower then the other ones. Channel 4 of the same board has instead the highest gain of all boards. This board already stood out during the function test with the same channels showing the same behavior: channel 4 had the highest, channel 5 by far the lowest signal.

In figure 4.7 are the S_{21}-measurements of six DRABs in linear form shown. All four channels of all 23 DRABs have been measured with the same IGLU. In this figure DRAB A0013 to A0018 are shown, (while DRAB A0001 to A0012 and A0014 to A0023 are included in the appendix figure 6.2- 6.4). In most cases the measurements of the different channels are still close together, but the uniformity of the down-hole amplifier boards is not as good as the uniformity of the SURFACE amplifier boards. This gain variance is assumed to be mostly due to the laser device-to-device variance. During the first S-parameter measurements the gain of the DRABs was lower than expected, between 50 dB and 55 dB for the different channels of the different DRABs. The DRABs were all measured with the same IGLU. Additionally the variations in the gain measurements of the different boards and the variation between the different channels of one board were greater. A repetition of the measurements brought the same result as did using a different IGLU.

Test measurements in Chicago contradicted the lower gain, therefore some error had to be in the test setup. The most prominent difference in the test setup was the used 10 m long fiber cable between the IGLU and the DRAB instead of the 1 m long fiber used in Chicago. Therefore the gain was measured again with two different fibers to check if the length of the used fiber has in general some influence on the gain or if maybe the first fiber was broken. The first fiber had a length of 10 m, next tested was a short fiber (3 m) and additionally a 50 m long fiber from the same fiber vendor who will also produce the fibers for Greenland. The tests showed clearly that the length of the fiber has no influence on the gain measurements, but that the first fiber (10 m fiber) was broken. More tests on the influence of the used fiber can be found in section 4.4.1.

The amount of variation in the passband, the passband ripple, of the gain determines the distortion of the signals passing through the amplifier. To check how much a transmitted signal gets deformed, the evenness of the gain over the range of different frequencies has to be studied. If the different frequency components are not amplified uniformly the signal gets distorted.

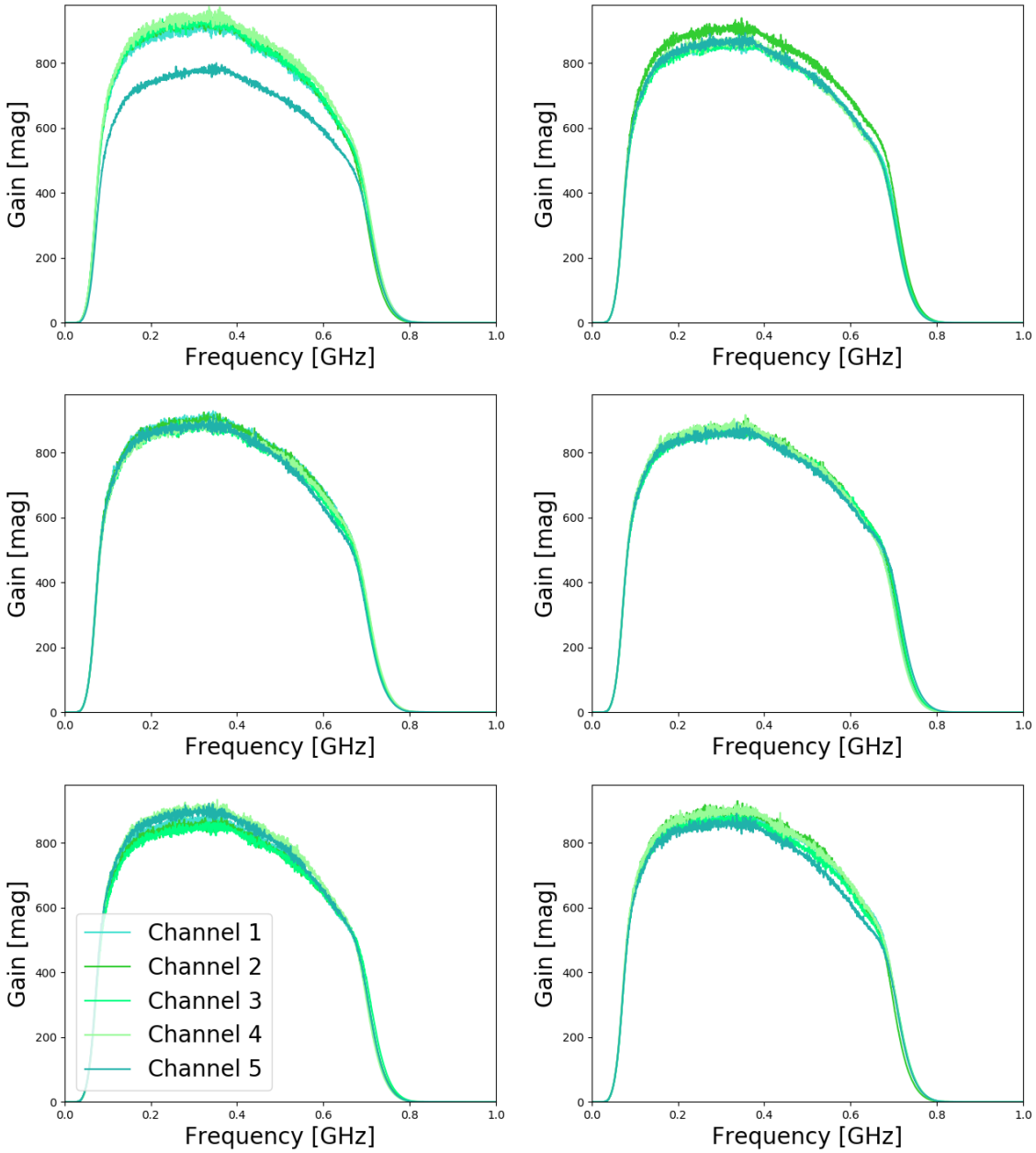

Figure 4.6: Gain of SURFACE boards [mag]: Board A0007 to A0012. Board A0007 (top left) has the least uniformity of all SURFACE boards with channel 5 having the lowest gain of all SURFACE boards.

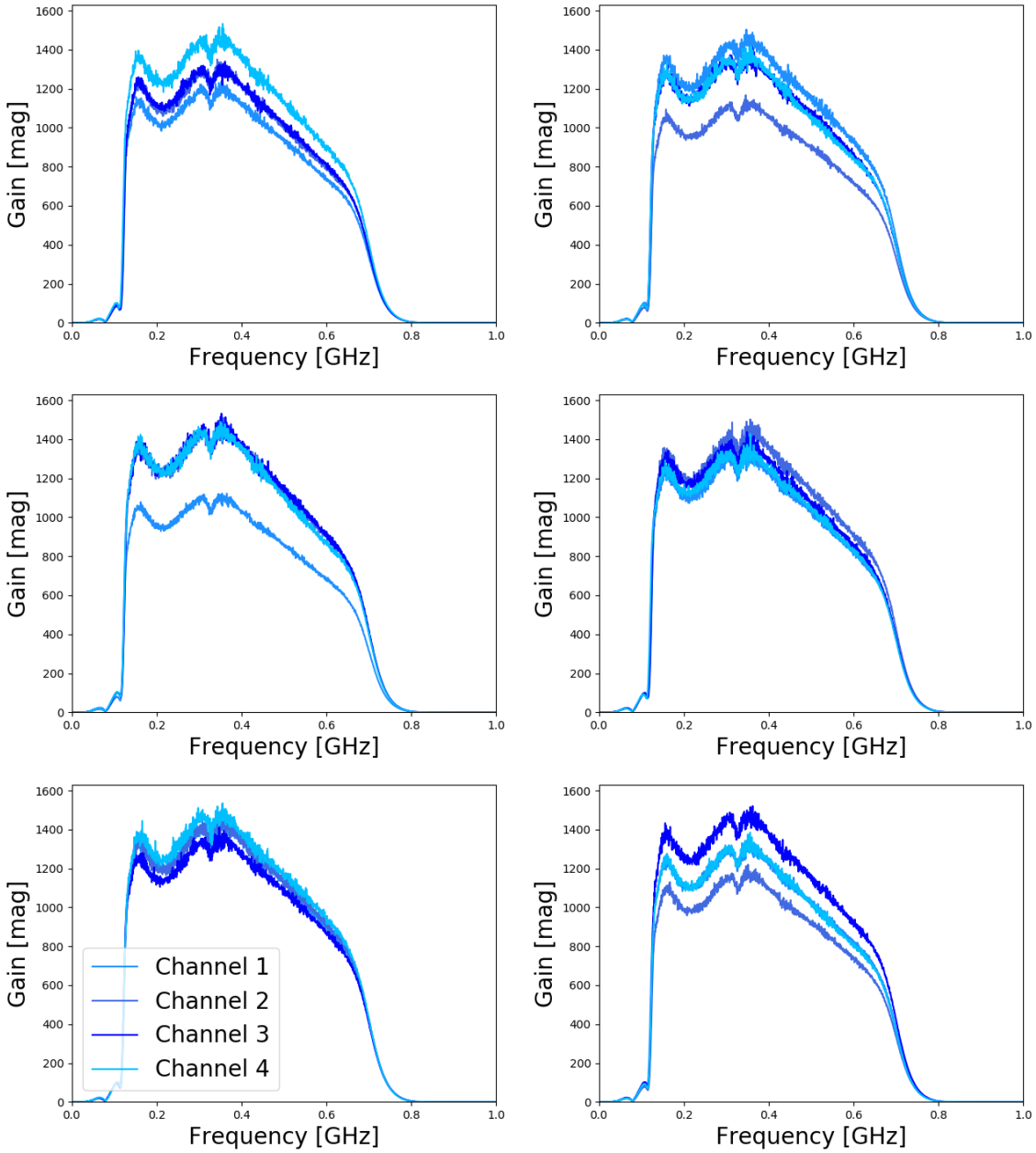

Figure 4.7: Gain of DRABs, all measured with the same IGLU [mag]: Board A0013 to A0018. The gain of the DRABs varies more than the gain of the SURFACE boards, with some boards having a greater spread than others.

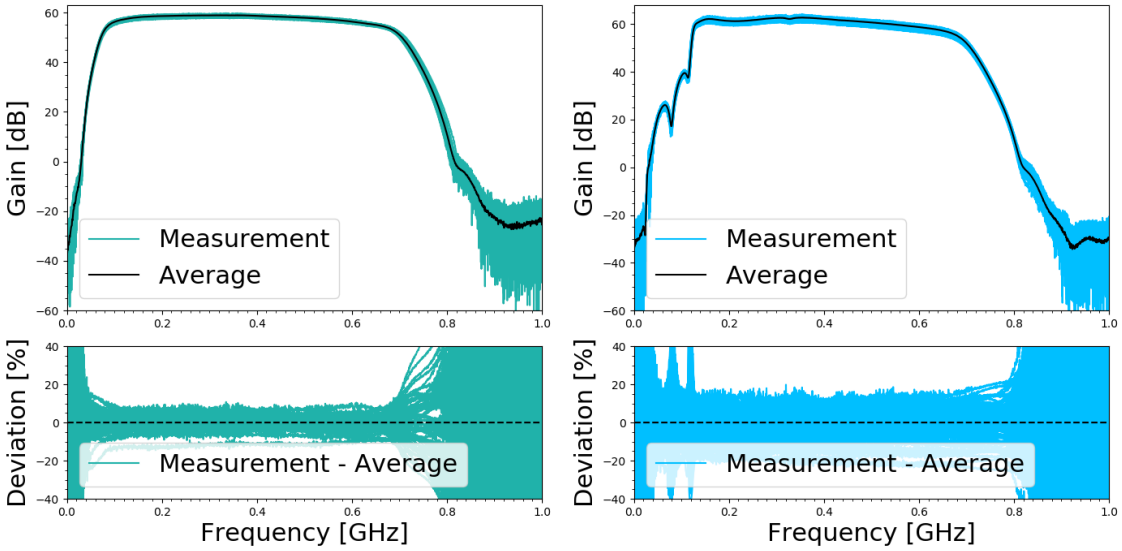

Figure 4.8: Measurement of amplifier boards: gain and deviation. Left: gain measurement in logarithmic form of all SURFACE boards and below the deviation from the average of all gain measurements in percent. Right: gain measurements and deviation of all DRABs tested with the same IGLU board using a 50 m fiber cable to connect the boards.

To understand the characteristics all amplifier boards of one board type share, the gain of all boards and all channels can be found, all together, in figure 4.8. This was done to examine the deviation from the average of the different channels and to study if all boards are in the same range or if some boards stick out. Furthermore the figures show: While the gain in the passband of the DRABs varies somewhat from unity, especially at 326 MHz, the passband gain is quite flat overall. The passband of the SURFACE boards even more. The transmitted signal therefore is not expected to get distorted very much.

Again prominent featured is the one SURFACE channel with the visibly lowest gain of all boards (board A0007 channel 5). Despite this channel the deviation is clearly greater in the DRAB measurements.

It also becomes clear that the anti-resonance at 326 MHz (see section 4.3.3) in the down-hole amplifier chain is either something all DRABs feature or that it originates from the IGLU board since all measurements feature it. The deviation below also shows, that the anti-resonance is the same for all boards since there is not a different deviation for any board at this frequency.

It was decided that the criterion to qualify as working board with an acceptable gain is, to lay within a ±2 dB range around the average gain of the boards.

As can be seen in the figure 4.8, the deviation for the SURFACE boards is of

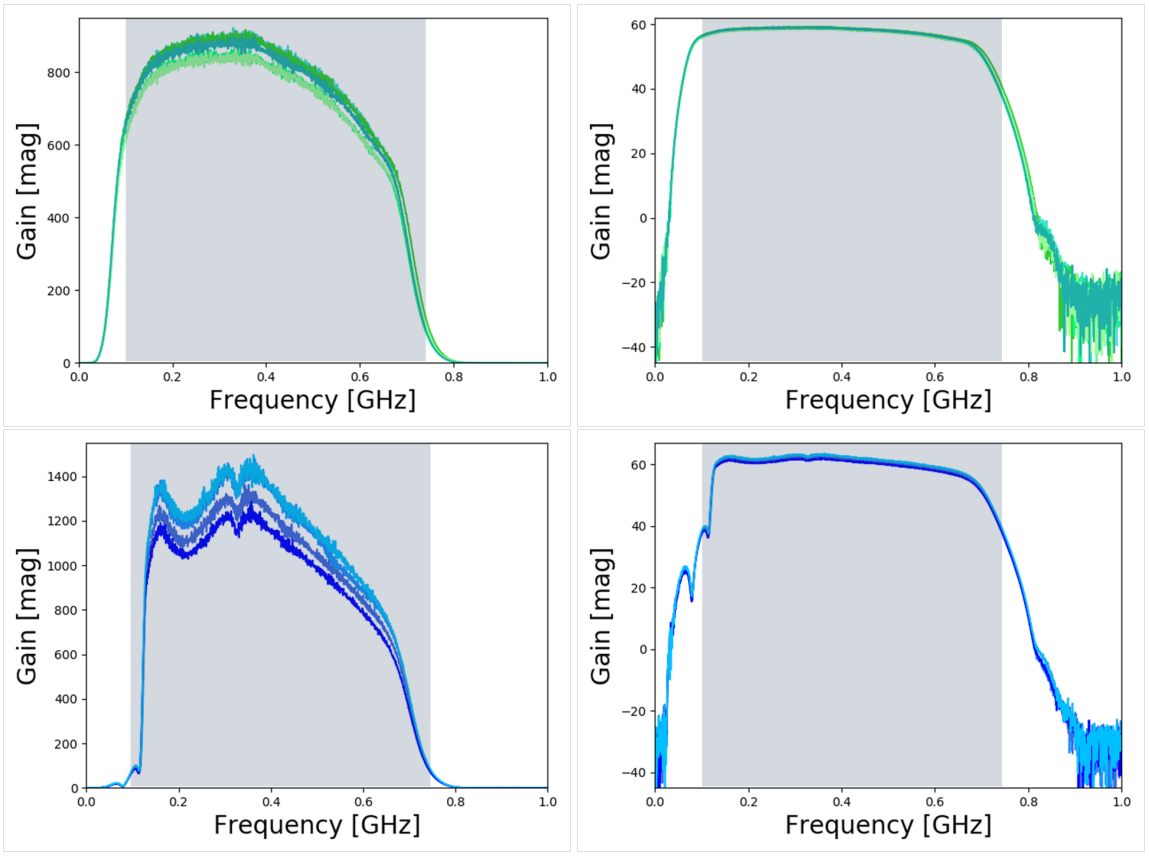

Figure 4.9: Gain of a SURFACE board and gain of a DRAB. Left: Gain measurement of a SURFACE board (top left) and of a DRAB (bottom left) in linear form. Right: The same measurement of the SURFACE board (top right) and of the DRAB (bottom right) in logarithmic form. In gray: Range between 0.1 GHz and 0.75 GHz for an analysis of the passband.

about 10 % (less than 1 dB) or smaller in the passband. Excluding the one channel with the lowest gain. While the deviation for most DRABs is a bit under 20 % (less than 2 dB) or smaller.

To further analyze the deviation of the gain, a closer look on the range between 100 MHz and 750 MHz was taken. This was done to see how big the differences between the channels (and boards) exactly are, by determining how much each channel differs from the average in the passband. The best way to represent this seemed to be the deviation from the average in percent or decibel. In figure 4.9 is the frequency range of interest (between 100 MHz and 750 MHz) marked in gray in the gain measurements of a DRAB and a SURFACE board. The following figures show the deviation from the average in percent. For all boards the deviation has

been calculated by dividing the gain measurement $\text{gain}_{\text{measured}}$ minus the average of all gain measurements by the average of all gain measurements:

$$\text{deviation } [\%] = \frac{\text{gain}_{\text{measured}} - \text{average(gain)}}{\text{average(gain)}}. \tag{4.2}$$

In figure 4.10 is the deviation in the passband of the SURFACE boards A0007 to A0012 in percent depicted. Board A0001 to A0006 as well as the measurements of all boards in decibel can be found in the appendix, figure 6.5 - 6.7. Most of the boards in this figure have, up to about 700 MHz, a deviation from the average gain of about 5 % (about 0.5 dB). As before shown channel 5 of board A0007 deviates the most from the average. This was already observed in the gain figures of all boards. The SURFACE board with the lowest and highest gain and therefore the greatest deviation, board A0007, shows a deviation of over 10 % (about 1 dB).

Figure 4.11 shows the deviation from the average gain of the DRABs A0013 to A0018 in percent. Board A0001 to A0012 and board A0019 to A0023 as well as all measurements in decibel can be found in the appendix, figure 6.8 - 6.14. The figures display that most gain measurements differ about 10 % from the average, with a maximum of about 20 % (about 2 dB). Since the criterion to qualify as working board with an acceptable gain is to lay within a ± 2 dB range around the average gain of the boards, most boards pass this criterion easily. All SURFACE boards have a far lower deviation and only DRAB A0011 and DRAB A0015 have a deviation of about 2 dB. The measurements have shown that the gain of all boards is quite flat and even in the passband, especially in the case of the SURFACE boards. Overall the gains of the different boards almost all spread within an acceptable range (less than 2 dB deviation from the average), the boards show a great uniformity. Nonetheless, all amplifiers will be calibrated individually in order to reduce systematic uncertainties on the reconstructed signals.

4.3.3 Group Delay Measurements

Group delay is the derivative of the unwrapped phase of the S_{21} parameter. The area of interest is the range between about 200 MHz and 600 MHz. Since the unwrapped phase in this range is quite even, the group delay is expected to be relatively continuous.

For a group delay measurement with the VNA just the measurement *Format* for the S_{21} parameter has to be changed to *Delay*. Therefore, the S-parameter measurements and the group delay measurements can be carried out together: After the channel has been connected to the VNA, the S-parameters are measured first. Then the format is changed and the group delay of the channel is measured. The procedure then continues for the next channels.

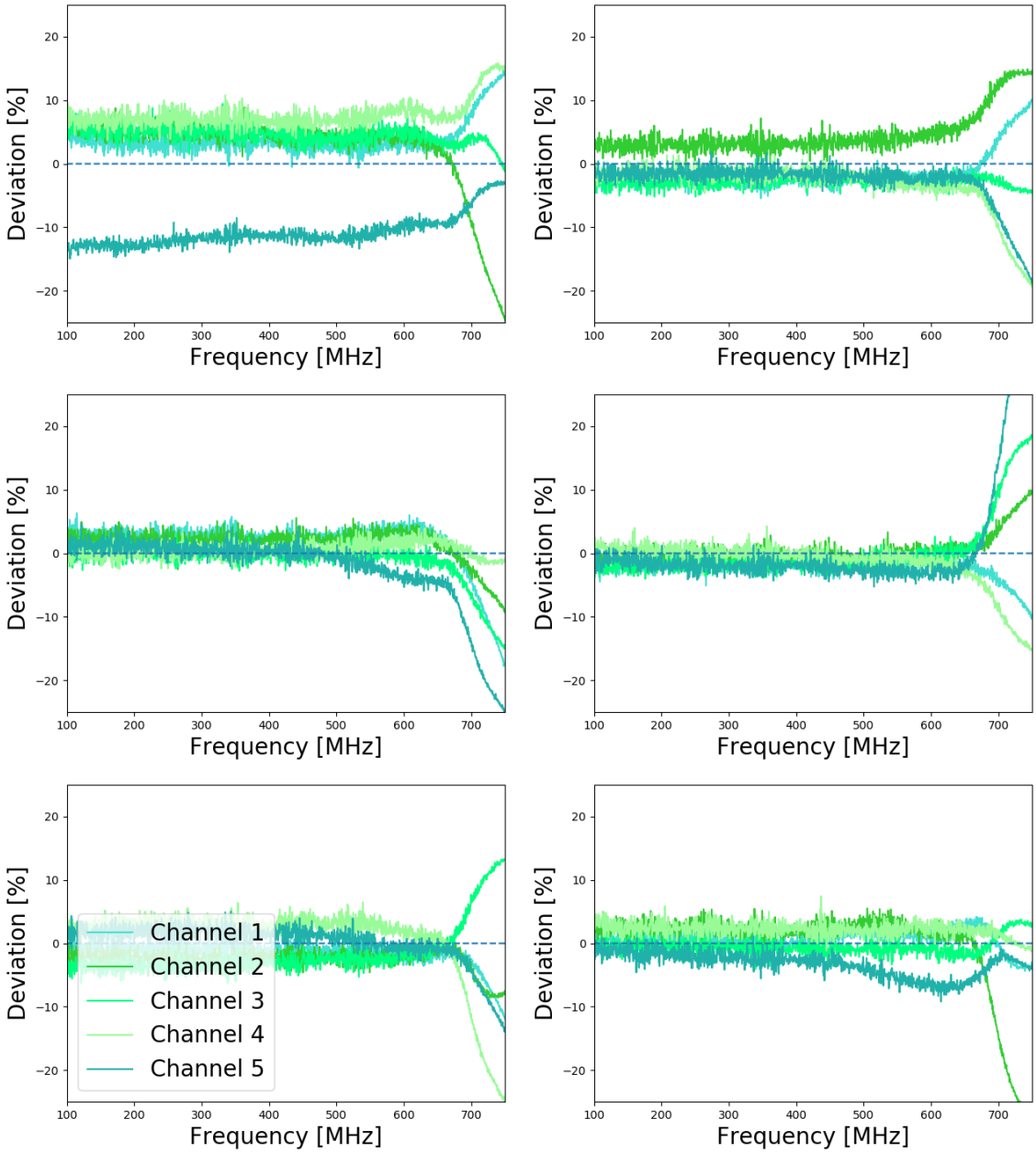

Figure 4.10: Deviation from the average [%]. Top left to bottom right: Gain deviation of board A0007 to board A0012. Noticeable: Channel 5 of board A0007 (upper left) deviates the most from the average gain.

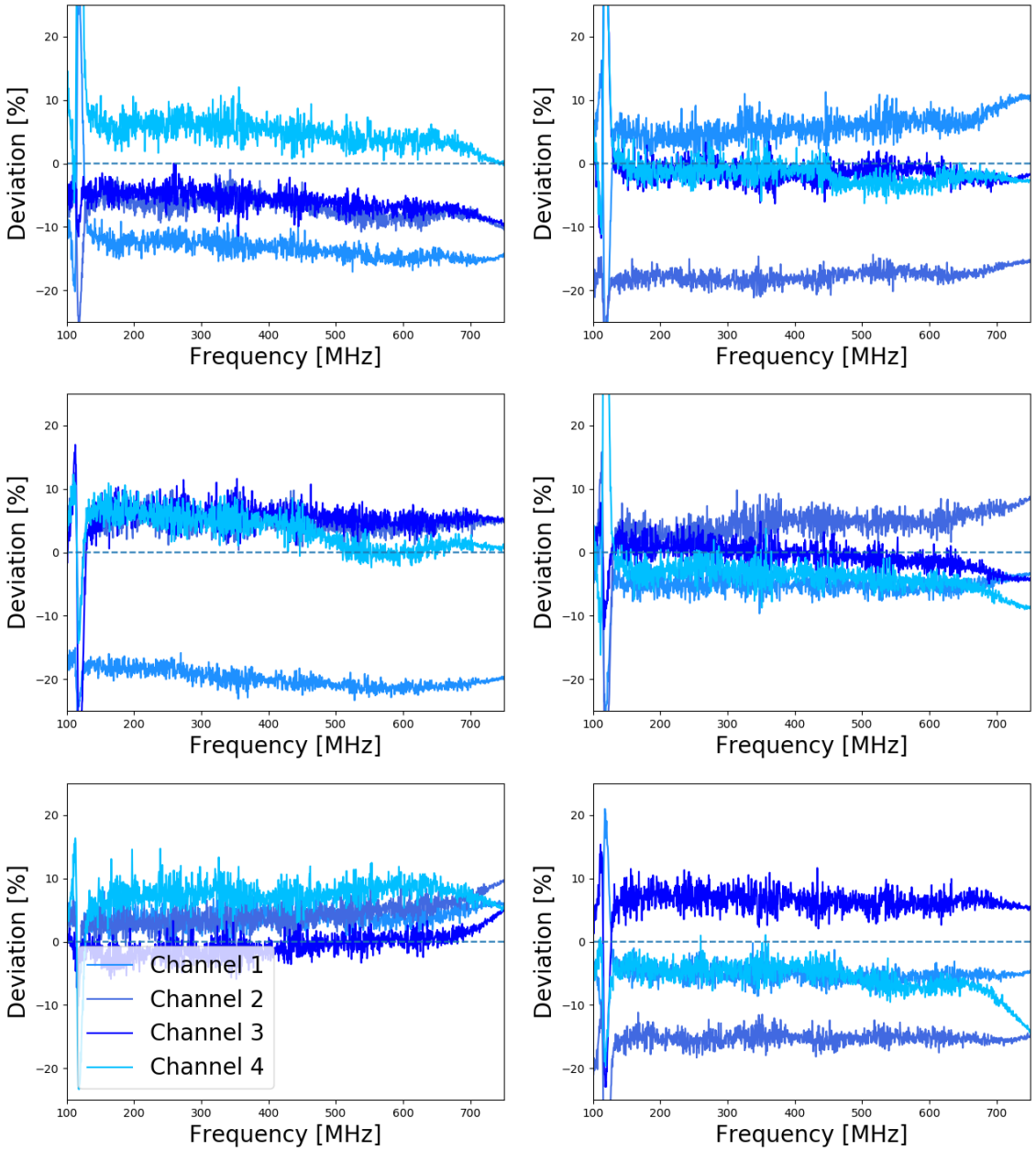

Figure 4.11: Deviation from the average [%]. Top left to bottom right: Gain deviation of board A0013 to board A0018. The gain of the down-hole amplifiers clearly varies more than the SURFACE board gain.

In figure 4.12 is the group delay for the SURFACE boards and for the boards of the down-hole signal chain. In the figures are all channels of all 12 SURFACE boards and all 23 DRABs measured with the same IGLU, they all look very similar and the frequency range of interest is rather even.

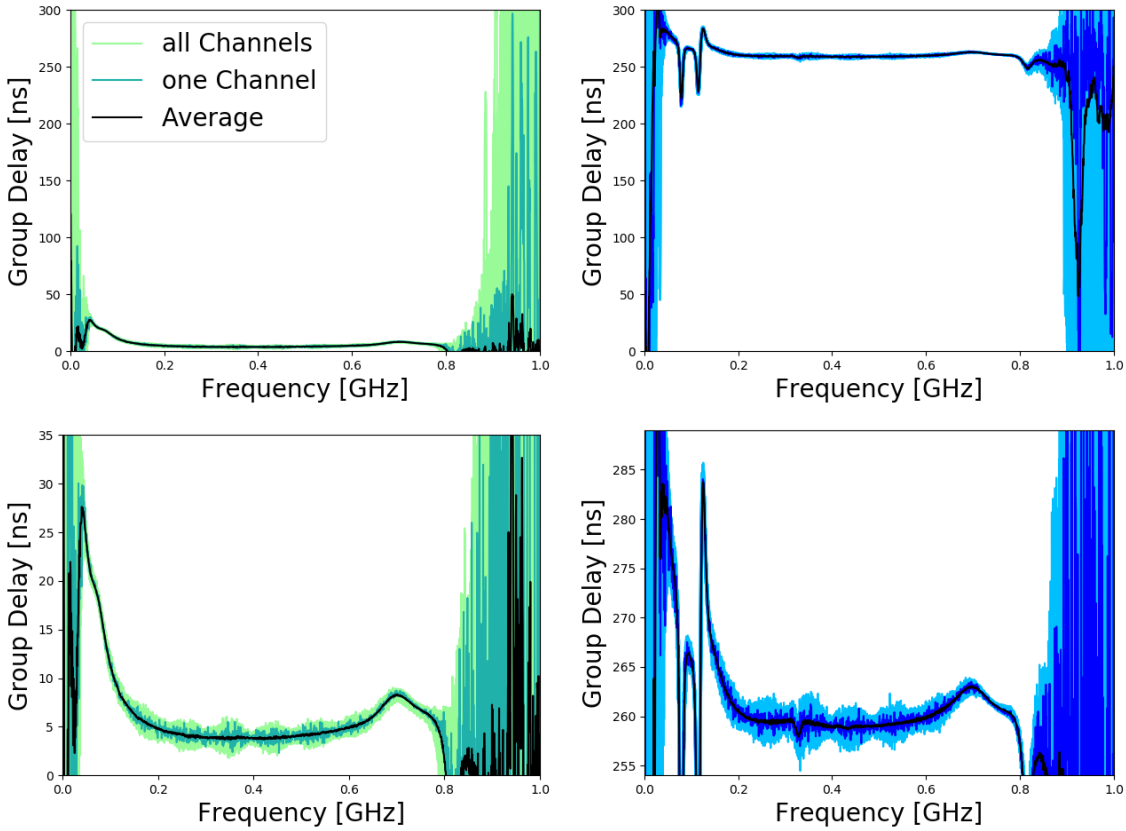

Figure 4.12: Group delay of the SURFACE boards and of the DRABs. Left: The group delay of all boards and all channels of the SURFACE boards, just on different time scales. In the frequency range of interest (about 0.2 GHz to 0.6 GHz) the delay time is about the same, the shape is relatively even. Right: All DRABs, measured with the same IGLU. And again the delay in the frequency range of interest is relatively constant. For the SURFACE board the group delay between 0.2 GHz and 0.6 GHz is about 5 ns, while the DRABs' group delay is about 260 ns. The long group delay of the DRABs is due to the long fiber that is used to connect DRAB and IGLU. On top of the delay times of the signal propagating through the amplifier boards, the travel time through the fiber gets added. Used for these measurements was the 50 m fiber. Measurements with the shorter fibers (3 m and 10 m) are shown in figure 4.19.

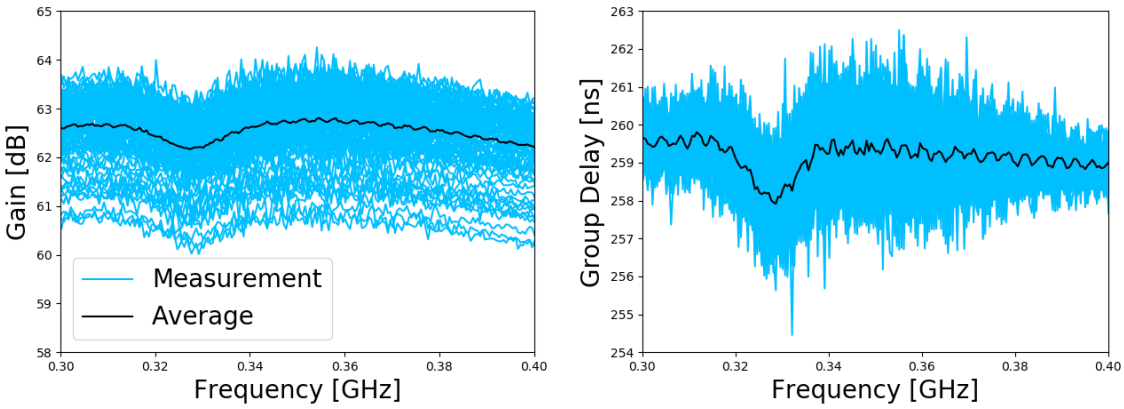

Figure 4.13: Anti-resonance at 326 MHz. Left: Zoom into the gain measurement of all DRABs to the drop of about 0.5 dB at 326 MHz. Right: Zoom into the group delay measurement. The small drop is of approximately 2 ns which is tiny compared to the band-edges (shown in figure 4.12).

The group delay for all boards of one board type is about the same and matches the expectations. The group delay is for all frequencies of interest similar, which was anticipated. If a board had a different group delay: something would be wrong with that board.

The delay in the passband is fairly uniform, this means, that the amplifiers do not cause much signal distortion. The frequency components in the passband are delayed for similar times and thereby the signal shape gets not changed not much.

Anti-Resonance in the DRAB Measurements

Noticeable in the group delay measurements of the DRABs is the anti-resonance at 326 MHz, featured in all DRAB measurements and which already appeared in the gain measurements. All gain and group delay measurements of the down-hole amplifiers feature this peculiar narrow anti-resonance at 326 MHz. All DRABs and all working IGLUs have been tested and the feature appears in all measurements independent of the used DRABs and IGLU boards.

In figure 4.13 are zooms into the gain and group delay measurements, showing the anti-resonance. Both figures show the data of all DRABs in their enclosures measured with the same IGLU. The unwanted drop is only of about 0.5 dB in the gain of the amplifiers, which is fairly tolerable.

The reason for the anti-resonance seems to come from the IGLU layout side. It has not been discovered yet what exactly on the board causes this issue. So far the source remains unknown. Tests in Chicago did not suggest that it originated in board design: changing laser-matching network inductor sizes did not move it at

all. A theory is that it is maybe somehow inherent to the laser.

Since the unexpected and unwanted feature is very small it is not seen as a big concern but nevertheless eventually finding out the reason for it is still a goal.

4.3.4 Crosstalk Measurements

The crosstalk measurements show how much signal interference should be expected in the data. The measurements were also studied to see how much the enclosures reduce crosstalk. Additional, the effects of the absorber foil, which is placed in the enclosures with the boards, was tested in these measurements.

To measure the crosstalk between the channels of one board, an input signal was applied to one channel and the gain of the other three (DRABs) or four (SURFACE boards) channels, without any input signal, was measured.

It was tested to what extent the crosstalk depends on the shielding of the boards. For that the crosstalk was measured one time when the board was not in the enclosure (*Bare*) and one time when the board was in its enclosure with the absorber (*Enclosure and Absorber*), as will be the case for all completed SURFACE boards and DRABs. To test the influence of the absorber foil some additional tests with the board while it was in its enclosure without the absorber (*Enclosure*) were done. In order to measure the crosstalk of a board in the enclosure (with or without absorber), the enclosure must be screwed. Otherwise, unusually high crosstalk signals can occur.

In figure 4.14 the crosstalk in four channels of a SURFACE board caused by the input signal at the remaining channel can be seen. Figures of the crosstalk caused by a signal in a different channel of this board are in the appendix, figure 6.15 - 6.18.

In figure 4.15 the crosstalk in the channels of a DRAB are pictured. The crosstalk measurements caused by the remaining channels are displayed in the appendix, figure 6.19 - 6.21.

In the cases of both board types (SURFACE board or DRAB) the crosstalk between the channels of one board when the board was not in the enclosure and the crosstalk while the board was in its enclosure were measured. The data was then compared to analyze the effect of the enclosures on crosstalk.

Every figure shows a gain measurement of a channel without input. Displayed are the measurements with and without an enclosure. Depending on the distance to the channel with an applied signal the height of the crosstalk changes for the measurements without an enclosure. While the measurements with an enclosure do not differ from the channels in greater distance, the signals in the *neighbor* channels of the channel with the input signal are considerably larger for measurements without an enclosure. While the board is not shielded at all, the signal is stronger in these channels than in the others.

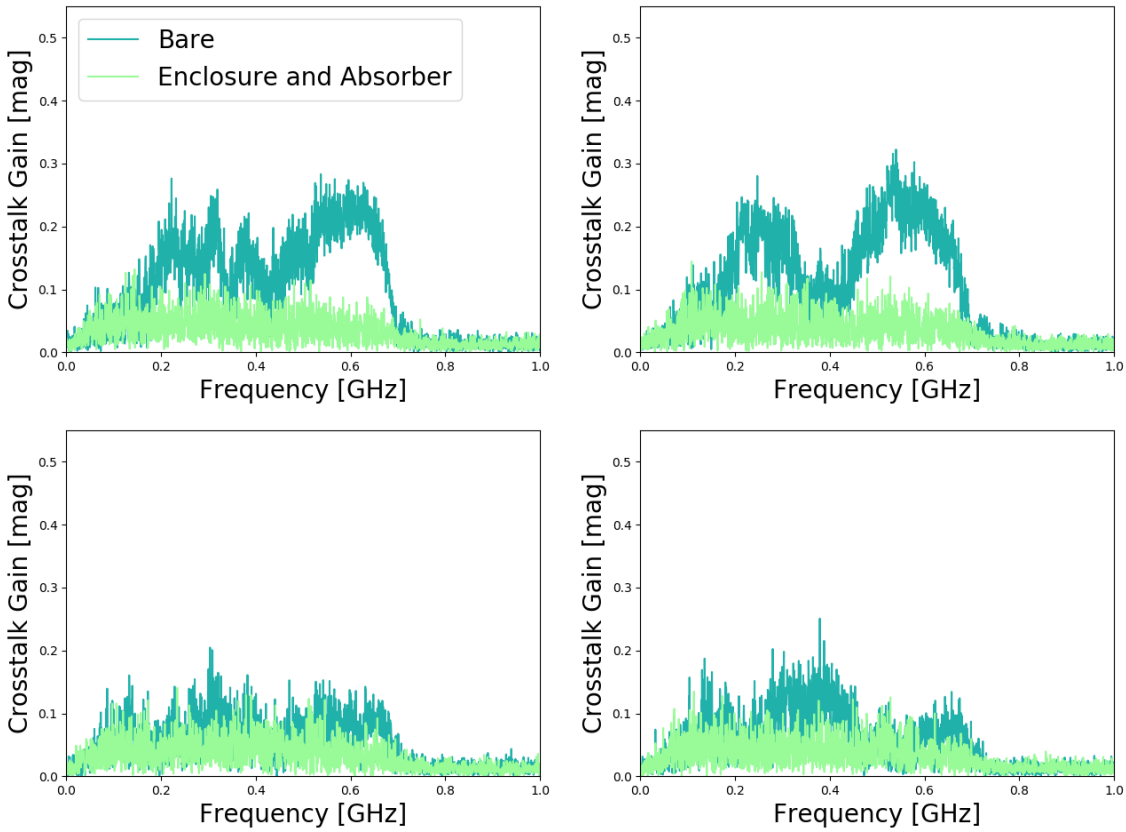

Figure 4.14: Crosstalk SURFACE board: gain measurement of channel 1, channel 3, channel 4 and channel 5. While a signal was applied to channel 2, the output of the other channels was measured. Due to crosstalk the output of these channels was not zero. But only a small signal was measured, additionally shielded by the enclosure. The neighbor channels (channel 1 and channel 3) show a stronger signal but only when measured without the enclosure.

The crosstalk while the board was in the enclosure is clearly smaller and the neighbor channels no longer show a different behavior than the other channels: The crosstalk in these channels is not greater, but about the same as in the other channels.

Accordingly: While the board is not shielded in any way, the crosstalk is clearly higher than in the case when the board is in its housing. Therefore the enclosure works as a shielding against interfering signals of other channels, so the signals are smaller with the board in the enclosure.

Figure 4.16 also displays the crosstalk in the DRAB channels. In this case the influence of the absorber was tested additionally. Crosstalk figures of the remaining channels are in the appendix, figure 6.22 - 6.24.

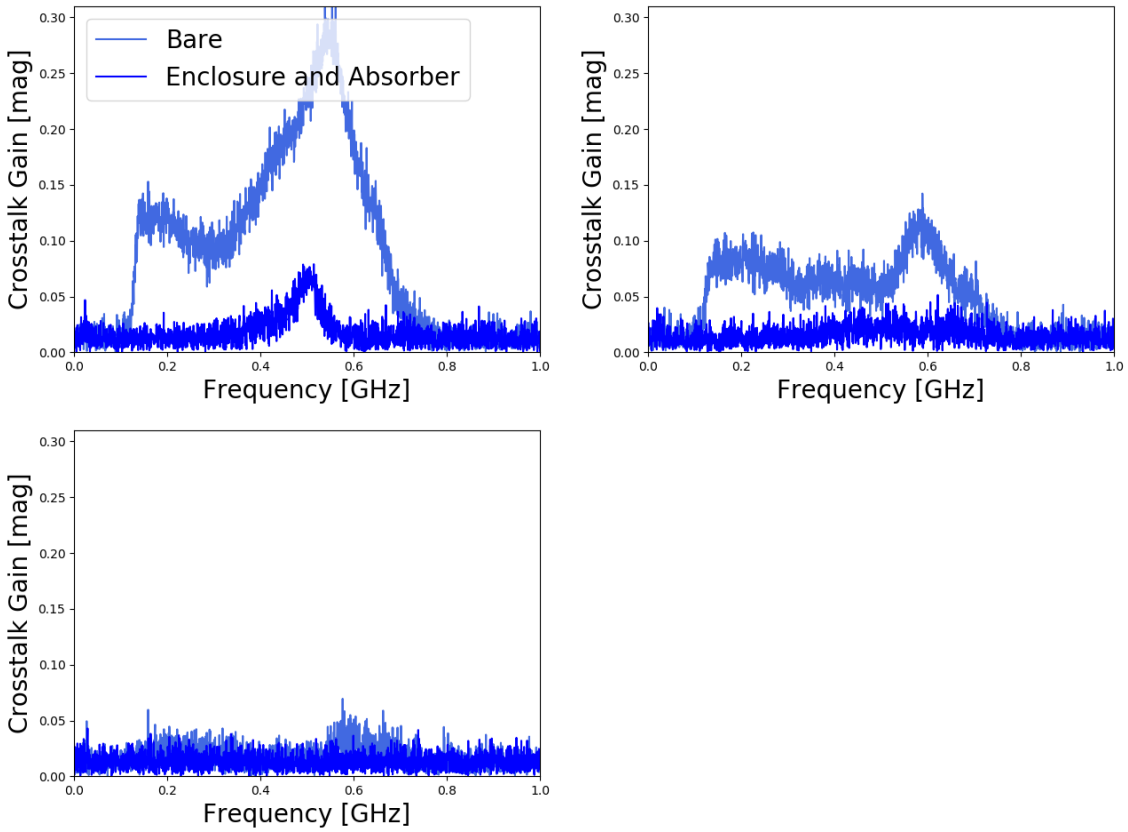

Figure 4.15: Crosstalk DRAB: gain measurement of channel 1, channel 3 and channel 4. While a signal was applied to channel 2, the output of the other channels was measured. The neighbor channels (channel 1 and 3) show some crosstalk in the measurements without the board in its enclosure opposed to the channel in greater distance (channel 4) which barely features any crosstalk.

The difference in crosstalk between the board being in its enclosure with or without the absorber however is very small. In most cases both data look exactly the same, only in very few cases was the absorber measurement insignificantly smaller. Therefore, an effect of the absorber foil on the crosstalk can not be concluded. The main differences between measurements is really caused by the shielding the enclosures provide.

In the measurements of the different channels of the SURFACE board it occurs, that while the signal was applied to channel 1 (figure 6.15), channel 5 - not being a neighbor channel - is a bit higher than expected, compared to the other channels. It was expected that channel 3 and 4 would be higher or of about the same height. But the difference is very small.

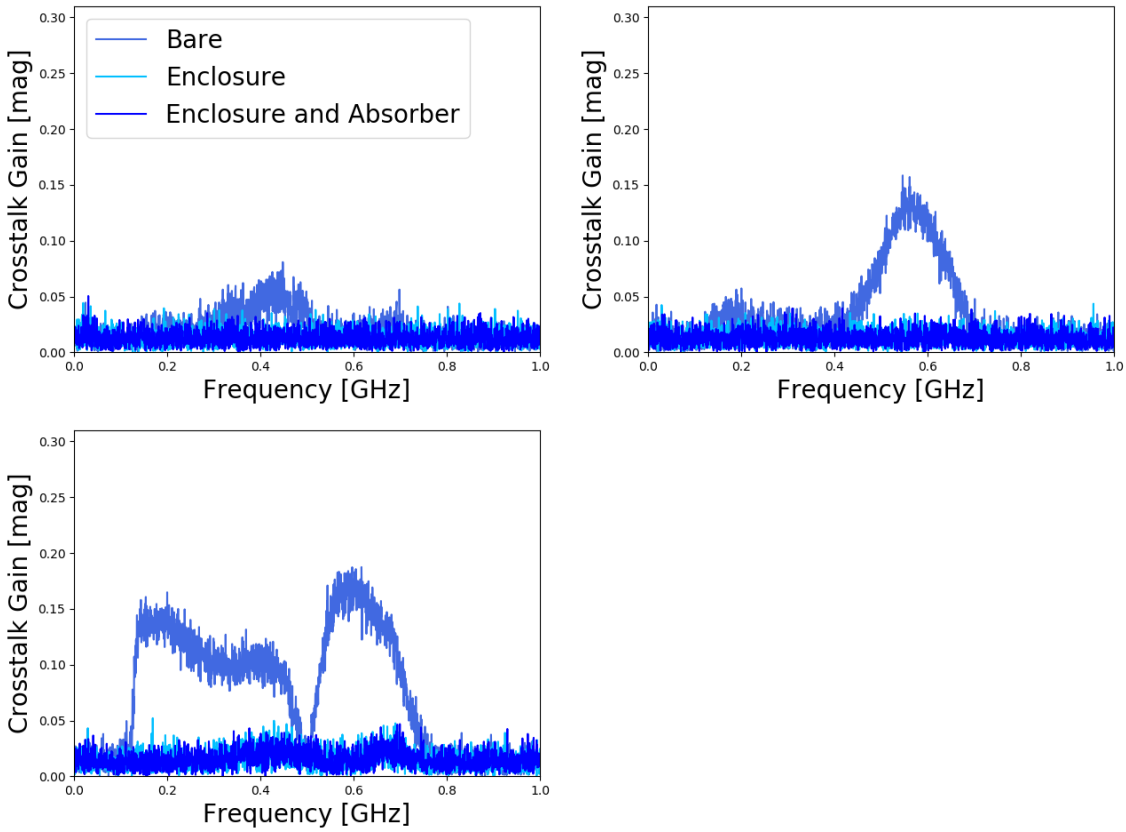

Figure 4.16: Crosstalk DRAB: gain measurement of channel 1, channel 2 and channel 3. While a signal was applied to channel 4, the output of the other channels was measured. The figure shows the influence of the enclosure and the absorber foil on the crosstalk: the measurements with the bare board, the board in its enclosure and the board in its enclosure with an additional absorber are all displayed. The neighbor channels (channel 3) shows the highest signal for the case of no shielding. The absorber foil has no influence on the measurements.

The same holds for channel 1 in the crosstalk measurement of channel 4 (figure 6.17): The crosstalk in channel 1 is almost as high as in a neighbor channel. In the crosstalk measurement of channel 5 (figure 6.18), channel 1 shows a similar behavior.

In contrast to the measurements with the SURFACE board the neighbor channels in the DRAB measurements, when the board is in its enclosure, often show a signal that is a bit higher than for the other channels. But the signal is still very small.

As has been shown, the crosstalk clearly decreases for the measurements with the enclosures. But with the added absorber the crosstalk does not decrease any further. The tests of the absorber foil - measurements in the enclosure with and

without the absorber - showed no difference. Some single measurements seemed to show a slight influence of the absorber to shield the channels even more, but further tests did not confirm this.

Overall four SURFACE boards and two DRABs were measured inside and outside their enclosures. The DRABs have been tested additional in their enclosures without the absorber foil. All boards showed a comparable behavior.

In summary the enclosures prevent crosstalk, especially in the neighbor channels, as expected. While the aluminum housings provide a good shield for the individual channels against crosstalk, the additional absorber foil in the enclosures does not seem to have any influence on the height of the interfering signal.

4.3.5 Noise Figure Measurements

To further quantify the performance of the boards, the noise figure (NF) was measured, it describes the amount of noise the amplifier board adds to the signal transmitted through the board. The noise figure compares the signal to noise ratio (SNR) at the output to the smaller SNR at the input.

To measure the noise, the VNA's *Spectrum Analyzer* function has to be selected (*Instrument*, *Measurement Class*). In the *SA Setup* the *Sweep Type* is set to *Linear Frequency*. The used *Settings* can be found in table 4.4. The *Attenuator* of the used port is set to *Low Attenuation*.

Start	9.990000kHz
Stop	1GHz
Center	500.004995000MHz
Span	999.990010000MHz
Number of Points	2001

Tables 4.4: Noise figure settings.

First a measurement is done without any device, to get the noise at the input of the tested device. After that the VNA is connected to the output of the amplifier board and a new measurement is started.

The noise figure is the total noise output power P_{Nout} subtracted by the thermal noise input $N_{\text{in}}^{\text{th}}$ and the previously measured gain (see section 4.3.2) of the channel:

$$NF\ [\text{dB}] = P_{\text{Nout}} - (N_{\text{in}}^{\text{th}} + \text{gain}) \tag{4.3}$$

This method to determine the noise figure of a device with a VNA is called the *gain method*. [95]

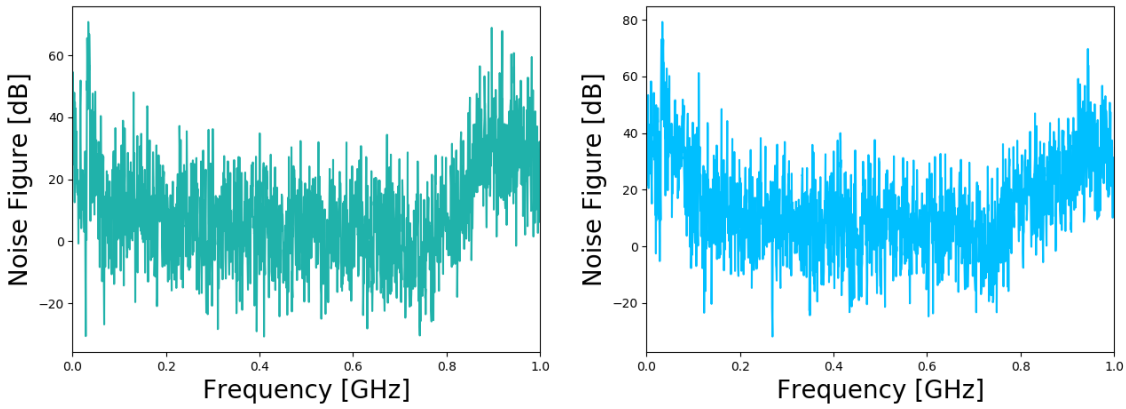

Figure 4.17: Noise figure measurements. The measured noise figure is unexpectedly high: Between 200-600 MHz the noise figure is about 4.48 dB for the SURFACE board (left) and about 7.78 dB for the DRAB (right). That would be a bad noise figure to have, expected was a noise figure better than 4 dB. The measured values do also not match the ones previously measured in Chicago (see figure 4.18).

But the noise figure measurements look odd (see figure 4.17) and the noise is a few decibels too high - higher than expected and higher than what has been previously measured in Chicago with a dedicated noise-figure meter (see figure 4.18). Smaller values indicate better performance and the expected noise figure was supposed to be in the range between 1-3 dB in-band (100-600 MHz). But between 200-600 MHz the noise figure for the different channels that were measured, was about 5 dB for the SURFACE boards and about 8 dB for the DRABs.

The reason for this could not be identified, but it is likely that something went wrong during the measurements or that some measurement settings were chosen wrong. Instead of the thermal noise, the measurement without any device (input noise) was used and no noise source was applied. Further measurements have to be taken to identify the reason for the incorrect results and to determine the mean noise figure of the boards.

4.4 Testing Different Parameters and Components

To study the influence of different components on the measurement results and the impact of the variation of certain parameters, different tests were done. That includes the testing of the used fiber cable in the down-hole signal chain between IGLU and DRAB. Furthermore, some measurements were repeated with the exact

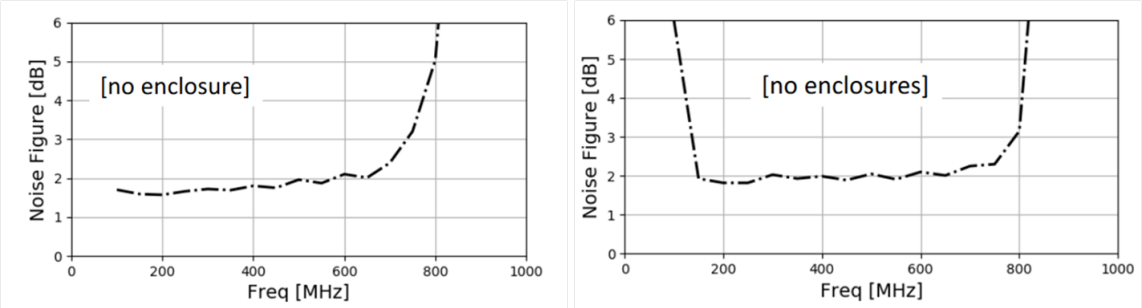

Figure 4.18: Previous noise figure measurements. The measurements were done with a noise figure meter of a SURFACE board (left) and a DRAB (right). The noise figure in the passband is below 2 dB (SURFACE board) or at 2 dB (DRAB).

same setup on different days to check for random errors. The influence of the used IGLU board on the gain of the down-hole amplifier chain was studied. Tests on the influence of the temperature on the measurements are described in section 4.5.

4.4.1 Fiber Influence

First, the influence of the used fiber cable in the down-hole signal chain between IGLU and DRAB was tested. This was done because the measurements with the first fiber did not turn out as expected: the measured gain was too low (50 dB to 55 dB). To check if the used fiber was broken or if the length of the fiber somehow influences the measurement, some of these measurements were repeated with a short and a very long fiber. The measurements with those fibers looked pretty similar and as expected: The gain was in both cases between 61 dB and 63 dB and the boards showed more uniformity.

In figure 4.19 are gain and group delay measurements of the down-hole amplifiers to compare the three different fiber lengths between the IGLU and the DRAB.

The shape of the group delay measurements (figure 4.19 (right)) is always the same, but due to the different lengths of the fibers, the delay time is of course different, since the signal needs more time to travel through a longer fiber cable. The three different fiber lengths were 3 m, 10 m and 50 m. The group delay measurement gives no indication of a defect: the measurements look as expected, the shape of the group delay is always the same, only the delay time is different.

The gain measurements with all fibers (figure 4.19 (left)) reveal, that the reason for the too low gain was a broken fiber in the first measurement and the length of the fiber has no influence on the gain. In the figure are the averages of all DRABs measured with the three different fibers compared. The gain measurements with the short and with the long fiber do not differ from one another, only the measurement with the broken fiber is significantly lower.

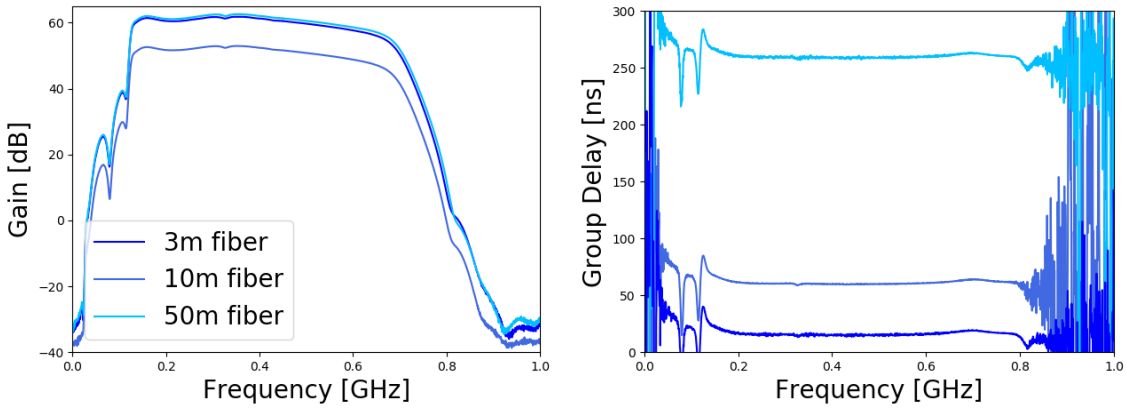

Figure 4.19: Fiber influence: Comparison of measurements with a 3 m fiber, a 10 m fiber and a 50 m fiber. Left: The average gain of all DRABs. The gain measured with the broken fiber (10 m) is clearly lower than the other measurements. Right: The group delay measurements of the different fibers have the same shape, but due to the different propagation times through the fibers, the delay time is shifted.

Additionally the deviation from the average of many boards is way higher for the broken fiber than in the measurements with the other two fibers: In figure 4.20 is the gain of all DRABs measured with one of the fibers and the deviation from the average. The measurements with the broken fiber show that the gain is clearly lower and the gain variation is greater compared to the other two DRAB measurements with the short fiber (3 m) and the long fiber (50 m). The gain and the deviation in these two figures look very similar.

4.4.2 Random Errors

Random errors are unpredictable and change between different measurements with the same setup and therefore they can not be removed by calibration. Knowing how many random errors are expected in a measurement helps to estimate how many deviations in a measurement are actually caused by the use of a different hardware component (different board or fiber) and are not caused by random errors. To check for random errors the gain measurements with the same boards were repeated.

In figure 4.21 are the gain measurements of all SURFACE boards done twice and the gain measurements of all DRABs done twice with the same IGLU.

It can be seen in the SURFACE board measurements that there is almost no difference at all, both are almost identical - which means the random error for the SURFACE boards is very low: below 0.1 dB (difference between the averages).

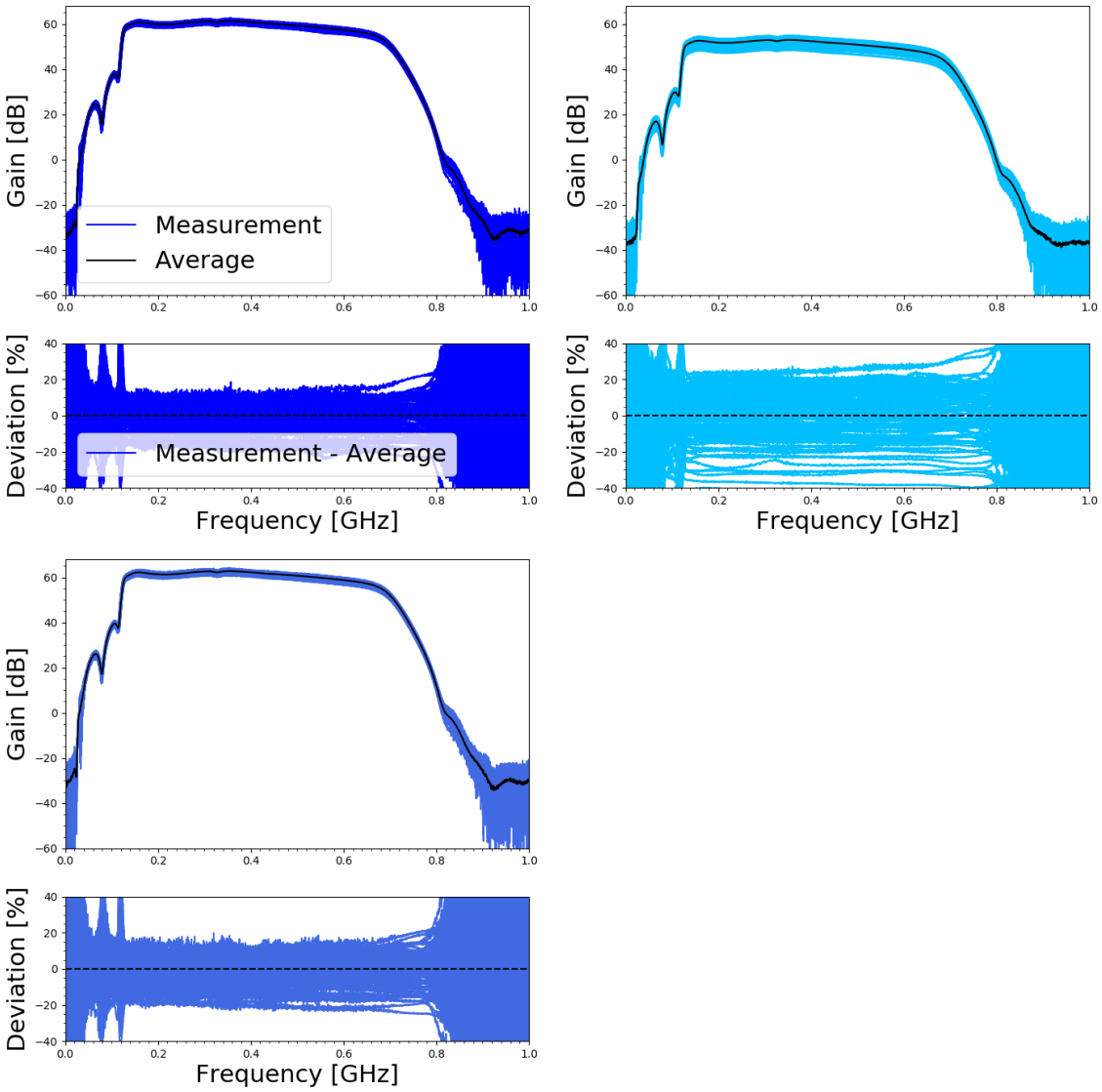

Figure 4.20: Fiber influence: Comparison of measurements with a 3 m fiber (top left), a 10 m fiber (broken, top right) and a 50 m fiber (bottom). In addition to the different gain values the measurement variation also spreads wider for the broken fiber, while the other two measurements show great uniformity and a gain of the same height.

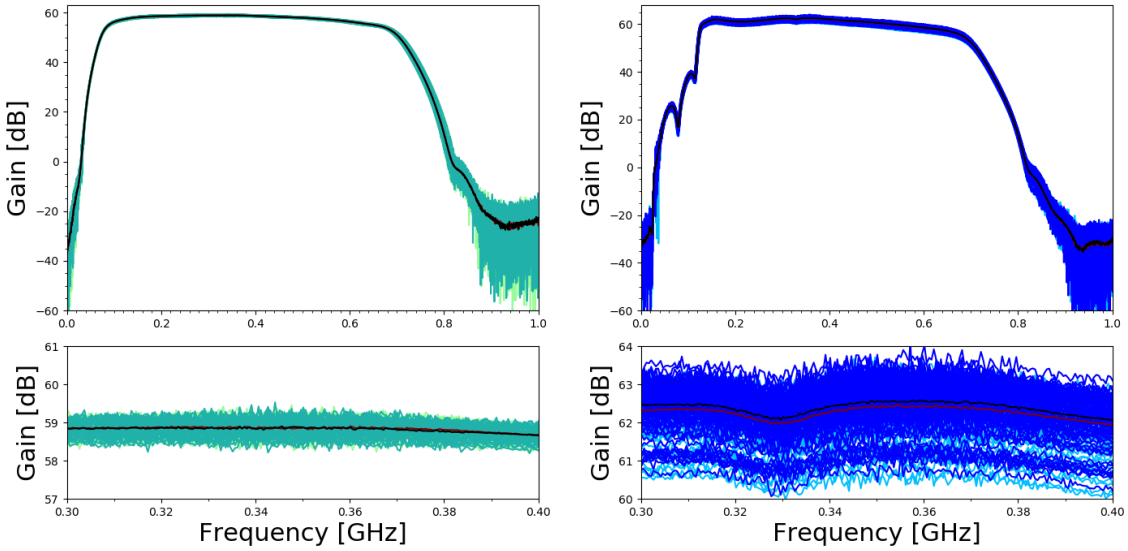

Figure 4.21: Random error. Left: All SURFACE boards measured twice and the average of both cases displaying (almost) no random error. Right: all DRABs measured twice showing some differences and a light shift of the measurement average.

Repeating the DRAB measurements showed a difference between the two measurements, but it is very small. The deviation between the two measurements is below 0.25 dB (difference between the averages). Since in this case there are two amplifier boards instead of one and more cables have to be connected to the downhole amplifier boards for each measurement, connector repeatability errors cause more differences in the DRAB measurements than in the SURFACE board measurements.

4.4.3 IGLU Influence

After analyzing the influence of the individual DRABs, by measuring all of them with the same IGLU, the IGLU influence was studied.

To understand the influence of the IGLU board on the measurements of the down-hole amplifiers, the gain of all IGLUs was measured with the same five DRABs (DRABs: A0001, A0006, A0007, A0008, A0020), which can be seen in logarithmic form in figure 4.22 and figure 4.23 (zoom). The gain in linear form can be found in the appendix figure 6.25.

All 43 working IGLUs have been tested: this includes the two fixed ones, which had shown no signal in the first function tests, while the four IGLUs with a too low current draw were excluded.

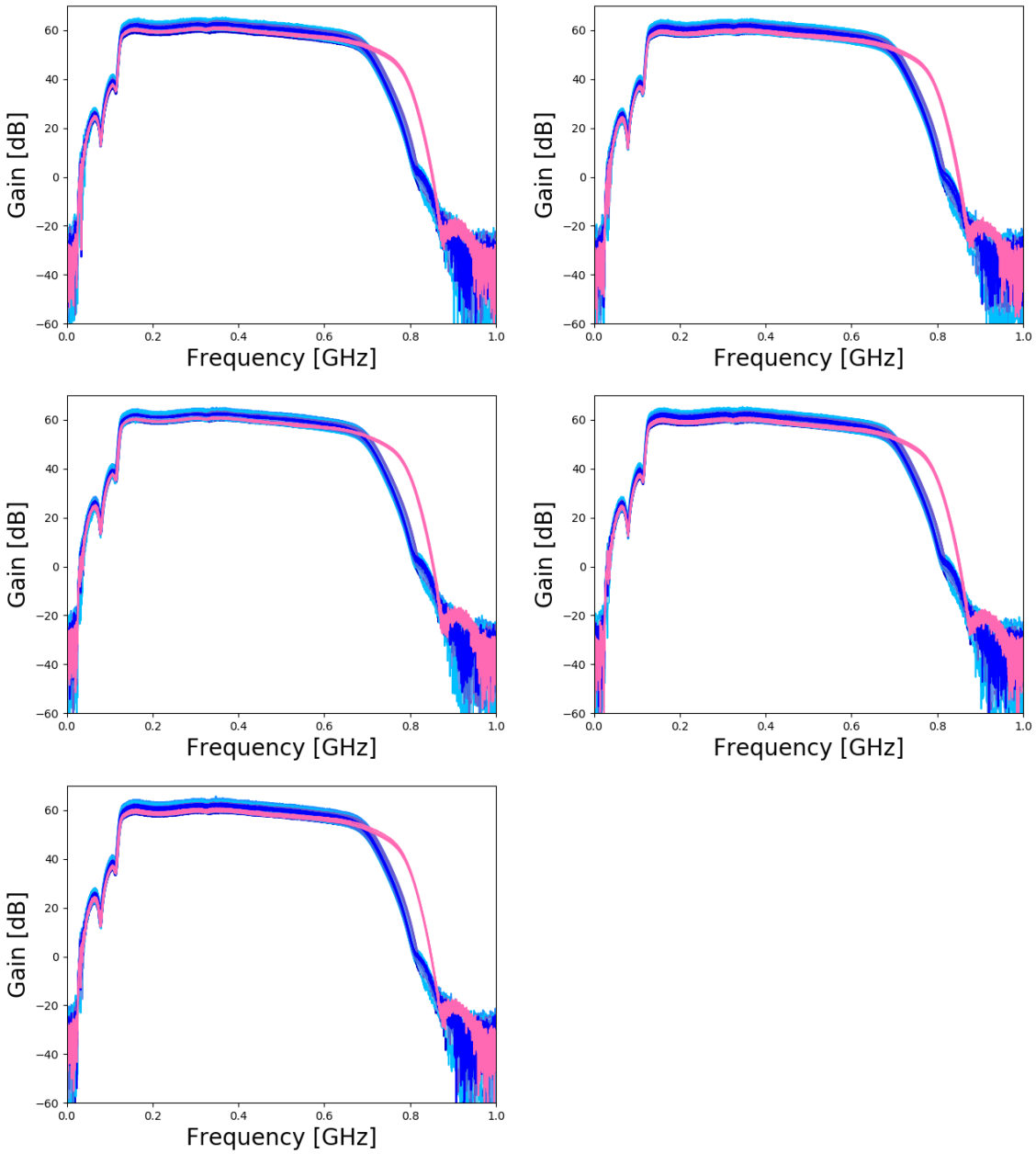

Figure 4.22: Influence of the used IGLU on the measured gain [dB]. The gain of five different DRABs measured with all IGLU boards displayed in logarithmic form. In pink the only IGLU to have a higher low-pass cutoff. The variation between measurements with different IGLUs is comparable to the variation due to the use of different DRABs.

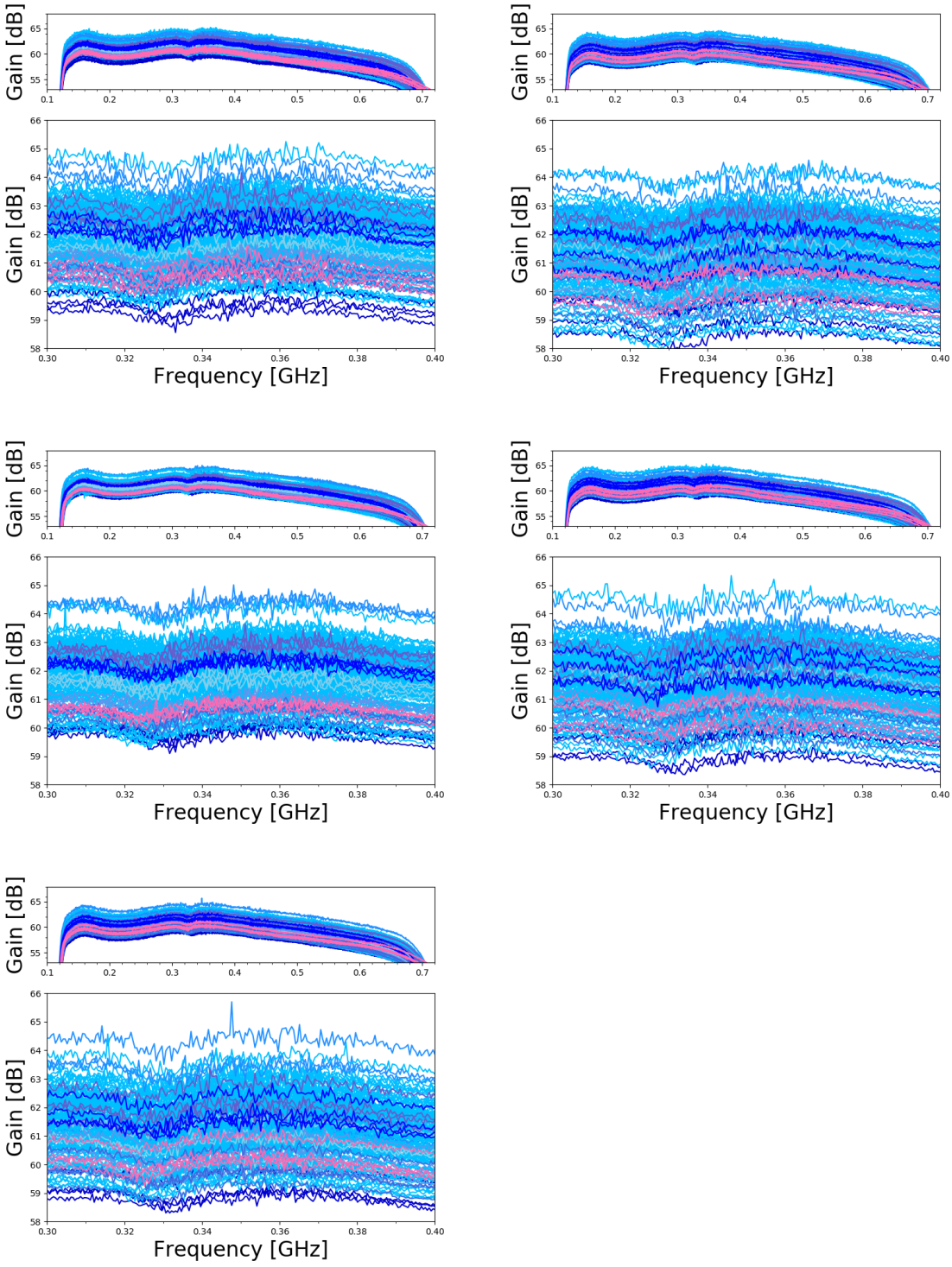

Figure 4.23: Gain of all IGLUs measured with five different DRABs [dB]. Zoom on the passband and on the range between 0.3 GHz and 0.4 GHz. The anti-resonance at 0.326 GHz is clearly visible in all measurements.

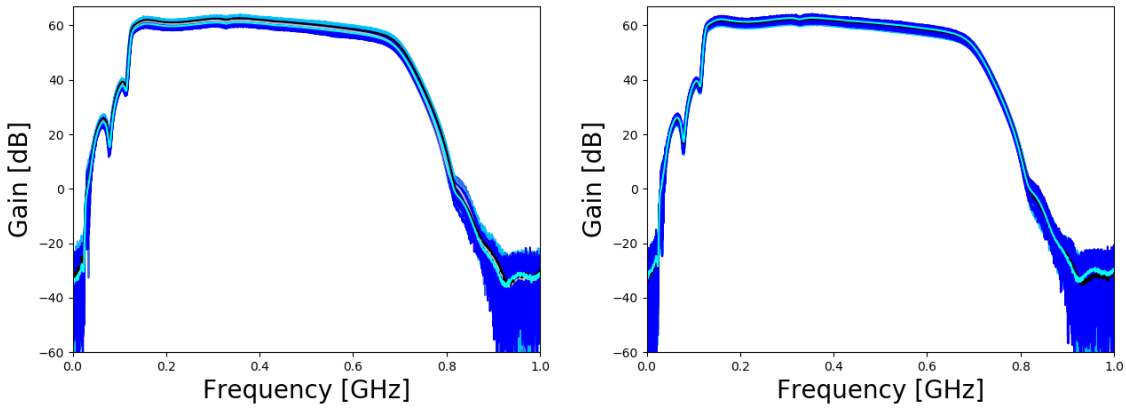

Figure 4.24: Comparison of different IGLUs. Left: All DRABS have been measured with three different IGLUs while being connected via a 3 m fiber. Right: All DRABs measured with two different IGLUs while being connected via a 50 m fiber. There are only small differences between the different measurements.

The maximum discrepancy seems to be of about 4 dB. Therefore the variation of the different IGLUs is a bit higher than of the different DRABs (see figure 4.21).

But it also has to be considered that more IGLUs (43) than DRABs (23) have been tested.

There is one IGLU board (IGLU A0004) with a higher low-pass cutoff – in pink – therefore failing to qualify for a potential use in the detector. This was the only IGLU board that showed an unwanted or unexpected behavior. The other IGLUs all showed similar results. The height of the measured gain varies with the used IGLU in a manner comparable to the influence of the DRAB.

The anti-resonance at 326 MHz is featured in all measurements. This means, that the origin of the anti-resonance was not identified during the measurements for this thesis. This feature was present in every down-hole amplifier measurement, independent of the used DRAB and the used IGLU. Therefore either the DRAB or the IGLU could cause the anti-resonance.

To further examine how much the gain depends on the used IGLU, the averages of *all* DRABs, measured with different IGLUs, were determined. All DRABs were measured several times with different IGLUs and fibers of different lengths. A comparison of different IGLUs is displayed in figure 4.24 and figure 4.25: all DRABs measured with three different IGLUs (3 m fiber) and two different IGLUs (50 m fiber). The measurements with the different IGLUs are close to each other, but not identical. The averages of the different measurements are 1.5 dB or less apart. The influence of the used IGLU therefore seems comparable to the influence of the used DRAB.

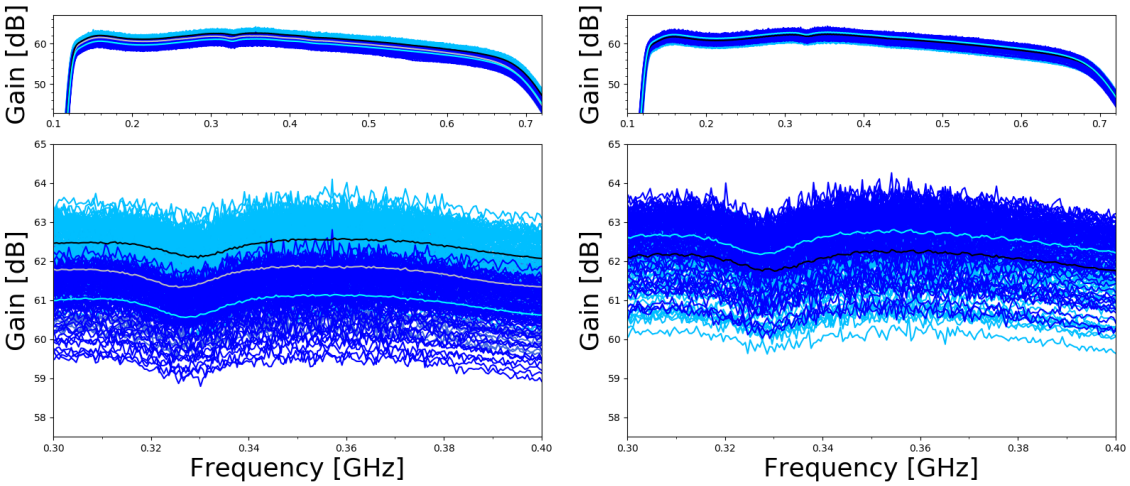

Figure 4.25: Comparison of different IGLUs. Zoom on the passband and on the range between 0.3 GHz and 0.4 GHz. Left: All DRABS have been measured with three different IGLUs while being connected via a 3 m fiber. Right: All DRABs measured with two different IGLUs while being connected via a 50 m fiber. The zoom shows that the average varies with the different measurements. The averages of all IGLUs are close, but about less than 1.5 dB (left) or less than 1 dB (right) apart. While the deviation of the DRABs is for most boards about 1 dB or less with a maximum of about 2 dB. Also clearly visible is the anti-resonance at 0.326 GHz.

4.5 Temperature Dependence

To analyze the temperature dependence of the amplifier board measurements, the S-parameters were measured at several different temperatures in a temperature chamber.

The temperature at Summit Station (72 ° 35′ 46″ N, 38 ° 25′ 19″ W) drops very low: The minimum temperature in winter is around -45 °C. The daily maximum temperature in winter is about -35 °C (January) and in summer the maximum temperature is about -10 °C (July). [94]

In section 4.2 all boards were tested in a temperature chamber to make sure they would survive the extreme cold weather in Greenland. To further investigate the influence of extreme cold temperatures and temperature changes on the amplifier board measurements, tests with the boards using the vector network analyzer were done at different temperatures in the temperature chamber.

Since amplifiers may respond very differently at various temperatures it is essential to know *how* the measurements change with the temperature, if it is *the same* for all boards and *how much* the measurements change with the temperature.

Therefore the S-Parameters of the amplifier boards were measured at different temperatures: Room temperature (about 23 °C), 0 °C, -10 °C, -20 °C, -30 °C, -40 °C and -50 °C.

4.5.1 SURFACE Boards

The SURFACE boards, when deployed, will be sitting in the DAQ box at the surface. Therefore the boards will probably not get colder than -20 °C but go through more temperature changes than the boards at 100 m depth in the borehole. The boards in the DAQ box will presumably experience temperatures in the range between about -20 °C and 20 °C.

Overall 12 channels of 4 boards, all channels of 2 boards and additional 2 single channels of 2 other boards, were measured to see how the amplifiers respond at different temperatures. The boards were put in the temperature chamber while being connected to the vector network analyzer outside the chamber.

In figure 4.26 (linear form) and figure 4.27 (logarithmic form) are the S-parameter measurements at different temperatures of one SURFACE board. Starting at a room temperature T_{room} of about 23 °C (red), over 0 °C (darker orange) in steps of ten degrees down to -50 °C (darker blue). The S-parameters change with the temperature, but they change very steadily and all measured channels behaved the same. The steady and continuous change becomes especially visible for the parameters S_{11} at higher frequencies and in the passband of the parameter S_{21}. While changes in S_{12} and S_{22} are hardly identifiable.

The gain measurement of the amplifiers is of special interest: The color gradient shows that the gain changes steadily with the temperature. The gain increases as expected at lower temperatures (see section 3.6).

While the gain of all boards was measured at room temperature, only a few channels were measured at different temperatures and therefore at the temperatures expected in Greenland. Each measurement in the temperature chamber takes a long time, so it would be very time consuming to test every board at different temperatures. Furthermore, temperatures in Greenland can of course also occur between the temperatures measured in these tests, which must also be taken into account. Additional it would be a lot of data that had to be stored to measure every board at different temperatures. This would already be very inefficient with the 12 SURFACE boards tested for this thesis. But it is definitely not a good option for the rising number of boards in the coming seasons of RNO-G and for future detector projects based on RNO-G. With an increasing number of boards the amount of work, time and additional data would become a problem.

Hence, it would be ideal if all boards would show the same behavior when being cooled down and if it would be possible to find an easy way to take temperature related changes in the measurements into account instead of measuring all boards

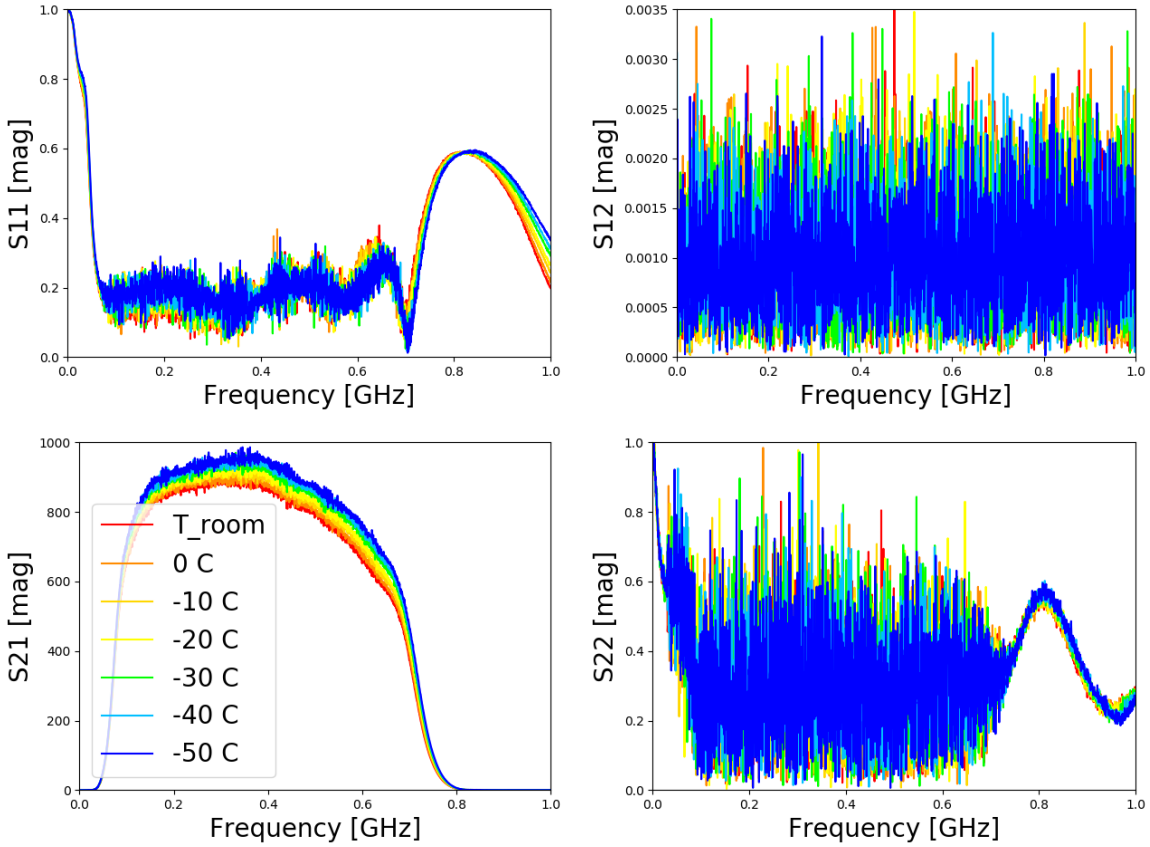

Figure 4.26: Temperature dependence of the S-parameters of a SURFACE amplifier board [mag]. The measurements change either steadily with temperature or do not change at all. The steady change becomes especially clear with the visibly developed color gradient of the parameters S_{11} (at higher frequencies) and S_{21} (passband). The gain varies inversely with temperature, the highest gain therefore was measured at -50 °C and the lowest at room temperature.

at multiple temperatures.

An idea to consider the changes in the gain while processing the data taken at different temperatures is to just multiply the gain measured at room temperature with a certain factor for different temperatures, since the gain changes very steadily with the temperature. Instead of measuring every board at multiple temperatures, the room temperature measurement, which exists for all boards, combined with different factors for different temperatures would be used to calculate the gain at the corresponding temperatures. To examine if the data at room temperature multiplied by a certain factor matches the measurements at 0 °C, -10 °C, -20 °C, -30 °C, -40 °C or -50 °C such a factor has to be determined for every temperature. For temperature $\overline{T}$ ($\overline{T}$ = 0 °C, -10 °C, -20 °C, -30 °C, -40 °C, -50 °C) the factor then

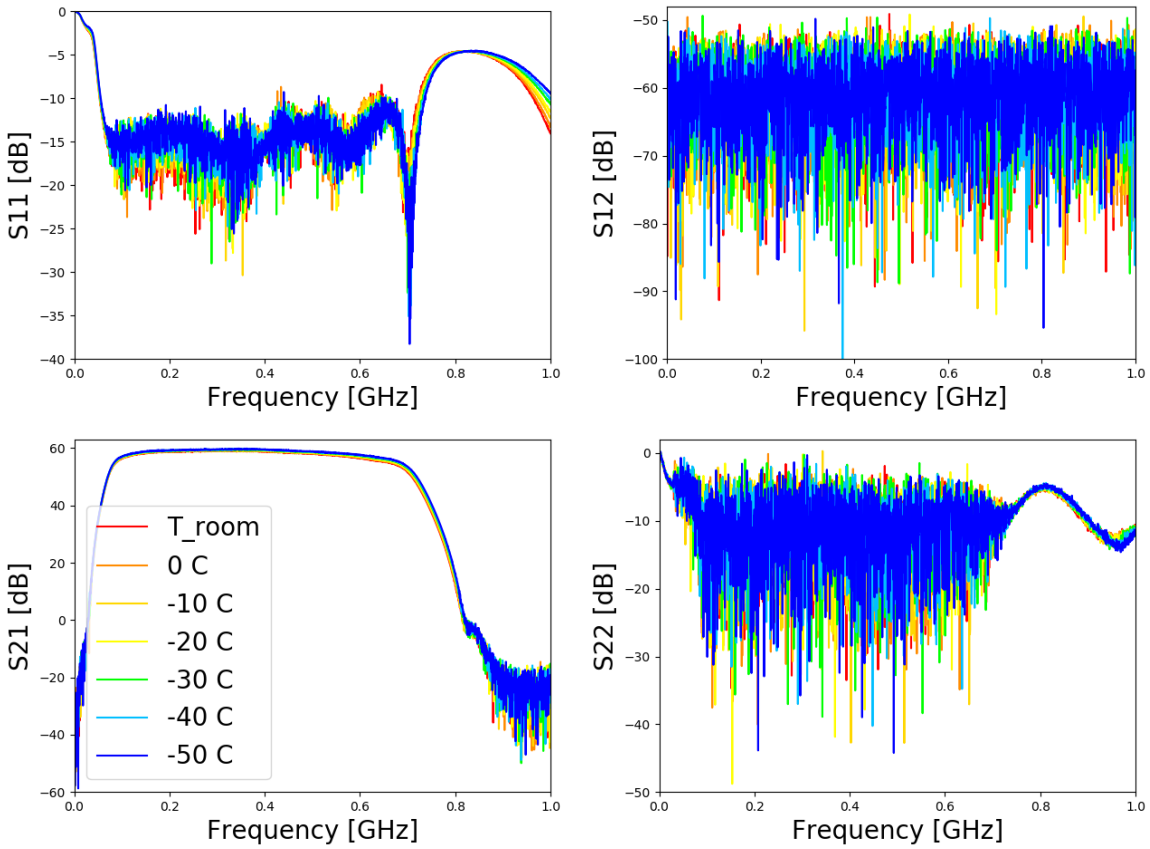

Figure 4.27: Temperature dependence of the S-parameters of a SURFACE amplifier board [dB]. The changes in the gain become larger and therefore more visible at higher frequencies in the passband.

should be the average gain at $\overline{T}$ divided by the average gain at room temperature:

$$\text{factor}(\overline{T}) = \frac{\text{average}(\overline{T})}{\text{average}(T_{room})}. \tag{4.4}$$

This was done for all measured temperatures, the results can be seen in figure 4.28 as a function of frequency. As can be seen, the factor varies for different frequencies. For higher temperatures the factor is relatively constant for frequencies between 0.1 GHz and 0.7 GHz, for the lower temperatures the difference between a factor for the lower frequencies and the higher frequencies grows. While for the 0 °C measurement the best factor at 0.1 GHz is 1.01 and for 0.7 GHz about 1.02 to 1.03, the best factor for the -50 °C measurement varies between 1.07 and 1.25 in this frequency range.

Using a *constant factor* would be the easiest way to deal with temperature changes

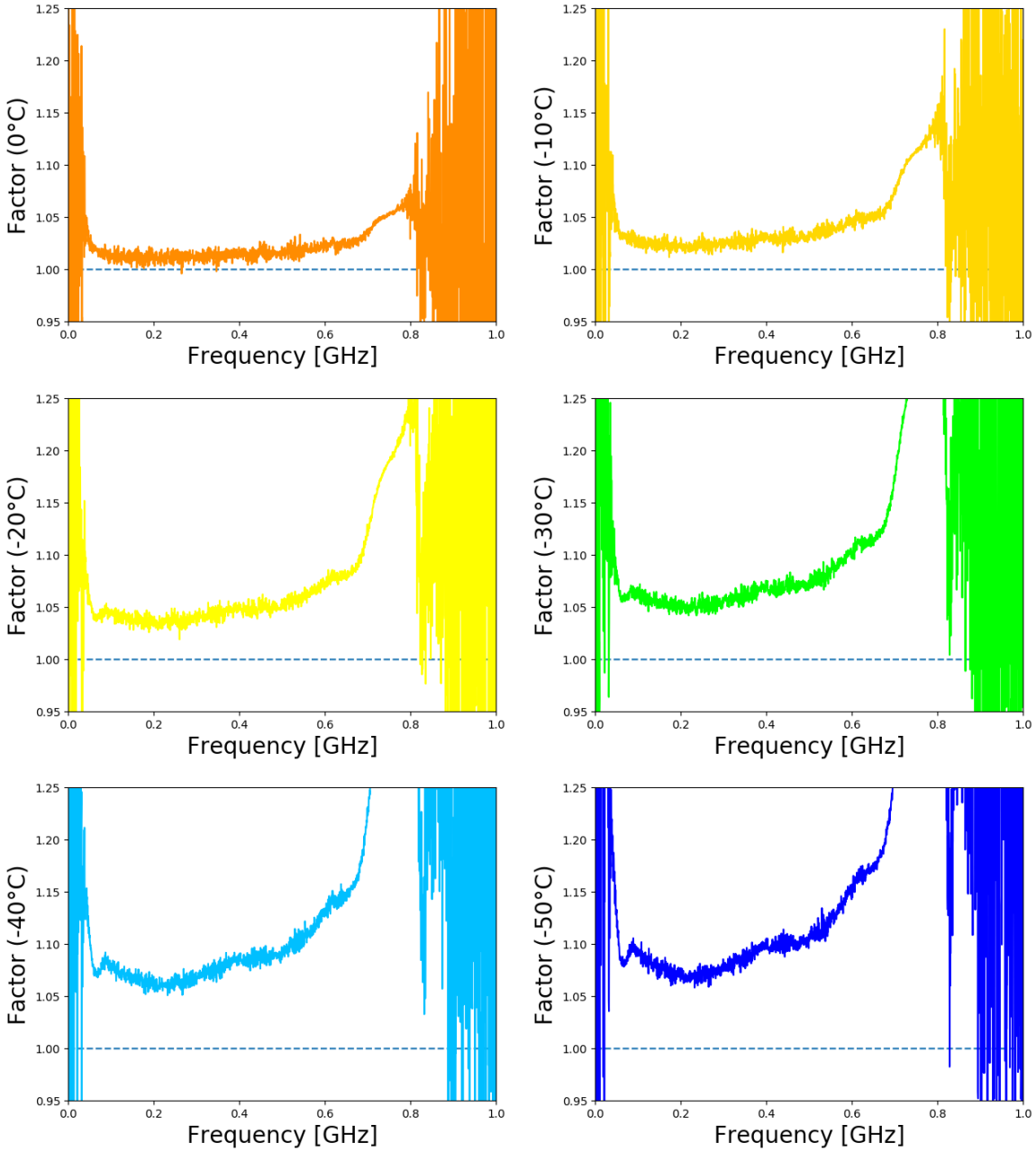

Figure 4.28: Temperature dependence: Search for a factor for the gain measurements of the SURFACE boards. Above are different factors for different temperatures as a function of frequency displayed. The data at room temperature is multiplied by a *constant factor* determined by the figures above in figure 4.29 or with the function above (*dynamic factor*) in figure 4.31 to check if this matches the measurements at different temperatures. While at higher temperatures (top row) the factor is relatively constant for frequencies between 0.1 GHz and 0.7 GHz, at lower temperatures (bottom row) the calculated factor changes more with frequency.

in the data analysis of the measurements. Despite the not so promising results of the factor determination, especially for lower temperatures, a constant factor for every temperature has been picked based on figure 4.28 and was multiplied with a gain measurement at room temperature. In figure 4.29 it was then examined how good the calculated curve matches the measured data. For higher temperatures (0 °C and -10 °C) it actually works quite well, but the difference between the measured and the estimated gain increases with decreasing temperature. For the lower temperatures both curves are clearly no longer matched at higher frequencies (between about 0.5 GHz and 0.75 GHz) but it is not a huge difference. The used factors can be found in table 4.5.

Temperature	Factor
0 °C	1.01
-10 °C	1.02
-20 °C	1.05
-30 °C	1.06
-40 °C	1.07
-50 °C	1.08

Tables 4.5: Constant factors for different temperatures. Estimated on the base of the results in figure 4.28 and used in figure 4.29.

To quantify the discrepancy between the measured gain and the gain determined with the constant factor the deviation was calculated. In this case the calculated gain $\text{gain}_{\text{calculated}}$ is computed by multiplying the room temperature measurement with the constant factor. The deviation is then determined by subtracting the measured gain from the calculated gain:

$$\text{deviation } [\%] = \frac{\text{gain}_{\text{calculated}} - \text{gain}_{\text{measured}}}{\text{gain}_{\text{measured}}}. \tag{4.5}$$

In figure 4.30 is the deviation from the actual measurements for the gain calculated by multiplying the room temperature measurement with a constant factor (see table 4.5). Shown are the gain deviations at several temperatures from the gain measurements of all 12 channels which were measured at these temperatures. In the frequency range of interest the deviation is below 5 %. But as already observed in figure 4.29, with decreasing temperature the gain deviates more at higher frequencies, starting at about 0.5 GHz and especially above 0.6 GHz. For -50 °C the deviation at 0.6 GHz is for some channels at 10 % and increases further above.

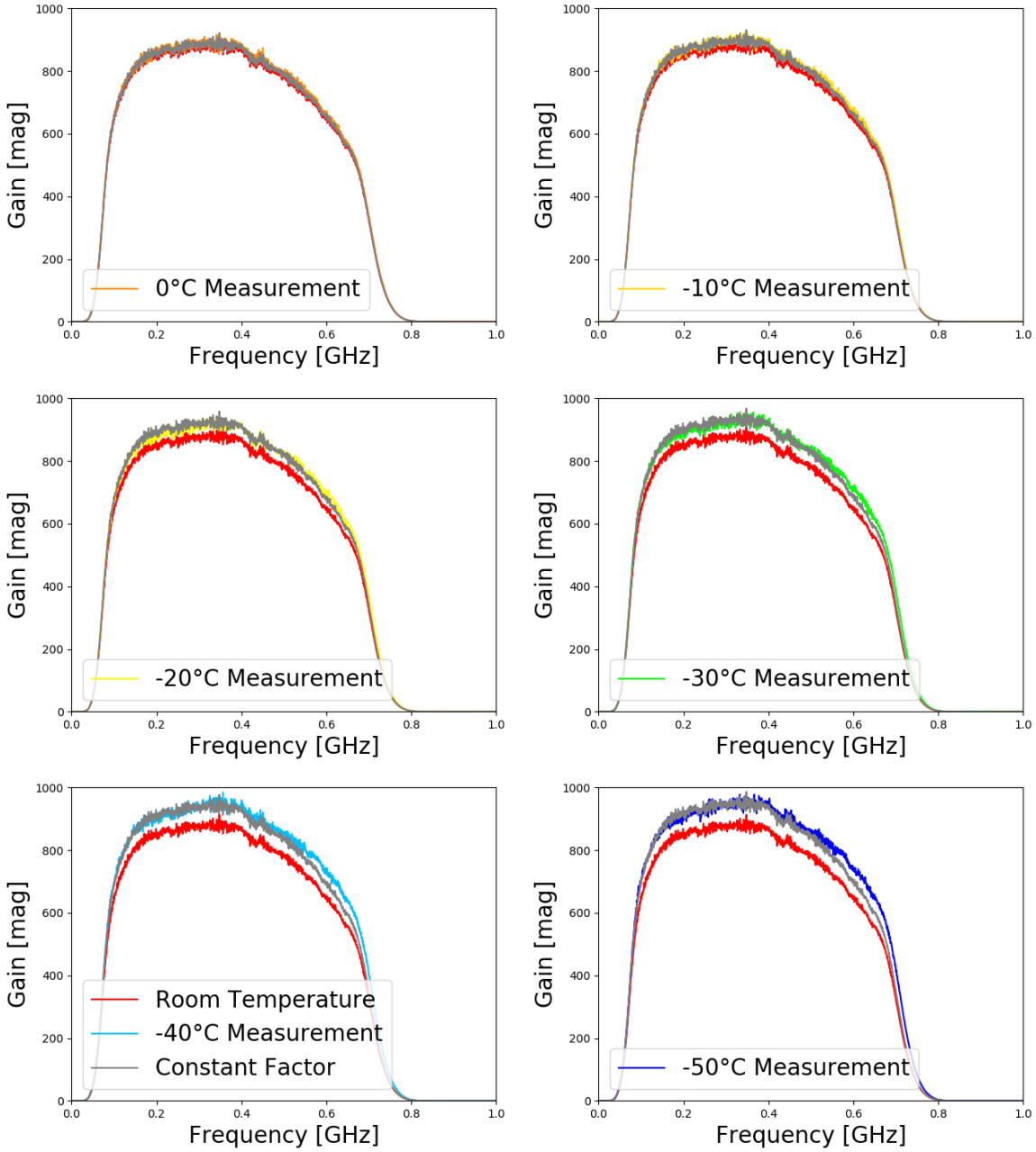

Figure 4.29: Temperature dependence: Test of the estimated constant factors of the SURFACE board measurements [mag]. The gain calculated by multiplying the room temperature measurement with a constant factor is displayed alongside the measurement at room temperature (for orientation) and the measurement at the target temperature (for comparison). This works with a constant factor quite well for higher temperatures (top row) but at lower temperatures the calculated factor changes more with frequency and therefore the calculated gain differs somewhat from the actual measurement at higher frequencies (bottom row).

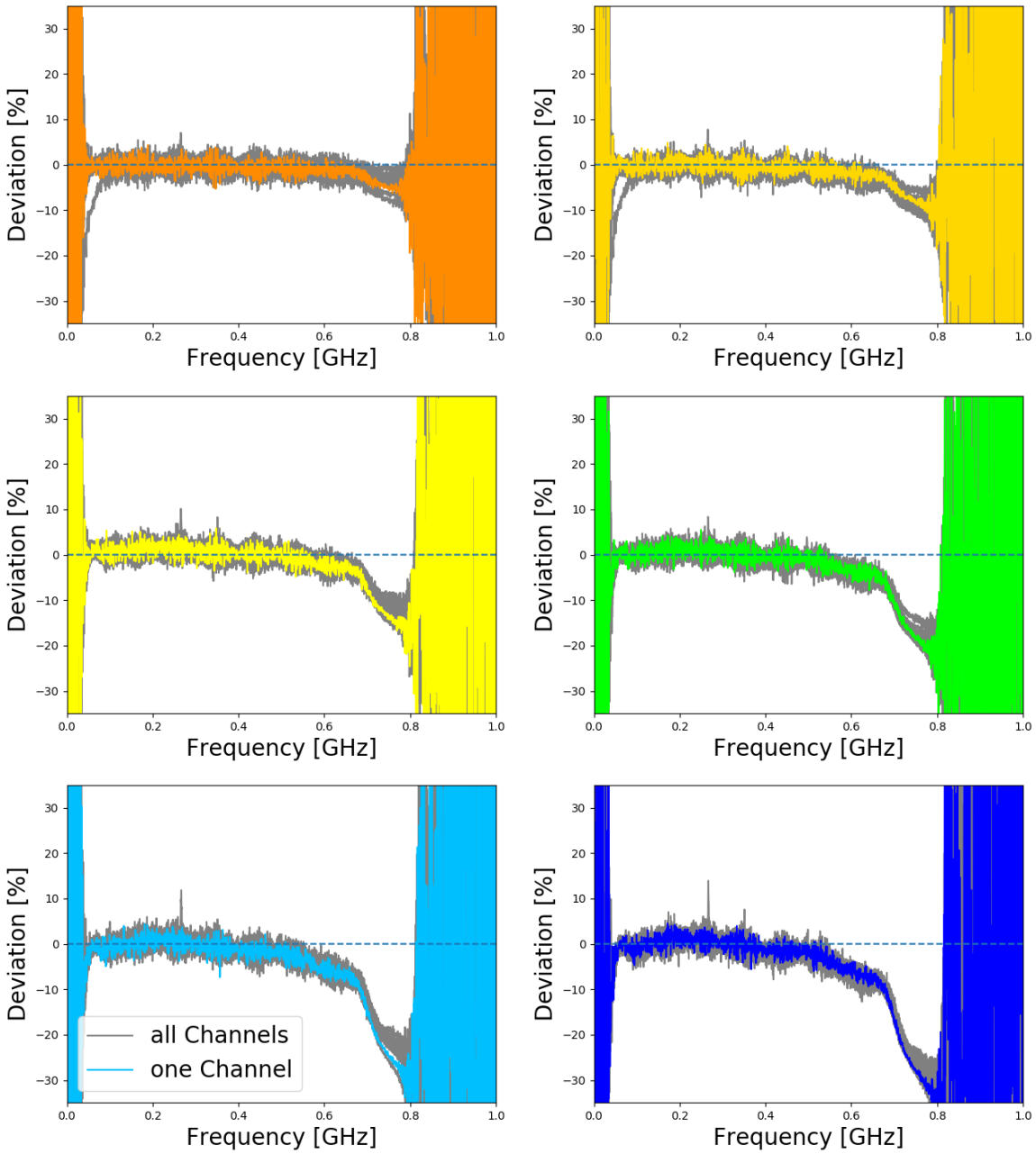

Figure 4.30: Temperature dependence: Deviation of the gain calculated with a constant factor (for all 12 measured channels). The gain calculated by multiplying the room temperature measurement with a constant factor (see table 4.5) for every temperature (0 °C (top left) to -50 °C (bottom right)) shows a deviation from the actual measurements of less than 5 % in the passband frequency range. With decreasing temperature the gain deviates more at higher frequencies, starting at about 0.5 GHz and increasing above 0.6 GHz. For -50 °C the deviation at 0.6 GHz is for some channels at 10 % and increases further above.

This shows again, that this method becomes less accurate at lower temperatures for higher frequencies.

In figure 4.31 a *dynamic factor* was used: The measured data at room temperature was multiplied with the average of all measurements at $\overline{T}$ divided by the average at room temperature as calculated with equation 4.4 and pictured in figure 4.28. This matches the actual measurements pretty good. This was the case for all measured channels and all temperatures. All channels that were measured at different temperatures were tested: The measurements were compared with the gains calculated using the dynamic factor. The precise results also indicate that all measured channels behave very similar when the temperature changes. But since the average of these measurements is used to compute the dynamic factor, the calculated gains depend on the measurements themselves. The calculated gains of other channels which have not been tested at different temperatures might therefore deviate a bit more from the real gain that would be measured at the according temperature. But since different features in the measurements still appear in the calculated gain, the differences are presumably very small. For example the small feature in the measurement between 0.4 GHz and 0.5 GHz in the displayed channel (figure 4.31) corresponds to the one in the gain calculated with the dynamic factor. This shows that small characteristic differences in the gain measurements do not cause problems using the dynamic factor method.

The deviation in percent is calculated using equation 4.5 with $\text{gain}_{\text{calculated}}$ being the gain computed by multiplying the room temperature measurement with the dynamic factor. In figure 4.32 is the deviation from the measurements at different temperatures for the gain calculated by multiplying the room temperature measurement with the dynamic factor function. Like displayed in figure 4.31 the deviation is not very large at any point, it is constantly below 5 % for all temperatures in the passband frequency range. The deviation does not increase with decreasing temperature opposed to the deviation for the constant factor method. The low deviation across the frequency range of interest proves the accuracy of the dynamic factor method. The dynamic factor works, as expected, better than a constant factor.

In regard to the increasing number of amplifier boards that are required for RNO-G and future detector projects that are based on RNO-G, the question arises whether this approach also makes sense if a large number of boards has to be tested. Since only a few boards have to be measured at different temperatures in order to determine a suitable dynamic factor, this seems to be a possibility. For future iterations on amplifier boards or completely new boards, some temperature tests would be necessary to check the temperature dependence of the gain, as happened here, anyway. These measurements can then also be used for the dynamic factor. However for an accurate dynamic factor a larger number of channels must be tested

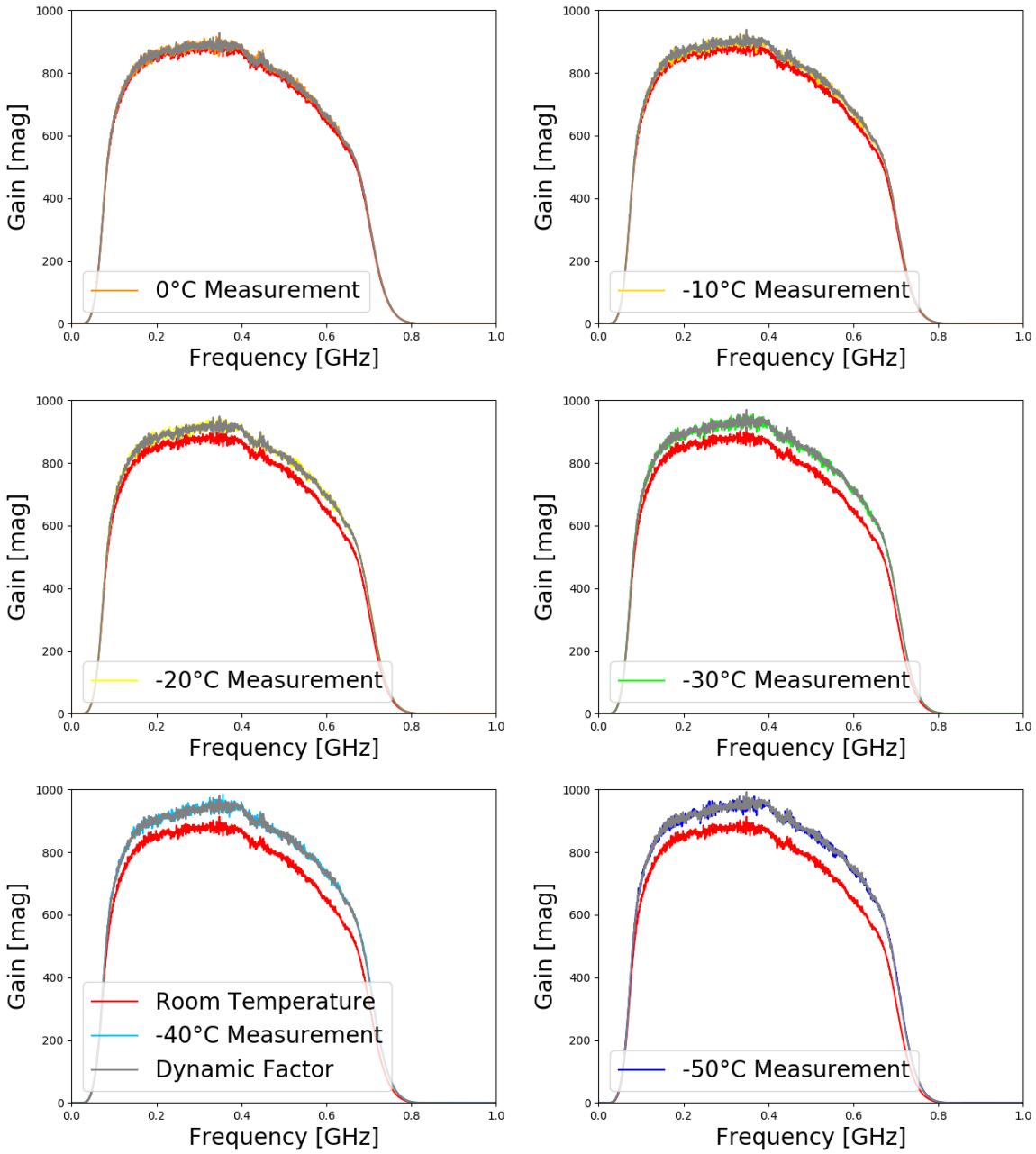

Figure 4.31: Temperature dependence: Test of the dynamic factors for different temperatures for the SURFACE board measurements [mag]. The room temperature measurement is multiplied with the dynamic factor for the target temperature. Shown are the measurements at room temperature (for orientation), the measurements at the target temperature (for comparison) and the calculated gain. This works with a dynamic factor really good for all temperatures: The measured and the calculated data are almost identical.

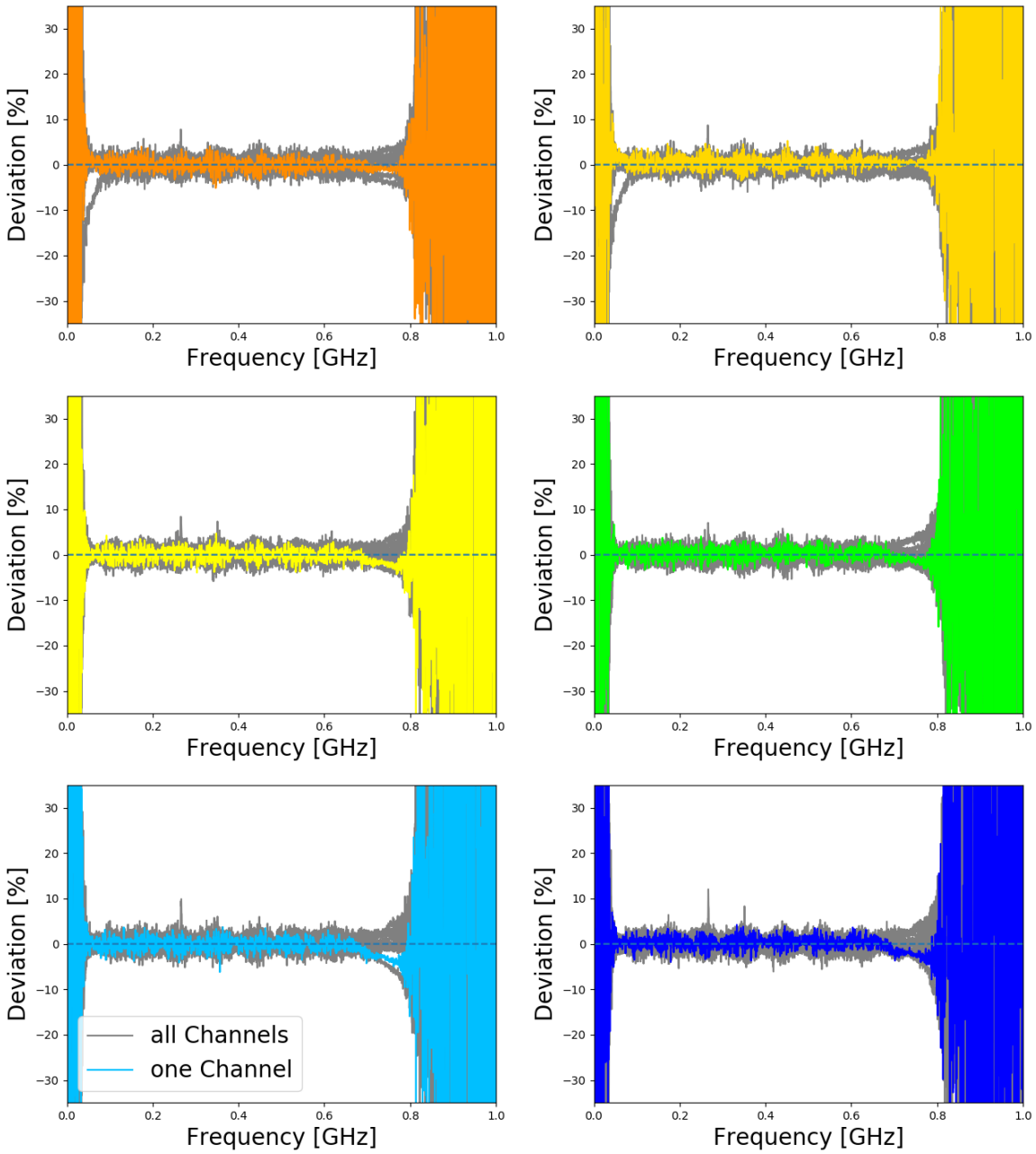

Figure 4.32: Temperature dependence: Deviation of the gain calculated with the dynamic factor, from the gain measurements of all 12 measured channels. The gain calculated by multiplying the room temperature measurement with the dynamic factor function for every temperature (0 °C (top left) to -50 °C (bottom right)) shows a deviation from the actual measurements of less than 5 % for all temperatures in the frequency range of interest. The deviation does not increase with decreasing temperature using the dynamic factor method.

and the data must be stored in such a way that it can be retrieved each time the dynamic factor is used.

Still a problem are temperatures between the ones used in these tests, which of course occur in nature. The next option to take temperature related changes in the amplifier gain measurements into account was therefore to fit the factor function calculated with equation 4.4 which can be seen in figure 4.33. The *factor function* of every measured temperature was fitted and the results (factor function multiplied by the room temperature measurement) were almost as good as the results of the dynamic factor method.

As already mentioned, the problem in practice with the corrections in relation to the temperature will be that a temperature T (at the surface) is measured and then the corresponding correction curve is needed. So the ideal result would be a function $G(T, f)$ that can be used to get the right curve for any temperature. The fit functions that were used before (see table 4.6: first fit function) follow the form $G(f) = a+b\cdot f^5$. For a steady transition between the temperatures, a fitting function for all temperatures and frequencies is needed of the type: $G(T, f) = a(T)+b(T)\cdot f^5$. In this way the parameters a and b can be determined for each temperature. In order to get $a(T)$ and $b(T)$, the parameters a and b (see table 4.6) are plotted for all measured temperatures and then fitted. The result of this straight line is the correction factor as a function of temperature. In figure 4.34 are the parameters a and b fitted with the functions:

$$\begin{aligned} a(T) &= -0.00124 \cdot T + 1.011 \\ b(T) &= -0.016 \cdot T + 0.15. \end{aligned} \tag{4.6}$$

Therefore the equation $G(T, f) = a(T) + b(T) \cdot f^5$ becomes:

$$G(T, f) = -0.00124 \cdot T + (-0.016 \cdot T + 0.15) \cdot f^5 + 1.011. \tag{4.7}$$

Temperature	First Fit Function	New Fit Function
0 °C	$1.011 + 0.15 \cdot f^5$	$1.011 + 0.15 \cdot f^5$
-10 °C	$1.022 + 0.3 \cdot f^5$	$1.023 + 0.31 \cdot f^5$
-20 °C	$1.036 + 0.5 \cdot f^5$	$1.036 + 0.47 \cdot f^5$
-30 °C	$1.053 + 0.6 \cdot f^5$	$1.048 + 0.63 \cdot f^5$
-40 °C	$1.07 + 0.8 \cdot f^5$	$1.061 + 0.79 \cdot f^5$
-50 °C	$1.073 + 0.95 \cdot f^5$	$1.073 + 0.95 \cdot f^5$

Tables 4.6: Fit functions for different temperatures depending on the frequency f [GHz]. The new parameters $a(T)$ and $b(T)$ of the new fit function differ only slightly from the parameters of the first fit function.

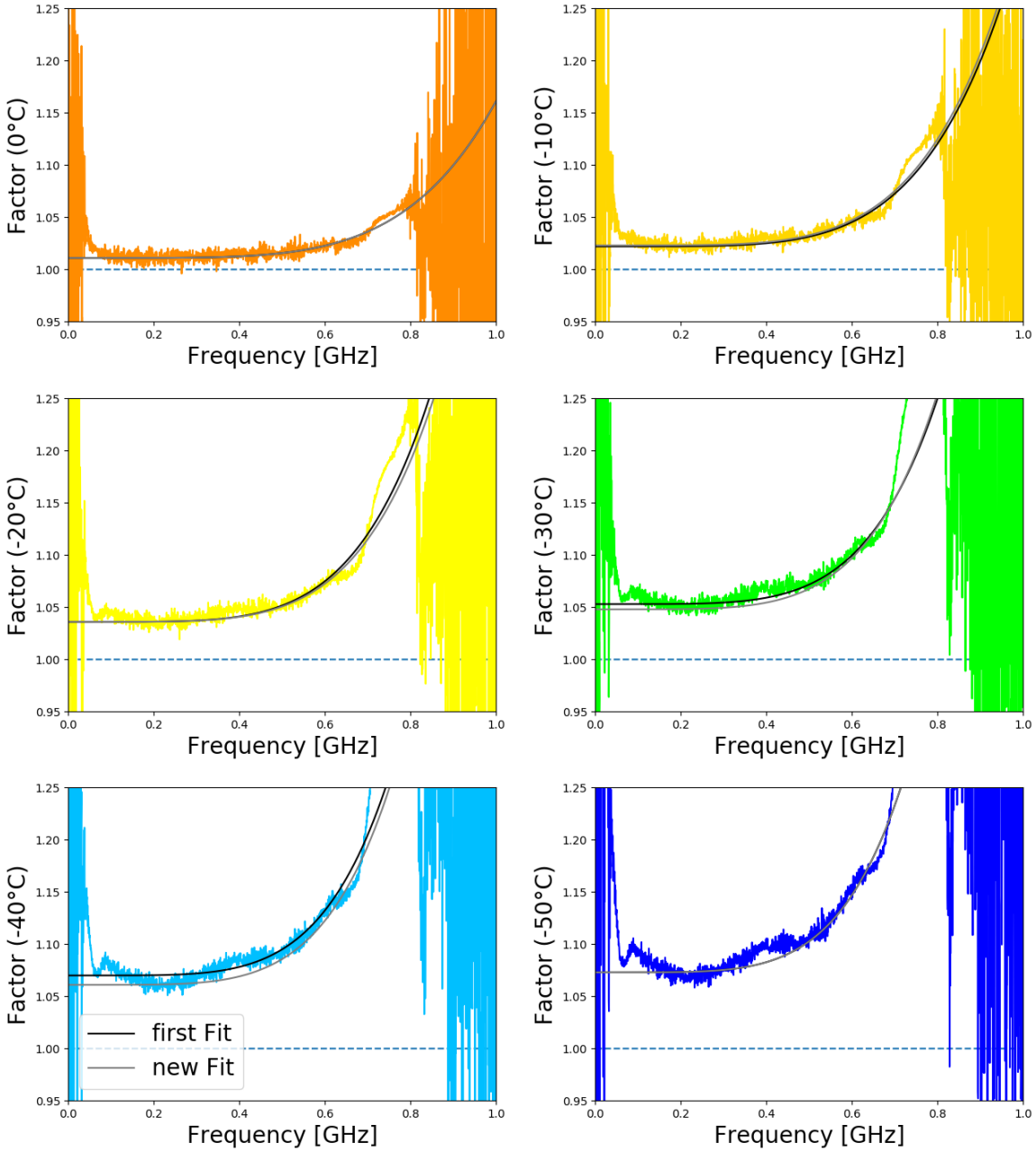

Figure 4.33: Temperature dependence: Fits of the factor function for the gain measurements of the SURFACE boards. Above are two different fits (see table 4.6) for different factors for several temperatures as a function of frequency displayed. While at higher temperatures (top row) the factor function is relatively even and constant for all frequencies, at lower temperatures (bottom row) the function is uneven and therefore the fits do not work as well. The two fit functions differ only slightly from each other. While the *first fit* works a bit better as an approximation to the function, the *new fit* allows to calculate the gain at any temperature and enables a steady transition between the temperatures.

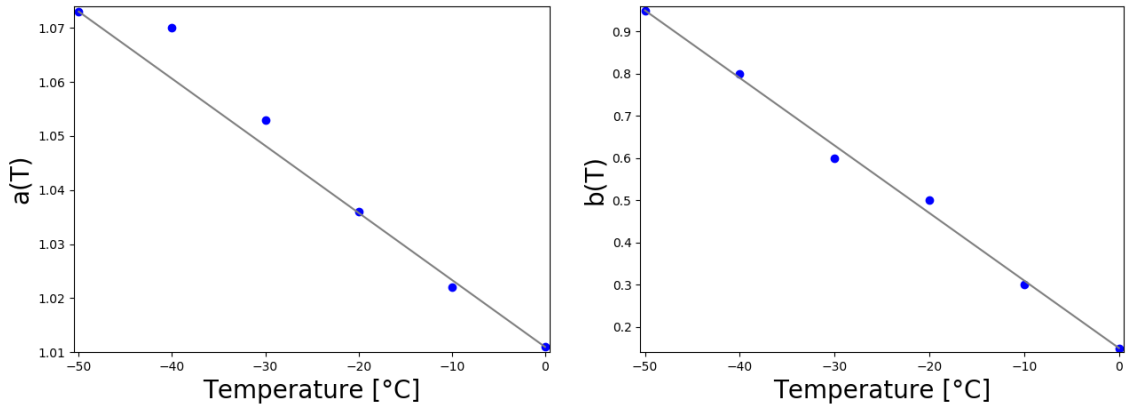

Figure 4.34: The fits to the parameters (blue dots) $a(\overline{T})$ (left) and $b(\overline{T})$ (right) for $\overline{T}$ = 0 °C, -10 °C, -20 °C, -30 °C, -40 °C, -50 °C are displayed in the figures. The previously determined, very well working parameters deviate in some cases ($a(T)$ for -30 °C and -40 °C) from the fit. The new fit parameters are therefore not expected to be as good as the individual determined parameters, but the deviations are supposedly only minimal. The advantage of the new parameters is instead, that it is possible with this method to calculate the curve for a measurement at a temperature between the measured intervals.

The new *fit functions* can be found in table 4.6 (new fit function). In figure 4.35 the gain measurement at room temperature was then multiplied with both fit functions for the targeted temperature. The results look very good, comparable to the gains calculated with the dynamic factor. The differences between both fits are very small. But due to the uneven factor function there are more small deviations from the measurements especially in the figures for the lower temperatures. These are only identifiable when zooming into the figures. This was the case for all measured channels and all temperatures.

The actual deviation is calculated using equation 4.5 with $\text{gain}_{\text{calculated}}$ being the gain computed by multiplying the fit function with the room temperature measurement. Figure 4.36 shows the deviation from the measurements at different temperatures. This was done for both fit functions (see table 4.6), the results barely differ. The deviation is below 5 % for all temperatures up to 0.7 GHz for both cases. Below 0.7 GHz the fit function method shows the same results as the dynamic factor method. But above 0.7 GHz the deviation increases with decreasing temperature and the behavior is therefore similar to the constant factor method. But since this frequency range with the higher deviation is no longer interesting for the measurements anyway, the increase in deviation is not a problem.

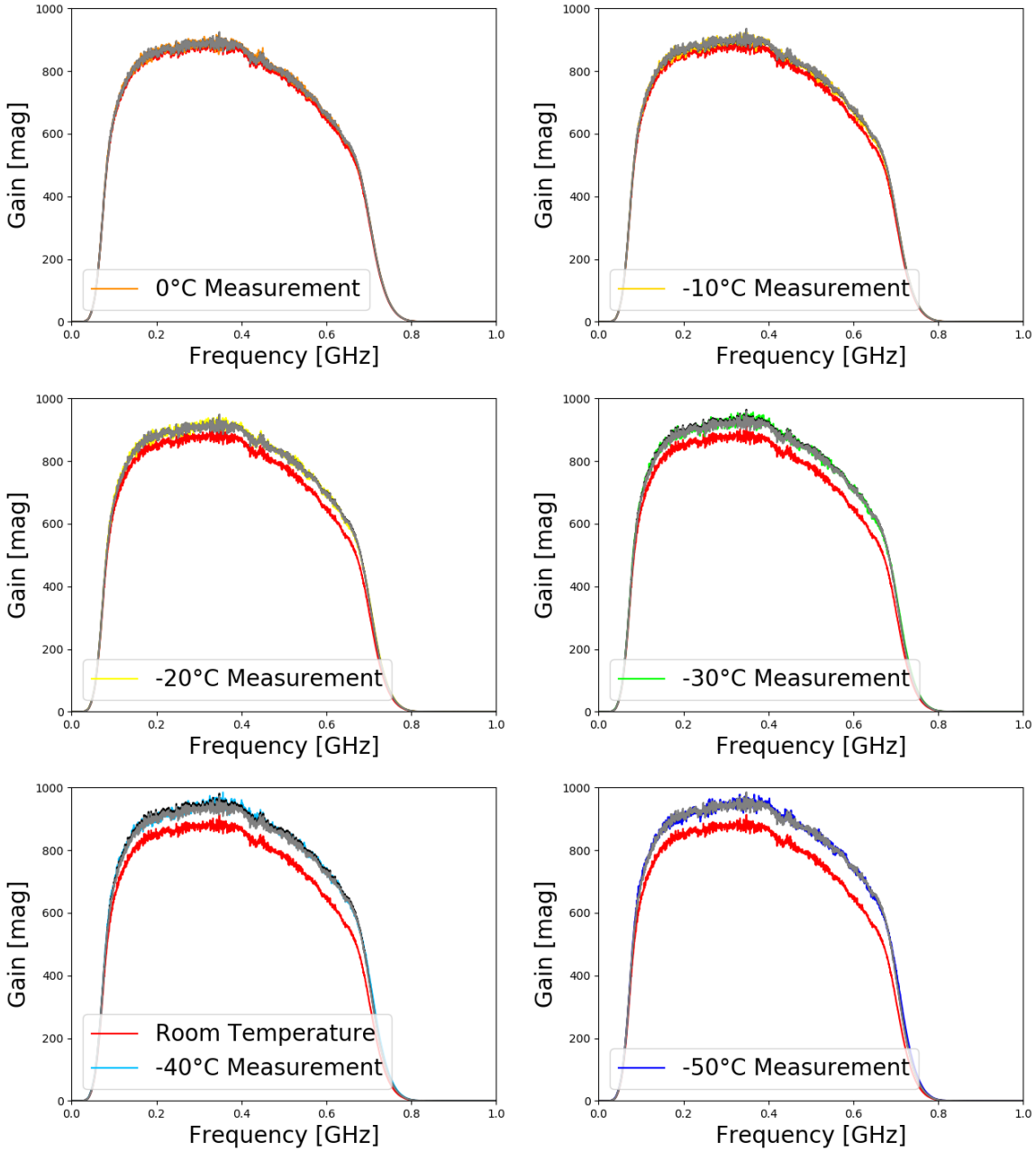

Figure 4.35: Temperature dependence: Test of the fit functions for different temperatures for the SURFACE board measurements [mag]. The room temperature measurement is multiplied with the fit function for the target temperature. The fit function method works quite well, only when zooming into the lower temperature figures some mismatches become visible. There are only small differences between the two used fits, the clearest deviation is in the -40 °C figure (bottom left) between 0.3 GHz and 0.5 GHz. Small features and the gain for frequencies above 0.7 GHz are not perfectly fitted in both cases. Since the gain above 0.7 GHz is of minor interest and the differences are small, this method seems like a good option.

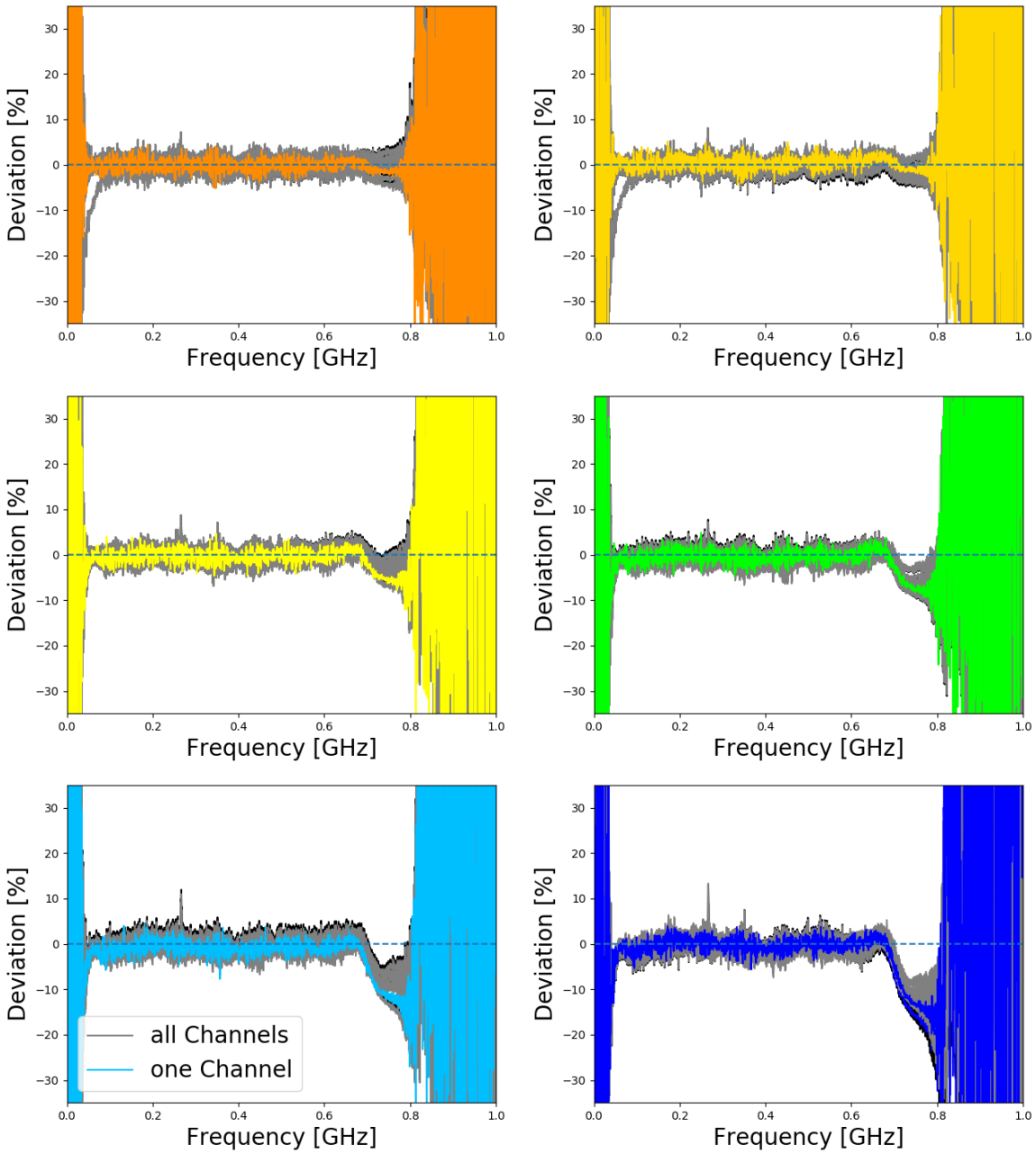

Figure 4.36: Temperature dependence: Deviation of the gain calculated with both fit functions, from the gain measurements of all 12 measured SURFACE board channels. The gain calculated by multiplying the room temperature measurement with both fit functions (see table 4.6) for every measured temperature shows a deviation from the actual measurements of about 5 % for all temperatures up to 0.7 GHz. Above 0.7 GHz the deviation increases with decreasing temperature. There are almost no differences between the used fit functions visible, the deviation is one percentage point (-40 °C figure) or lower.

The low deviation for most frequencies is comparable to the excellent results of the dynamic factor method. The fit function method seems like a good option to consider the temperature changes of the amplifiers, although the dynamic factor method works a bit more precise. The ability of the fit function method to calculate the gain for each temperature is a major advantage of this method.

It must be taken into account that the gain is represented in linear form so that even small deviations can be recognized. The differences between the gain measurements at different temperatures and the mismatch at lower temperatures for the constant factor are not huge, as the deviation figures have shown.

For quantification, the deviations within the passband for different temperatures are shown in histograms (see figure 4.37 and figure 4.38). The 68 % quantile (see table 4.7) was then determined for each temperature, so all three methods can be compared by this number. For the reconstruction it is important how many individual values deviate significantly. The histograms show how the average is formed and how much the deviations spread. There is an entry in the histogram for each measured frequency. The results of the dynamic factor method and of the fit function method are very similar, the deviation distribution does not change much at different temperatures, almost all frequencies show a deviation below 4 % for all frequencies. For the fit method only at lower temperatures (-30 °C and lower) more frequencies show a slightly higher deviation (between 2 % and 3 % instead of 1 % and 2 %). The constant factor method shows frequencies with the highest deviation, increasing with decreasing temperature, up to 18 % for a few frequencies at -50 °C.

Temperature	Constant Factor	Dynamic Factor	Fit Function
0 °C	1.58 %	1.30 %	1.36 %
-10 °C	2.05 %	1.26 %	1.36 %
-20 °C	2.08 %	1.32 %	1.45 %
-30 °C	2.45 %	1.29 %	1.55 %
-40 °C	2.99 %	1.33 %	1.65 %
-50 °C	3.29 %	1.34 %	1.62 %

Tables 4.7: The 68 % quantile of the deviation over the whole passband (80 MHz-700 MHz) for all three methods at all temperatures for the SURFACE boards.

The 68 % quantile (dashed line in the histograms) is one single number that describes the deviation at which 68% of the measured values are on the left in the histogram. This number is a good quantifier for the quality of the deviation and all methods can be compared on one value.

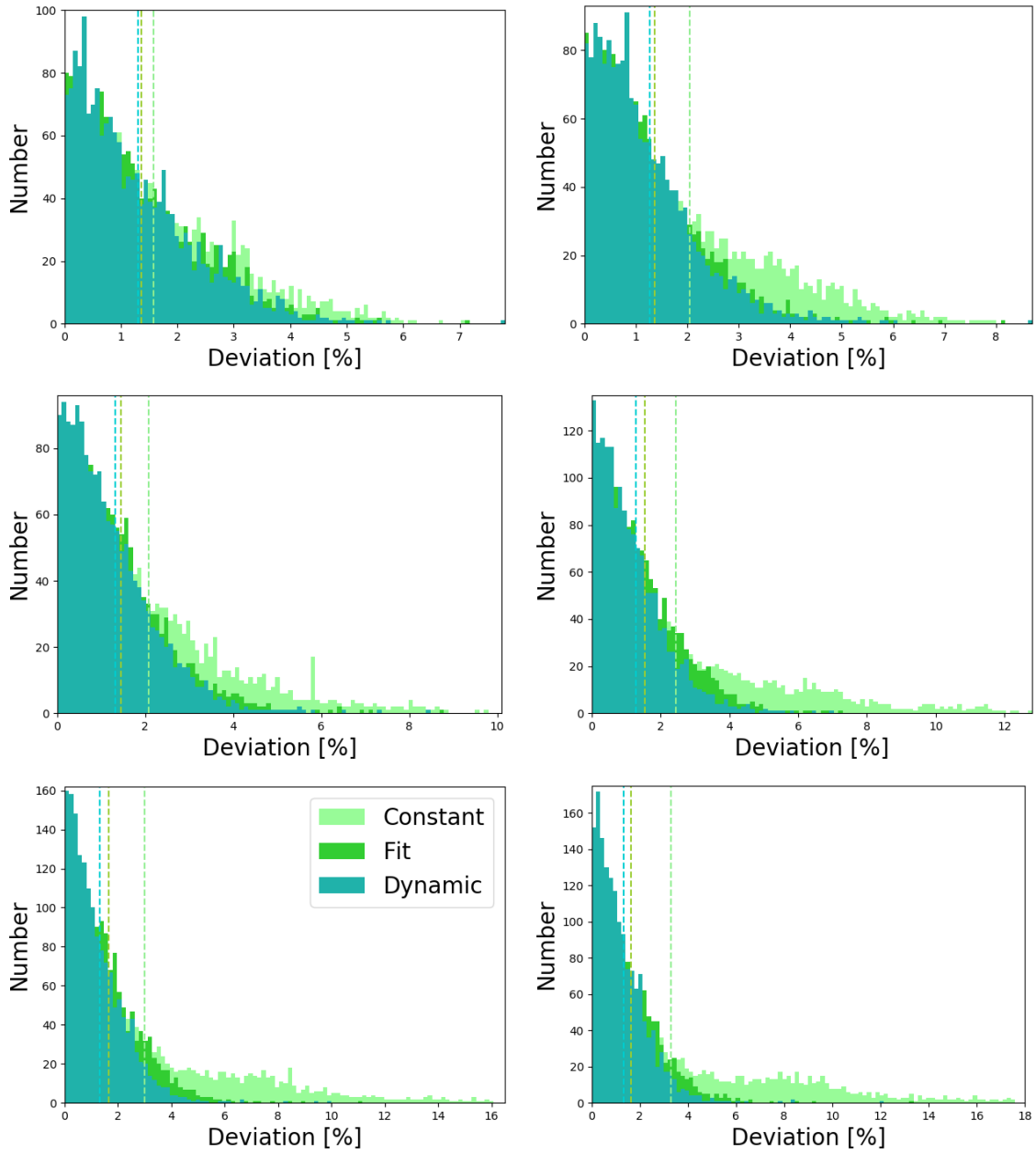

Figure 4.37: Histograms to compare the accuracy of the constant, the dynamic and the fit method at different temperatures (0 °C to -50 °C). The figures show the number of frequencies with a certain deviation in the passband for all 12 measured SURFACE board channels. The dashed lines mark the 68 % quantile of the corresponding method. While the 68 % quantile belonging to the dynamic factor and to the fit function method do not move much with decreasing temperature (staying below 1.7 %), the dashed line corresponding to the constant factor method moves up to 3.3 % at lower temperatures.

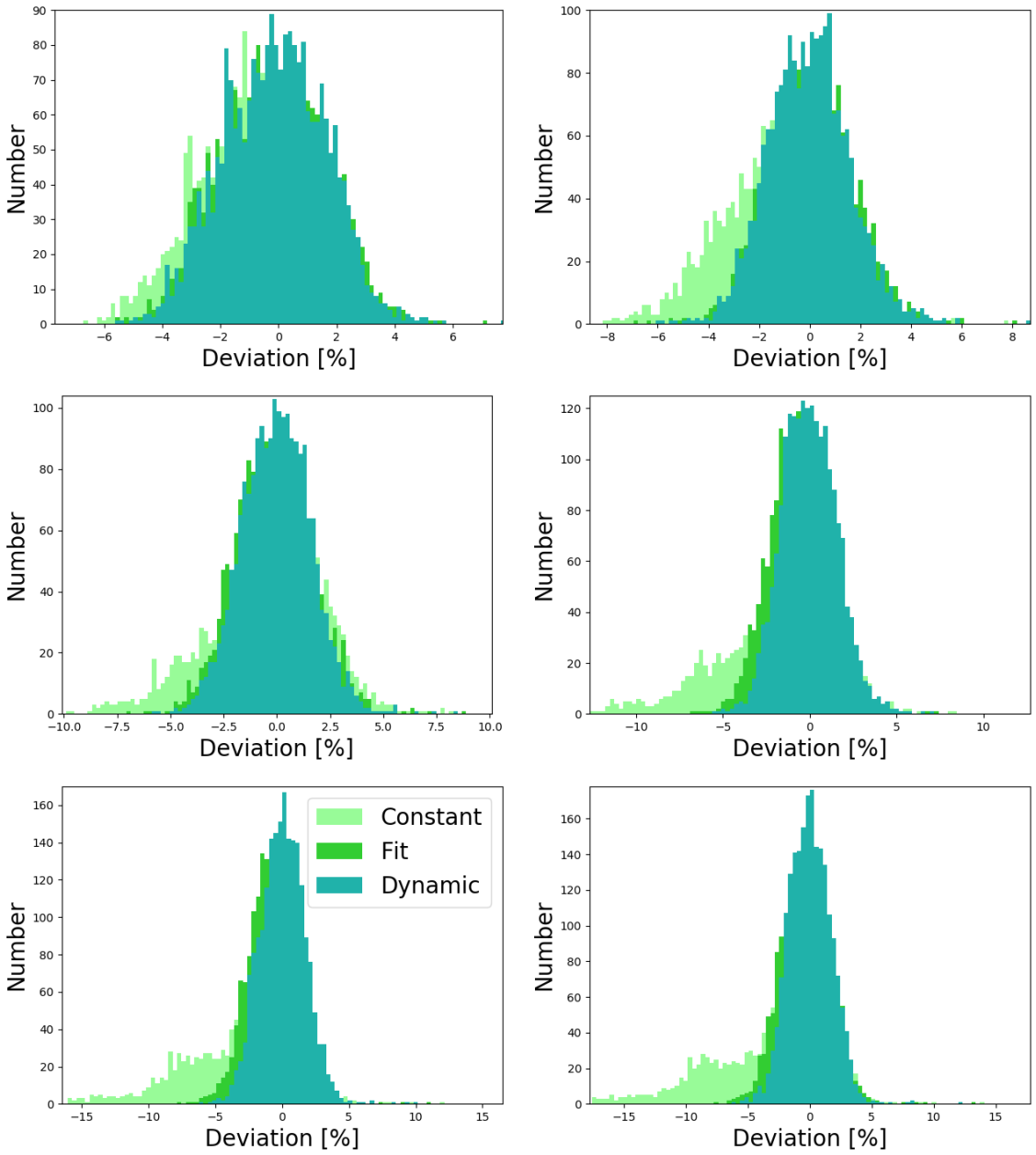

Figure 4.38: Histograms to compare the constant, the dynamic and the fit method for the SURFACE boards. The figures show the distribution of the deviations upwards and downwards. The deviation distribution is relatively symmetrical for the dynamic and the fit method in the analyzed frequency range. Only the constant method is distributed asymmetrical with significantly greater downward deviations. This could already be seen in figure 4.30. The upwards deviation is comparable for all three methods.

For the constant factor method the deviation for 68 % of the measured frequencies is between 1.58 % or lower at 0 °C and 3.29 % or lower at -50 °C, as can be seen in table 4.7. For the dynamic method and for the fit method, the 68 % quantile is between 1.26 % and 1.34 % (1.36 % and 1.65 %) for different temperatures. The deviation increases for the fit function method and especially for the constant factor method with decreasing temperature. For the dynamic factor and for the fit function method 68 % of all frequencies only show a deviation below 2 % (between 1.26 % and 1.65 %). At the end of the passband with decreasing temperature the deviation increases for the fit function method (from 5.60 % to 7.41 %) and especially for the constant factor method (from 6.65 % to 18.45 %). While the deviation for the dynamic factor function varies between 5.49 % and 6.21 %. The maximum deviation values for every temperature can be found in table 4.8.

Temperature	Constant Factor	Dynamic Factor	Fit Function
0 °C	6.65 %	5.55 %	5.60 %
-10 °C	8.10 %	6.01 %	6.92 %
-20 °C	9.70 %	5.86 %	6.87 %
-30 °C	12.91 %	5.49 %	6.69 %
-40 °C	16.65 %	6.21 %	7.74 %
-50 °C	18.45 %	6.11 %	7.41 %

Tables 4.8: Maximum deviation for the SURFACE boards in the passband at different temperatures for all three methods. The deviations can also be seen in figure 4.30, figure 4.32 and figure 4.36 for the different methods. Only some extreme outliers such as the one at 265 MHz (featured in all figures) were excluded.

The constant factor works for an estimation but for an optimal data analysis of RNO-G a more precise method for considering the temperature changes of the amplifiers is needed. The dynamic factor method proved itself to work very well (see table 4.7). Since the SURFACE boards react uniformly and therefore predictable to temperature changes, this method is a precise alternative to measuring all boards at multiple temperatures. The fit function method has the advantage that the data for the factor function has not to be used directly when doing data analysis, opposed to the dynamic factor method. This method is not as accurate as the dynamic factor, but most importantly: The fit function method can be used to calculate the gain at any temperature, while the constant factor and the dynamic factor method only work for the few temperatures that a few channels have actually been measured at. A correction function can be determined and used for any temperature with a continuous transition between different temperatures. The fit

function methods makes it possible to calculate the gain of every board at any temperature with just the room temperature measurement given. The method proved itself to work very well.

4.5.2 DRABs and IGLU Boards

The tests with the DRABs and IGLU boards studied the influence of the temperature of different components (DRAB, IGLU and fiber cable) on the measurements.

The temperature dependence of the down-hole amplifier chain is more complex than the SURFACE board temperature dependence. The DRABs that will be deployed in Greenland will be sitting in the DAQ box at the surface like the SURFACE boards. Therefore it is unlikely that the boards will experience temperatures colder than -20 °C, but the DRABs go through more temperature changes than the IGLU boards at 100 m depth in the borehole. While the boards in the DAQ box are suspected to experience temperatures in the range between about -20 °C and 20 °C, the IGLUs will experience a colder, but mostly static temperature between about -40 °C and -30 °C. The fiber that connects the DRAB and the IGLU board will hence experience different temperatures at different sections.

It is complex to consider the different temperatures and the temperature variations of the IGLU board, the DRAB and the fiber. To study the influence of extreme low temperatures on the different components of the down-hole chain different combinations of the cooled down components and components at room temperature were tested. One of the boards (IGLU board or DRAB) was placed inside the temperature chamber and was cooled down while the other board stayed outside at room temperature. The fiber connecting the two boards was either mostly inside or outside the chamber. Analogous to the SURFACE board measurements, the S-parameters of the DRAB and IGLU boards were measured. For an even more realistic study two temperature chamber next to each other would be needed to keep the IGLU at a low temperature while the DRAB is measured at different temperatures.

In figure 4.39 are the S-parameters of a DRAB and an IGLU board measured at multiple temperatures in linear form and figure 4.40 shows the same data in logarithmic form. In this case the temperature dependence of the S-parameters was studied when all components (DRAB, IGLU and fiber cable) were inside the temperature chamber. The parameters S_{11}, S_{12} and S_{22} behave in a similar way to the parameters of the SURFACE boards, changing steadily with the temperature. Only the gain behaves differently and does not increase continuously with decreasing temperature.

To determine the temperature dependence of the boards and to estimate how the gain measurements in Greenland will be influenced by the temperature, different combinations of the DRAB, the IGLU and the fiber inside and outside of the

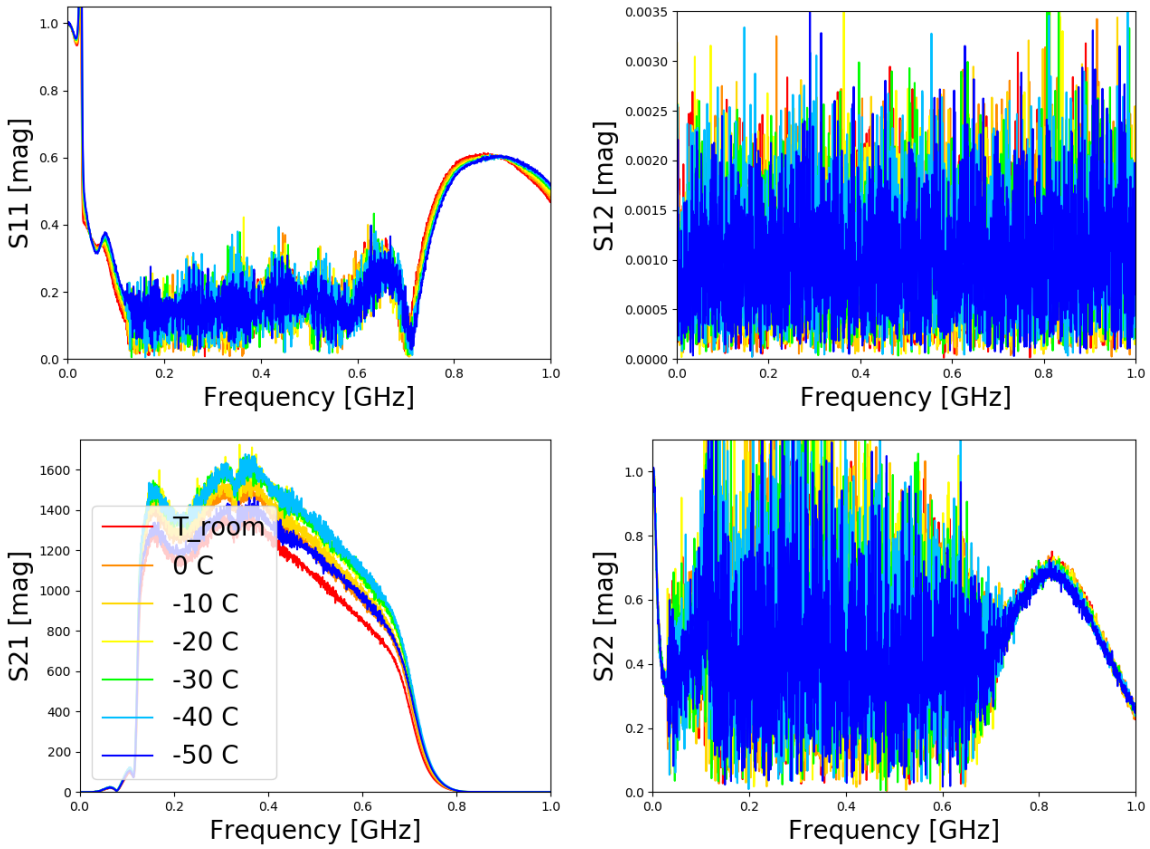

Figure 4.39: Temperature dependence of the S-parameters of a DRAB and an IGLU board [mag]. DRAB, IGLU and fiber cable were inside the temperature chamber and the S-parameters were measured at different temperatures. While the changes in S_{11}, S_{12} and S_{22} are similar to the behavior of the SURFACE board at different temperatures, S_{21} changes differently.

temperature chamber were tested. In (almost) all cases shown in the following the same two channels of two different DRABs (DRAB A0003 channel 1 and DRAB A0012 channel 1) were tested with the same IGLU for good comparison. In some cases more channels have been tested and can be found in the appendix (figure 6.26 - 6.29).

First, the influence of the DRAB temperature was tested, followed by the influence of the fiber temperature (see figure 4.41). With the DRAB inside the temperature chamber and the IGLU board and the fiber outside the gain measurements only slightly change with temperature. The temperature changes of the DRAB do not influence the gain measurement very much. Between about 450 MHz and 700 MHz the measurements at different temperatures slightly vary, similar to the

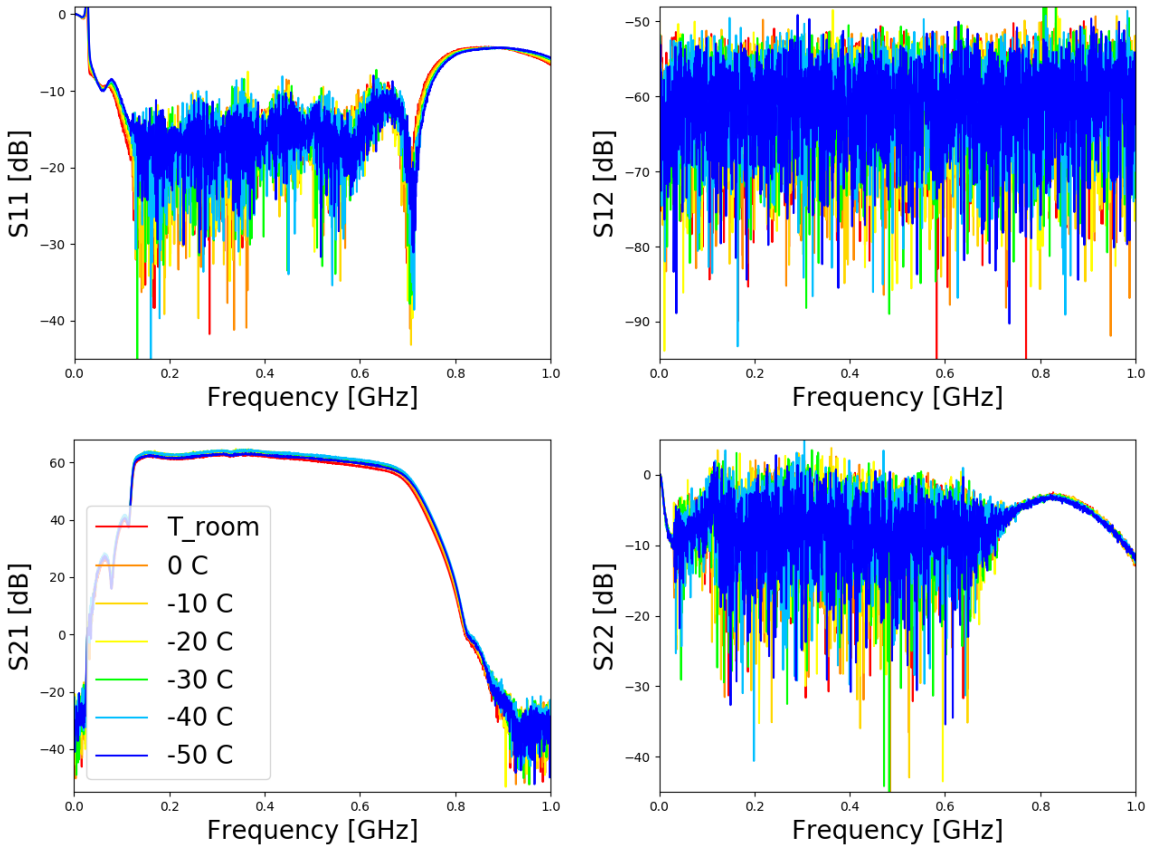

Figure 4.40: Temperature dependence of the S-Parameters of a DRAB and an IGLU board [dB]. The measurements in logarithmic form show, that the changes due to the temperature variation are relatively small.

SURFACE board gain at different temperatures: With decreasing temperature the gain increases. The gain does not appear to have a strong dependence on the DRAB temperature. Putting the fiber inside the chamber as well does not really change the measurements either. With the DRAB and the fiber getting cooled down while the IGLU stays outside the temperature chamber, the gain measurement looks similar to the case with just the DRAB inside the chamber. Hence, the fiber temperature does not influence the gain very much either.

Next, the influence of the IGLU temperature on the measured gain was tested (see figure 4.42). First, the IGLU was put inside the temperature chamber and after that the IGLU and the fiber were placed inside the chamber and only the DRAB stayed outside. The temperature of the IGLU seems to influence the measured data clearly more than the DRAB temperature. The different gain measurements have different heights and opposed to the SURFACE board measurements the

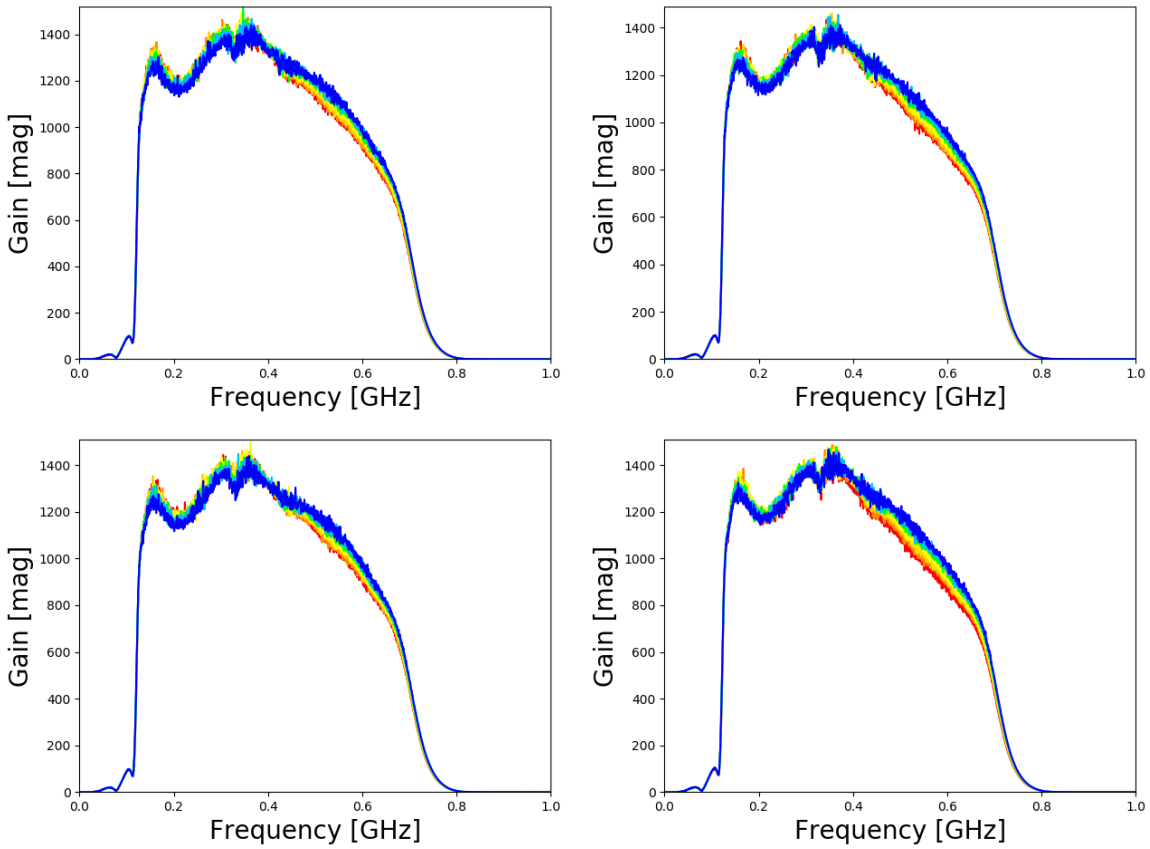

Figure 4.41: DRAB or DRAB and fiber cooled down. Top row: While the DRAB was in the temperature chamber, the IGLU board and the fiber were outside. Bottom row: DRAB and fiber were in the temperature chamber while the IGLU stayed outside. The same two different DRAB channels have been tested in both cases (left and right). The temperature changes of the DRAB do not influence the gain measurement very much. Putting the fiber inside the chamber additionally does not really change the measurements either: The measurements in the bottom row fit there counterpart in the top row quite well. Only the measurements in the bottom right figure spread a bit more, but the difference is insignificant.

measurements change not steadily with the temperature. In the case of the SURFACE boards the gain increased with decreasing temperature.

But the gain of the DRABs only varies inversely with temperature until around -30 °C or -40 °C. After that the gain starts to decrease again. The gain measured at -50 °C (and in some cases at -40 °C) is only slightly larger than the gain measured at room temperature. Additional the difference between the gain measurement at room temperature and the measurement at 0 °C is greater than the differences between the other measurements.

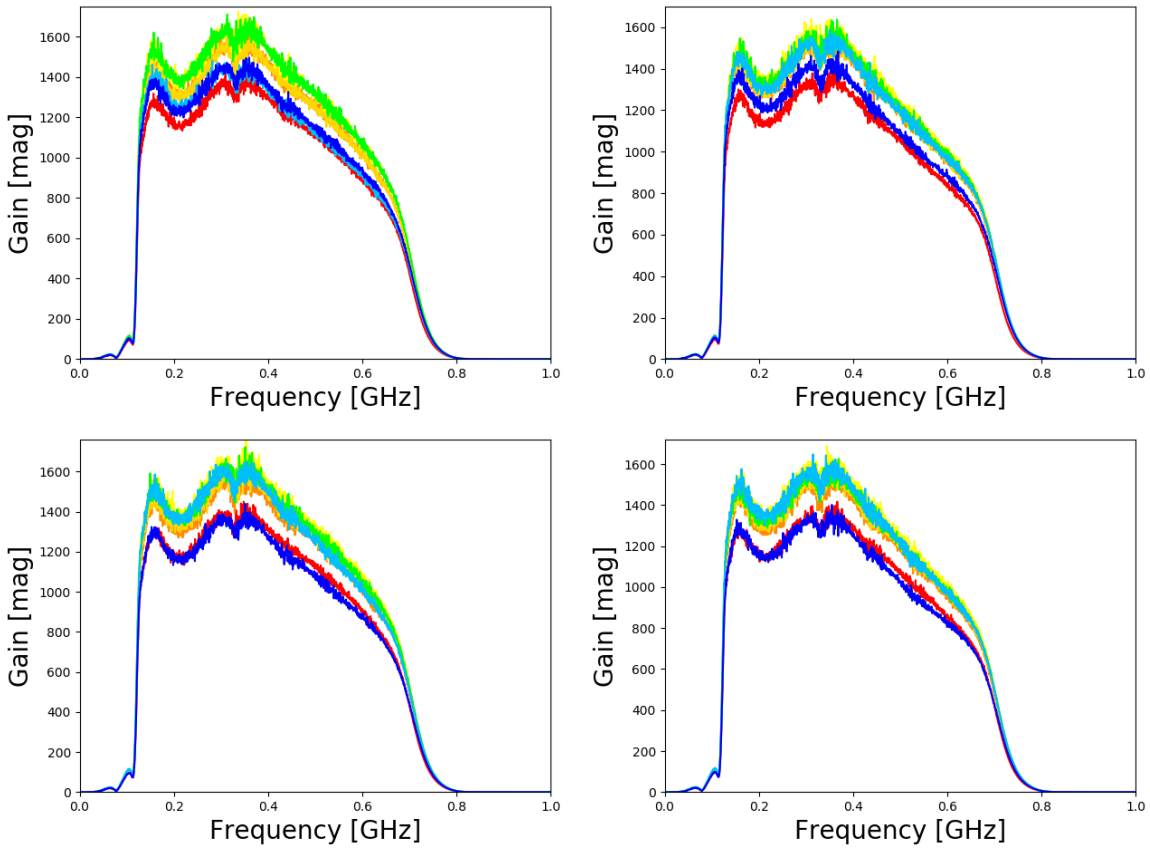

Figure 4.42: IGLU or IGLU and fiber cooled down. Top row: While the IGLU board was in the temperature chamber, DRAB and fiber stayed outside. Bottom row: IGLU and fiber were in the temperature chamber while the DRAB was outside the chamber. The same two DRAB channels have been tested in both cases (left and right). The influence of the IGLU temperature is clearly greater than the influence of the DRAB temperature. The different gain measurements have different heights but the height does not change steadily with temperature. While for the SURFACE boards the gain increased with decreasing temperature, the gain of the down-hole amplifiers only increases until -30 °C (green, left) or -40 °C (light blue, right). The temperature at which the gain starts to decrease again was mostly consistent within one board, but not entirely. With the IGLU and the fiber inside the chamber the gain measured at -50 °C (darker blue) was no longer greater than the one measured at room temperature (red).

Since there is a temperature difference of only 10 °C between the other measurements, but between these is a difference of about 23 °C, this makes sense. In the SURFACE board measurements, however, there was no discernible difference to the other measurements. The reason for the different behavior of the IGLU board

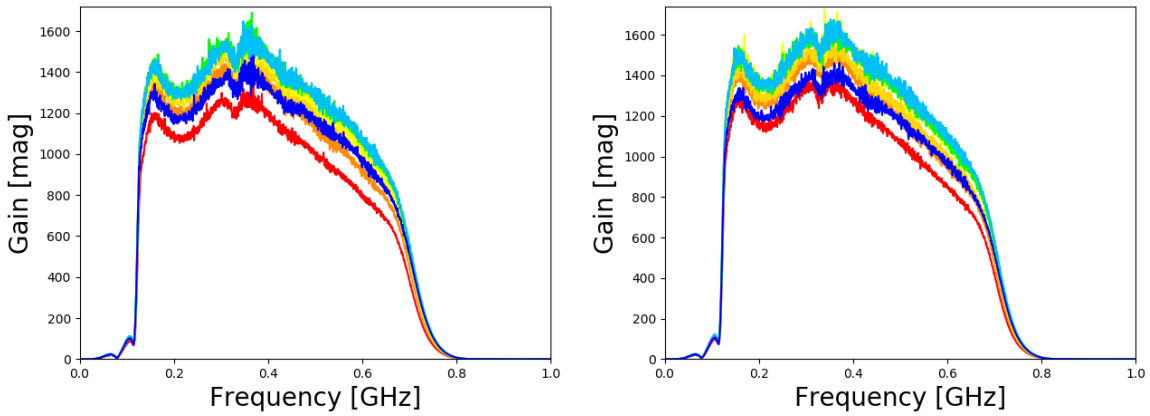

Figure 4.43: DRAB, IGLU and fiber all cooled down. Two different DRABs have been tested. The measurements look similar to the measurements with the DRAB or the DRAB and the fiber outside the temperature chamber. The gain increases until -40 °C and the gain measured at -50 °C is of similar height as the measurement at room temperature.

compared to the SURFACE board is probably the laser which apparently influences the temperature dependence of the amplifier board noticeable.

Putting the fiber in the temperature chamber as well does not change much. Like the tests with the DRAB and fiber inside the chamber already indicated, the influence of the fiber temperature on the gain is small. The gain measured at -50 °C is of about the same height or even slightly lower than the gain measured at room temperature. The highest measured gain is the one measured at -40 °C. Opposed to the case of only having the IGLU inside the chamber, this was the same for all tested channels. The influence of the fiber temperature is noticeably smaller than the influence of the IGLU temperature. In these measurements however small changes due to the fiber were found opposed to the tests with the DRABs, therefore the fiber temperatures has some influence on the gain. But the influence of the IGLU is the dominating component and influences the gain measurements clearly the most. All measured channels can be found in the appendix figure 6.26 - 6.29.

The final test was to cool down all the elements of the down-hole amplifier chain: DRAB, IGLU and fiber were all put inside the temperature chamber. This was the only test where a different channel was tested: channel 1 of DRAB A0001 instead of channel 1 of DRAB A0003. The measurements (see figure 4.43) look similar to the measurements with the IGLU inside the temperature chamber. Since the varied temperatures of the DRAB and the fiber did not change the gain very much (see figure 4.41) but the IGLU temperature had the greatest influence on the measurements (see figure 4.42), this was expected. The gain measured at room

temperature is, opposed to the measurement with the IGLU *and* the fiber in the chamber, lower than the measurement at -50 °C for the case of the channel that was not measured in the other cases (DRAB A0001 channel 1, left) and slightly lower for the other channel (DRAB A0012 channel 1, right). This shows again the somewhat different reactions of the individual DRABs to different temperatures and indicates a variation between different measurements with the same channel.

Overall the IGLU temperature has the biggest influence on the measured gain while the DRAB and fiber temperature only have little influence. The first changes in the gain measurements when cooling down the IGLU board or all components are similar to the changes in the SURFACE board measurements: The gain increases with decreasing temperature. But at a certain temperature this effect gets inverted and with further decreasing temperature the gain starts to decrease again. The temperature at which the gain begins to decrease was not the same for all boards and in a few cases it was not even the same for all channels of one board. The turning point seemed to be around -30 °C and -40 °C.

At what temperature the gain decreases instead of increasing further, is a factor of uncertainty. In general, the gain measurements displayed a maximum discrepancy of about 4.5 dB at different temperatures.

A positive result of these tests is the fact that the IGLU temperature has the most influence on the measurements: Since the IGLU will presumably experience the most consistent temperature, the measurement differences are not expected to be huge. Larger temperature changes of the DRAB and the fiber (which can occur) would not influence the gain measurements very much. Different temperatures of different components at the same time should therefore not be a big problem. Unfortunately the temperature range between -30 °C and -40 °C, which the IGLU will mostly experience, is also the temperature range in which the gain behavior is most uncertain: some channels showed an increased, some a decreased gain compared to the measurements at higher temperatures.

The temperature dependency tests of the DRABs performed for this thesis aimed at determining the influence of the temperature of the various components. The next step is to decide how these results should be implemented in a calibration: In order to be able to adjust the gain to the measured temperature, a fit function like previously done for the SURFACE boards should be found. To determine a fit function $G(T, f)$, the best combination of cooled and uncooled components has to be decided first. The most realistic scenario is probably to assume that the IGLU stays constantly at -40 °C or -30 °C while the temperature changes of the DRAB and the fiber can be neglected. A perfect model that can predict the actual behavior of every single board in Greenland under different weather conditions is not possible. But a good compromise should already be good enough, since the differences in the amplifier measurements at different temperatures are not very large. After that,

more measurements must be carried out for this particular case and in narrower temperature intervals. However, since the temperature dependency measurements of the SURFACE boards showed a significantly more uniform behavior of the various channels, larger deviations are to be expected. In order to estimate a possible function $G(T, f)$ and to estimate how large the deviations to the actual measurements will be, a fit function was determined for the data measured in this thesis, analogous to the procedure for the SURFACE boards.

In order to multiply the room temperature measurements with a function $G(T, f)$ to calculate the gain at any temperature, such a function has to be determined. For that the factor function for every measured temperature was calculated with equation 4.4. The factor function of temperature $\overline{T}$ is the average of all measurements at temperature $\overline{T}$ divided by the average of the measurements at room temperature. The factor functions can be found in figure 4.44. In the figure the factor functions of the cases *IGLU cold*, *IGLU and fiber cold* and *IGLU, DRAB and fiber cold* were compared. There are some inconsistencies, most noticeably at -50 °C: The case with the cooled down IGLU and fiber has a significantly lower factor function than the other two cases. However, if this were actually caused by the low temperature, one would expect the case of the cooled down IGLU, DRAB and fiber would decrease similarly, which is not the case. The reason for the slightly inconsistent results is probably the small number of tested channels. Cooling down all components was even only tested with two DRAB channels. The function $G(T, f)$ was determined for the case of the cooled down IGLU while DRAB and fiber stayed at room temperature.

Hence, every factor function at every temperature was fitted for the case of the cooled down IGLU. The fit function method makes it possible to calculate the gain curve for a measurement at a temperature between the measured temperature intervals and therefore allows a steady transition between the temperatures. To get a fit function for all temperatures and frequencies of the type: $G(T, f) = a(T) + b(T) \cdot f^6$ the parameters a and b have to be determined for each temperature. First, the parameters a and b are picked for every temperature individually to get the best result. Then they are plotted as a function of temperature and fitted to get the functions $a(T)$ and $b(T)$. Unfortunately the first picked parameters spread very random, therefore a few iterations were necessary to pick parameters that could be fitted (see figure 4.45). For parameter a two functions were picked: $a_1(T)$ for $T \leq -20\,°\mathrm{C}$ and $a_2(T)$ for $T \geq -20\,°\mathrm{C}$. This allows a steady transition at -20 °C and better fitting functions for all temperatures than just using one function. Still, the resulting functions $a(T)$ and $b(T)$ do not work very well.

The decision to change $a(-10\,°\mathrm{C})$ and $a(0\,°\mathrm{C})$ most drastically is motivated that the measurements between 0 °C and -10 °C showed a decrease of parameter a. But since an *increase* of the gain was expected between 0 °C and -20 °C (this

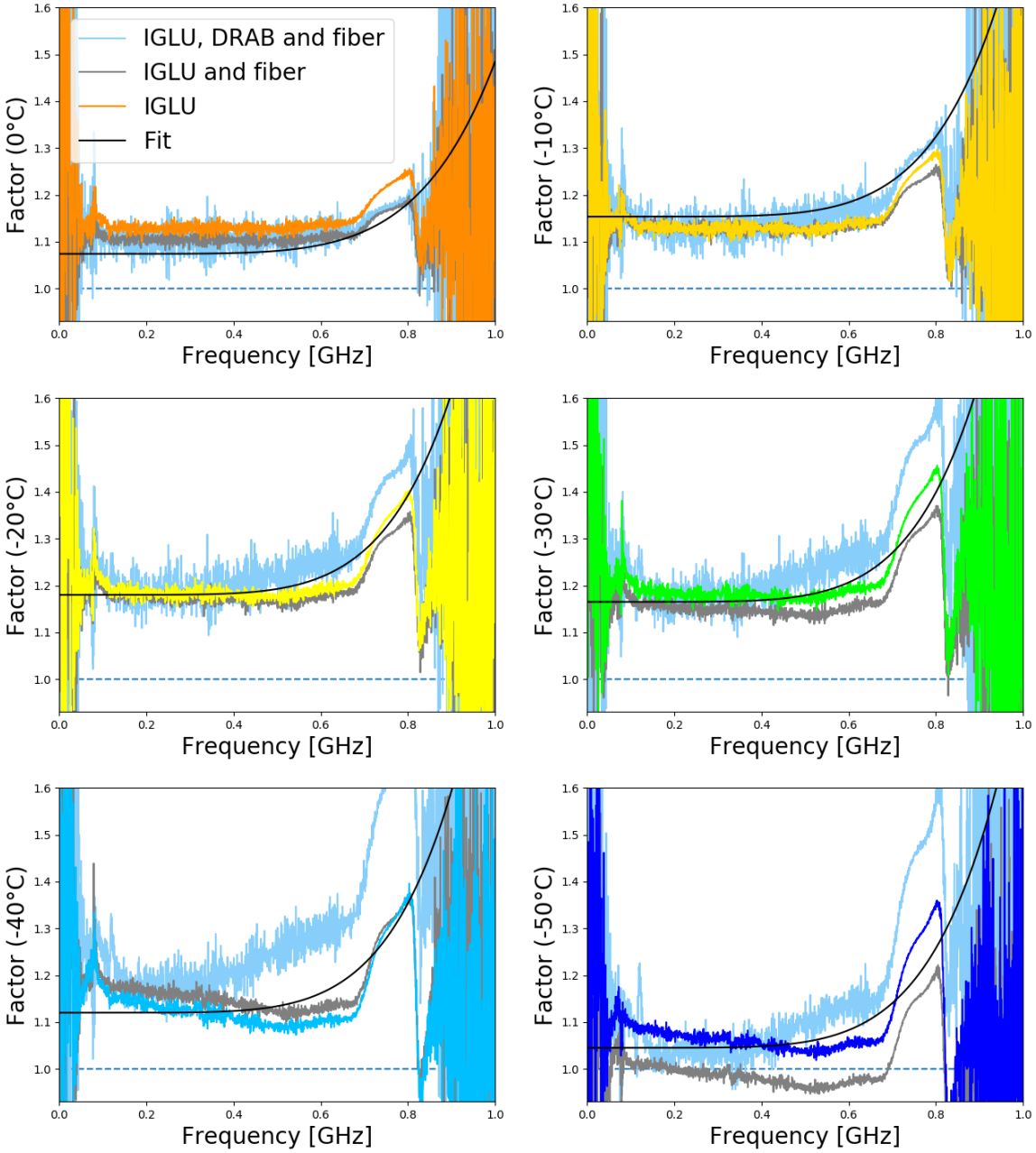

Figure 4.44: Temperature dependence: Fits of the factor functions for the gain measurements of the DRABs. Above are the factor functions for the three cases: *IGLU cold*, *IGLU and fiber cold* and *IGLU, DRAB and fiber cold* displayed. Shown are the fits (see table 4.9) for several temperatures. The fits were determined for the case that only the IGLU is cooled down. But since the disadvantage of the fit function $G(T, f)$ is, that the fit does not work very well for every single factor function of every temperature, the fit would work similarly for the other cases.

was the matter in all other cases) and otherwise a steady transition of a between all temperatures would not have been possible, the fit for $a(-10\,°\mathrm{C})$ and $a(0\,°\mathrm{C})$ deviates a lot from the measurements. It is entirely possible that more measurements will change the observed trend, as a decrease in this temperature range is unlikely.

The resulting functions $a(T)$ and $b(T)$ in figure 4.45 are fitted with the functions:

$$\begin{aligned} a_1(T) &= 1.18 - 0.00015 \cdot (T+20)^2 \\ a_2(T) &= 1.18 - 0.000265 \cdot (T+20)^2 \\ b(T) &= 0.9 - 0.0004 \cdot (T+35)^2. \end{aligned} \tag{4.8}$$

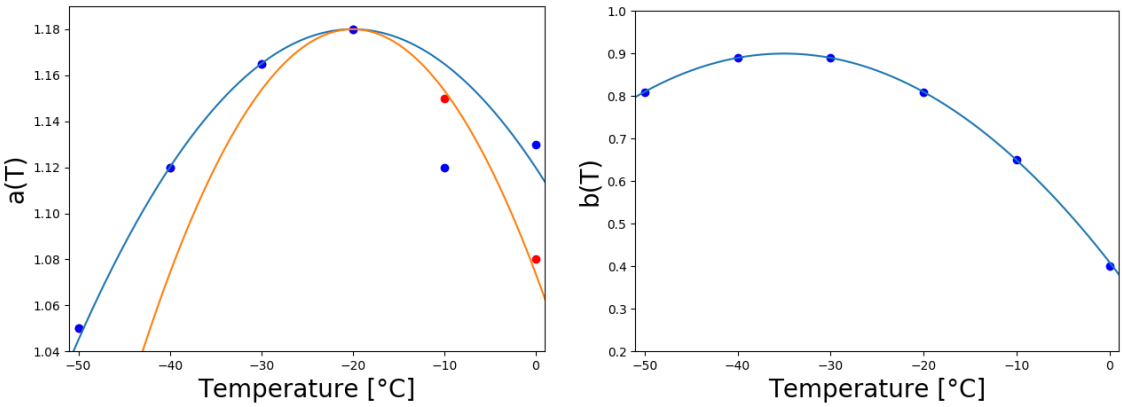

Figure 4.45: The fits to the parameters (blue dots) $a(\overline{T})$ (left) and $b(\overline{T})$ (right) for $\overline{T}$ = 0 °C, -10 °C, -20 °C, -30 °C, -40 °C, -50 °C are displayed in the figures. The parameters that were chosen first individually for every measured temperature were further adjusted to allow a fit. This worked well in the case of parameter b, but parameter a varied a lot. Therefore, the new parameters selected here for 0 °C and -10 °C (red points) cause large deviations. In addition, two fit functions (blue and orange) were used that intersect at -20 °C and thus enable a transition. A fit function can therefore be found for each temperature, but the results deviate significantly from the measurements (see figure 4.46).

Therefore the equation $G(T,f) = a(T) + b(T) \cdot f^6$ with $G_1(T,f)$ for $T \leq -20\,°\mathrm{C}$ and $G_2(T,f)$ for $T \geq -20\,°\mathrm{C}$ becomes:

$$\begin{aligned} G_1(T,f) &= 1.18 - 0.00015 \cdot (T+20)^2 + (0.9 - 0.0004 \cdot (T+35)^2) \cdot f^6 \\ G_2(T,f) &= 1.18 - 0.000265 \cdot (T+20)^2 + (0.9 - 0.0004 \cdot (T+35)^2) \cdot f^6. \end{aligned} \tag{4.9}$$

The fit functions for the measured temperatures can be found in table 4.9 and in figure 4.44. Although the used fit function was determined for the cold IGLU case,

Temperature	Fit Function	68 % Quantile
0 °C	$1.08 + 0.04 \cdot f^6$	5.21 %
-10 °C	$1.15 + 0.65 \cdot f^6$	4.17 %
-20 °C	$1.18 + 0.81 \cdot f^6$	2.72 %
-30 °C	$1.165 + 0.89 \cdot f^6$	3.23 %
-40 °C	$1.12 + 0.89 \cdot f^6$	6.63 %
-50 °C	$1.05 + 0.81 \cdot f^6$	4.08 %

Tables 4.9: Fit functions for different temperatures depending on the frequency f [GHz] and the 68 % quantile of the deviation between 80 MHz and 700 MHz for these fit functions.

it shows similar results for the other cases. When compared with the fit functions of the SURFACE boards (see figure 4.33), the fit functions of the down-hole amplifier boards clearly work less well.

The deviation of the gain calculated with the fit function from the measured gain was calculated with equation 4.5 and can be found in figure 4.46. Since the fit functions clearly differ from the factor functions, it was expected that the deviation from the average measurement would be large opposed to the relatively small deviation of the SURFACE boards (see figure 4.36). To quantify the deviation, the 68 % quantile was calculated and can be found in table 4.9. For the different temperatures the 68 % quantile varies, but the average is about 4.34 %. The deviation of the fit function for all temperatures is at least 2.72 %, while the fit for -40 °C (6.63 %) shows the highest deviation.

The results could certainly be improved through a larger number of tests, but the accuracy of the fit function for the SURFACE boards will probably not be achieved. However, since it is assumed that the IGLU temperature does not change very much, it could make sense to pick the fit function on the basis of the relevant temperature range (between about -40 °C and -30 °C). Therefore less sufficient parameters a and b for higher and lower temperatures would be accepted, while a good fit in this temperature range would be prioritized.

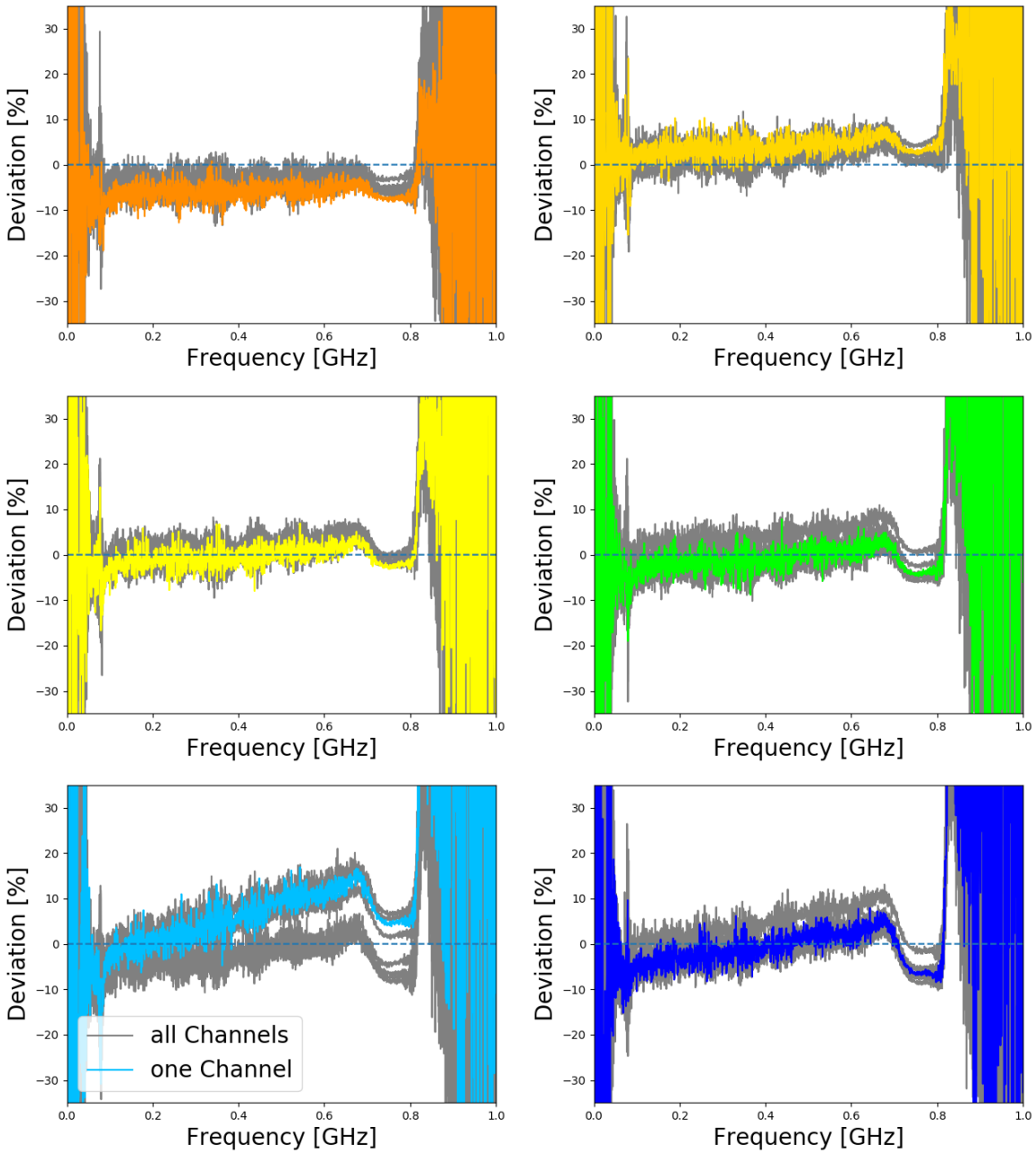

Figure 4.46: Temperature dependence: Deviation of the gain calculated with fit functions, from the gain measurements of all eight measured DRAB channels. The gain is calculated for every measured temperature by multiplying the room temperature measurement with the fit function (see table 4.9) of the corresponding temperature. The calculated gain distinctly deviates from the actual measurements, especially for -40 °C (bottom left). The 68 % quantile (see table 4.9) is between 2.72 % (-20 °C) and 6.63 % (-40 °C). This is significantly larger than the deviation for any method to calculate the SURFACE board gain (see table 4.7).

5 Summary and Conclusions

Neutrinos are important messenger particles that contribute to the exploration of the high-energy universe. Although neutrinos are difficult to detect due to their small interaction cross-section, the advantage of using neutrinos as messenger particles is that they directly point back to their origin. Ultra-high-energy neutrinos therefore promise to play an essential role in the identification and investigation of cosmic ray sources and their production and acceleration mechanisms. When these cosmic neutrinos reach Earth, they are difficult to detect. One way is the radio technique, measuring the radio emission of neutrino induced secondary particle cascades in dense media. The great advantage of detecting neutrinos via radio emission is the new, higher energy range it promises to explore.

The Radio Neutrino Observatory in Greenland aims at measuring neutrinos with energies above 10 PeV in glacial ice. The detector will consist of a down-hole and a surface component: antennas will be placed in a 100 m deep borehole and at the surface to detect radio signals. The detector stations will be arranged in a 1 km spaced grid. The deployment of the first of the overall 35 detector stations starts summer 2021.

The calibration measurements of the custom designed amplifier boards of RNO-G were described and analyzed in this thesis. The signals observed in both components (surface and borehole) follow different signal chains: the signals measured with the surface antennas are amplified with the SURFACE boards. The signals captured with the antennas of the deep component get amplified and transmitted via DRAB and IGLU boards. The experiences with the first detector stations will not only play a decisive role elaborating the second generation of RNO-G hardware and shape the perspective of future radio detector projects. The established testing process will also influence future measurement proceedings. It is therefore important to develop a reproducible and precise test and calibration procedure right from the start to evaluate the performance of the detector stations.

The testing procedure laid down in this thesis not only searched for defective boards to be sorted out or repaired and looked for features that should be revised for the next generation of amplifier boards. The tests also studied the influence of different parameters on the measurements, determined various properties of the different board types and quantified the differences between the individual boards.

The test procedure can be divided into four phases: the function tests, the performance tests, testing the influence of different components and the temperature

dependence tests.

First, the functionality and the temperature resistance of the boards was tested. After a first function test the boards were cooled down, afterwards another function test was done. There was no temperature related board malfunction. A few IGLUs and one DRAB channel showed some issues (no signal, low current draw) in the function tests, a couple of them - the ones showing no signal - were fixed.

In the next step the performance of the boards was evaluated to determine the characteristics and average values of some properties of one board type to then identify boards with an insufficient performance and divergent features. The S-parameters of the SURFACE boards as well as the S-parameters of the DRAB and IGLU boards (measured together) were measured and showed sufficient results. The gain measurements were further analyzed. The deviation of the different channels from the average of the corresponding board type were quantified. The gain measurements revealed a convincing uniformity of the SURFACE boards. The DRABs exhibited more spread in the gain measurements but are still overall quite similar. Regardless, all amplifiers are individually calibrated in order to reduce systematic uncertainties in the signals that are reconstructed. Only two DRABs and one SURFACE board showed an unsatisfactory deviation, while a couple of DRABs only barely passed. The down-hole amplifier gain measurements all show a small anti-resonance at 326 MHz. It could not be determined whether the origin is the DRAB or the IGLU board, since all measurements, regardless which individual board was used, showed the anti-resonance. Since the undesired and unexpected feature is very small it is not a big concern but it is still puzzling and future tests might determine the origin of it. The anti-resonance also shows up as a small feature in all group delay measurements. The anti-resonance was quantified in the gain and the group delay measurement. Despite that, the group delay of the SURFACE boards and DRABs revealed relatively even passbands and promise therefore only a slight signal distortion. The crosstalk measurements were carried out with only a few SURFACE boards and DRABs. The measurements showed little interference and showed how effectively the enclosures suppresses crosstalk between the channels on a board. The noise figure measurements done for this thesis are incorrect, probably because the measurement settings were wrong. The measured noise is significantly higher than the noise previously determined for the boards. The measurement procedure must therefore be revised in order to accurately determine the noise figure of the boards. Overall the amplifier measurements reached their expectations and exhibited a good uniformity.

In the third test phase, the influence of various components and parameters was examined. Due to problems with the first fiber that was used and to investigate the influence of the used fiber, three fiber cables of different lengths were tested. The tests showed no dependence of the measured values on the length of the fiber. The

SURFACE boards hardly show any random errors, but there are some variations when measuring the same DRAB repeatedly. While the influence of the used individual DRAB and SURFACE board were already analyzed in the performance testing stage, the influence of the used IGLU was tested in this phase. The IGLU influence on the down-hole amplifier measurements is comparable to the DRAB influence. One IGLU showed a higher low-pass cutoff than the other boards and was sorted out.

In summary, all 12 SURFACE boards worked, but the gain measurements displayed that one channel of one board deviated very much from the other channels (SURFACE board A0007). 43 out of the 47 IGLU boards passed the function test, four had an unexpectedly low current draw (IGLUs: A0033, A0009, A0012, A0037) and one boards showed a higher low-pass cutoff in the gain measurements (IGLU A0004). All 23 DRABs worked, but two of them (DRAB A0011 and DRAB A0015) had channels which gains deviated slightly more than 2 dB from the average. A few more boards showed deviation values just below the ± 2 dB limit. Therefore 11 SURFACE boards, 42 IGLU boards and 21 DRABs passed all tests.

The last amplifier board tests studied the influence of the temperature at which the data was measured, to understand how the measurement results depend on the temperature. The SURFACE board temperature testing focused on finding an adequat way to account for changes in the amplifier measurements due to temperature variations, rather than measuring each board at various temperatures. The DRAB and IGLU board tests on the other hand examined the influence of the temperature of various components on the measurements.

Overall the temperature dependence tests showed some positive results: Fortunately, the measurements of the SURFACE boards change very evenly with temperature. Different ways to implement this in the data analysis of the measured data of RNO-G were tested and showed promising results. Since the temperature of the SURFACE board is assumed to vary a lot, it is important to have a good method to consider the temperature dependence of the amplifier gain. The testing of the DRABs and IGLU boards was more complex but the influence of the different components was determined: The IGLU board temperature has the most influence on the down-hole amplifier chain measurements, the laser is probably the exact component that is dominating the temperature dependence. Since the IGLU will presumably experience the most consistent temperature, the measurement differences are not expected to be huge. The influence of the DRAB and fiber temperatures are only minor. The only negative results are, that unfortunately the temperature range which the IGLU will mostly experience is also the temperature range in which the gain behavior is most uncertain: some channels showed an increased, some a decreased gain compared to the measurement at higher temperatures. Additionally the gain of the down-hole amplifiers did not change as smoothly

and consistently as the gain of the SURFACE boards.

More temperature tests in the future are necessary: More channels of more different DRABs have to be tested to determine a good fit function. Currently all data comes from only two different DRABs. The best approach seems to be to carry out the measurements with the IGLU (or the IGLU and the fiber) in the temperature chamber while the DRAB is outside. It therefore is advisable to carry out more measurements in this constellation in upcoming tests to determine an adequate fit function for the down-hole amplifiers. Furthermore these tests can be used to study the differences in the response of the different boards and channels to being cooled down, especially in the range between -30 °C and -40 °C. Hence, it would certainly make sense to examine the temperature range between -30 °C and -40 °C more closely and to take measurements at least in this range in narrower temperature intervals. Thereby, it could be determined more precisely at which temperature the gain starts to decrease again instead of increasing further when the temperature decreases and how much this differs between different channels (or boards). In addition, the temperature tests should also be carried out with different IGLUs, so far all tests were done with the same IGLU. In particular since three different types of laser were used on the various IGLU boards.

Additionally, it might be interesting to cool down one board of every board type to -75 °C (minimum temperature of the temperature chamber) to test the functionality of the boards after extreme temperatures. Furthermore studying the effect of keeping the boards at a low temperature for a longer period of time might be an idea for future tests.

Aside from the ideas for new tests, future boards should be tested according to the scheme in figure 5.1, summarizing the developed testing procedure. The procedure was designed on the basis of the tests in this thesis and ensures systematic and effective testing of the boards.

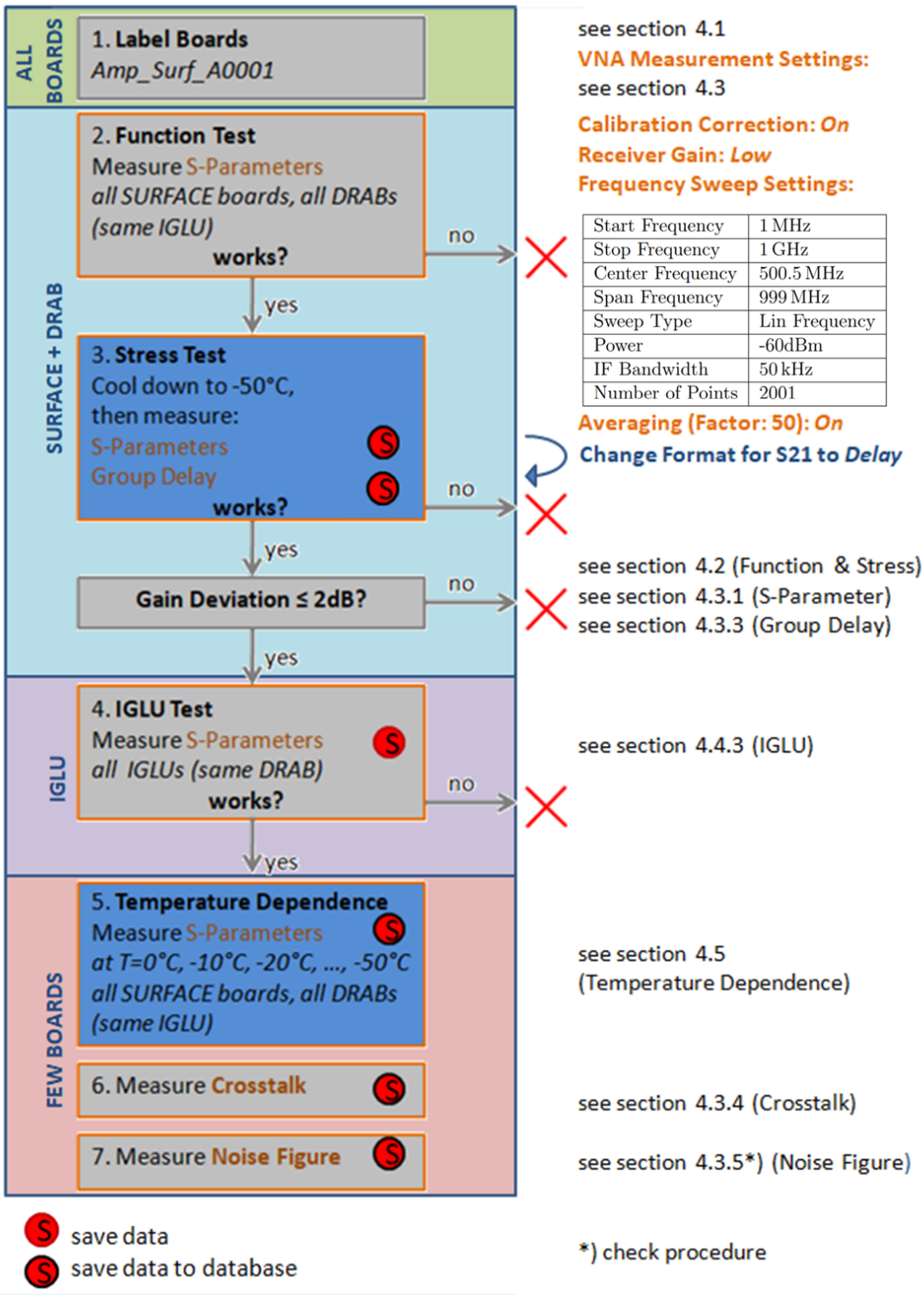

Figure 5.1: Flow chart: Standard test procedure to test the amplifier boards of RNO-G. The order of steps 5. to 7. is interchangeable.

6 Appendix

6.1 Effects of the COVID-19 pandemic

The worldwide COVID-19 pandemic also affected the work on this thesis.

The production of the IGLU board enclosures had to be put on hold because of the lockdown of the workshop manufacturing the enclosures due to the pandemic and they were only finished after the tests. Therefore the IGLU boards were not in their enclosures for any tests that are described in this thesis.

Due to delivery issues with the VNA the first function tests before and after the stress tests (see section 4.2) were done with an oscilloscope and a sine wave generator to just check if the boards worked. The functionality could have been tested by just measuring the S-parameters with the VNA. Thereby the S-parameter measurements before and after cooling the boards down for the first time could have been compared. This could be a test for the following generation of amplifier boards.

The pandemic strongly influenced the work and the timetable of the whole RNO-G project. The deployment start of the RNO-G detector, originally planned for summer 2020, is now planned for summer 2021.

6.2 Additional Figures

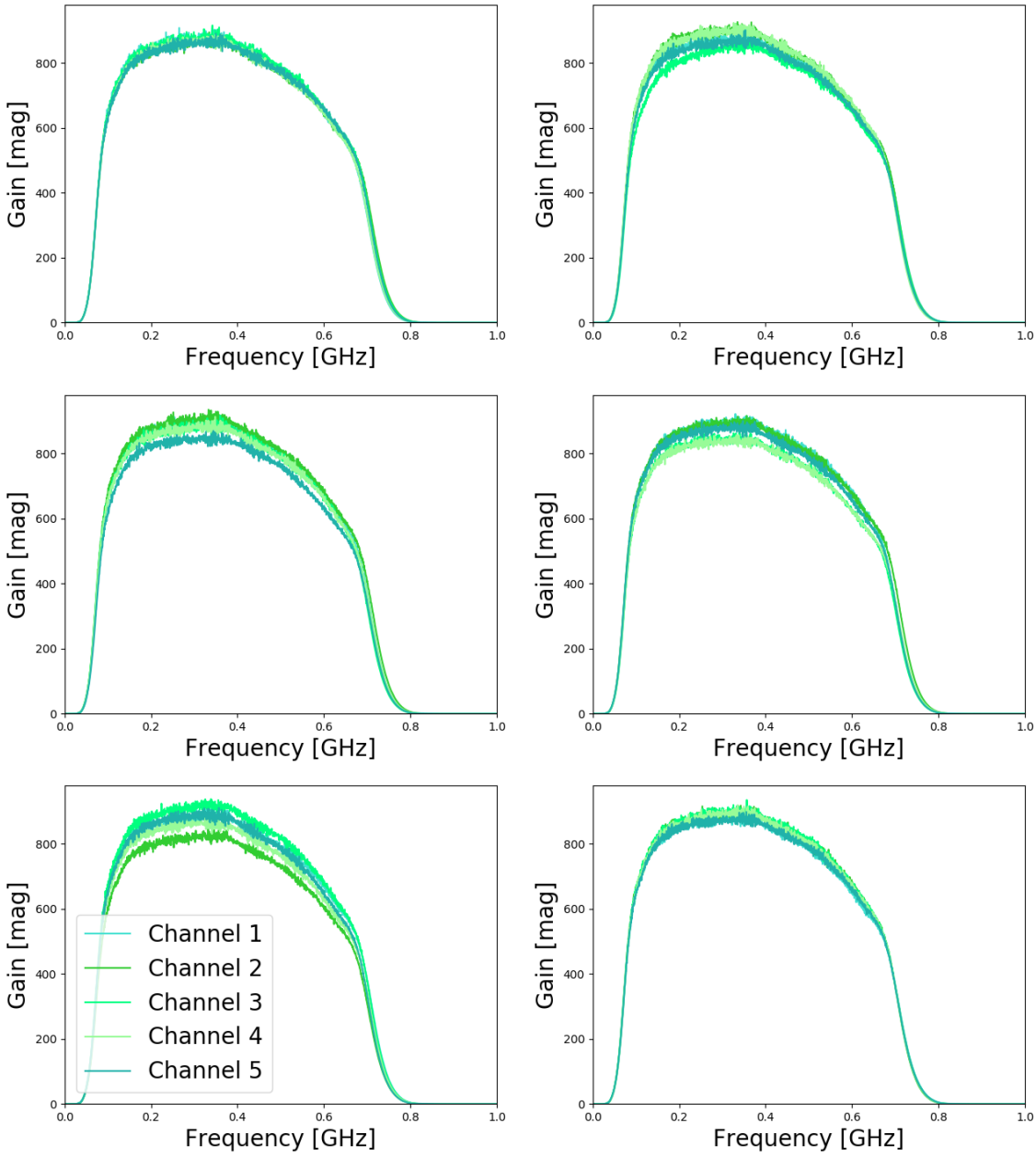

Figure 6.1: Gain of SURFACE boards [mag]: Board A0001-A0006.

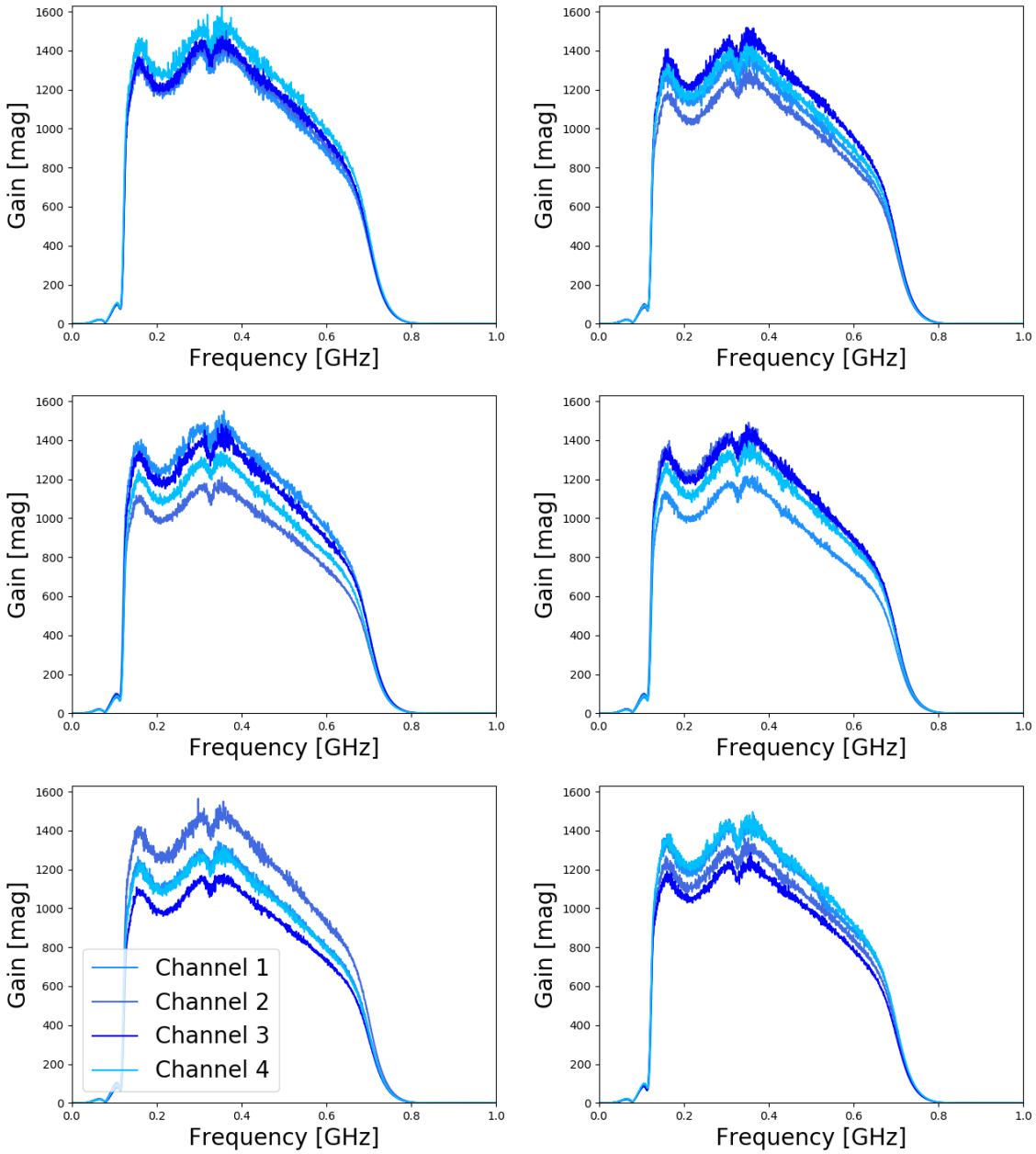

Figure 6.2: Gain of DRABs [mag]: Board A0001-A0006.

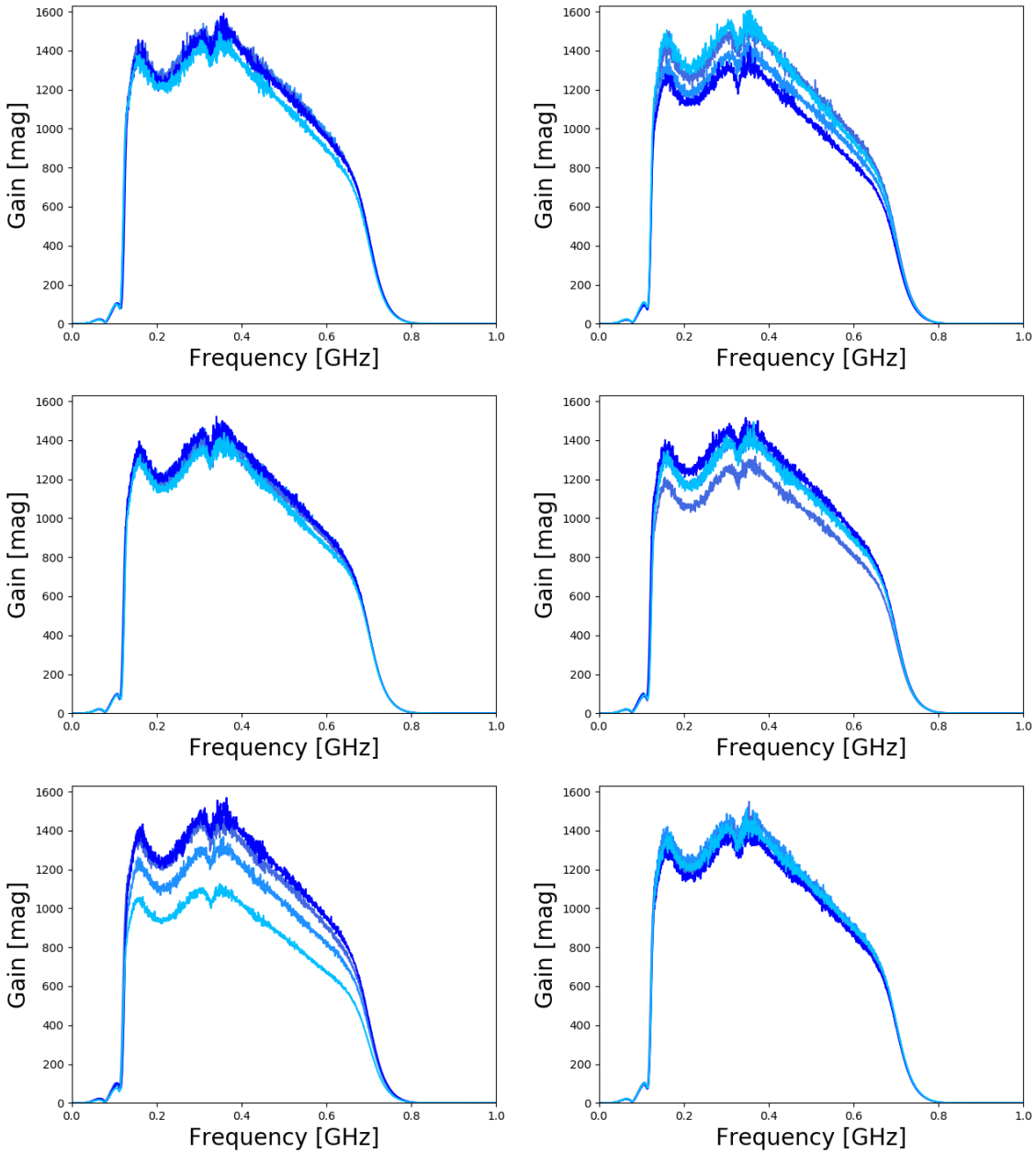

Figure 6.3: Gain of DRABs [mag]: Board A0007-A0012.

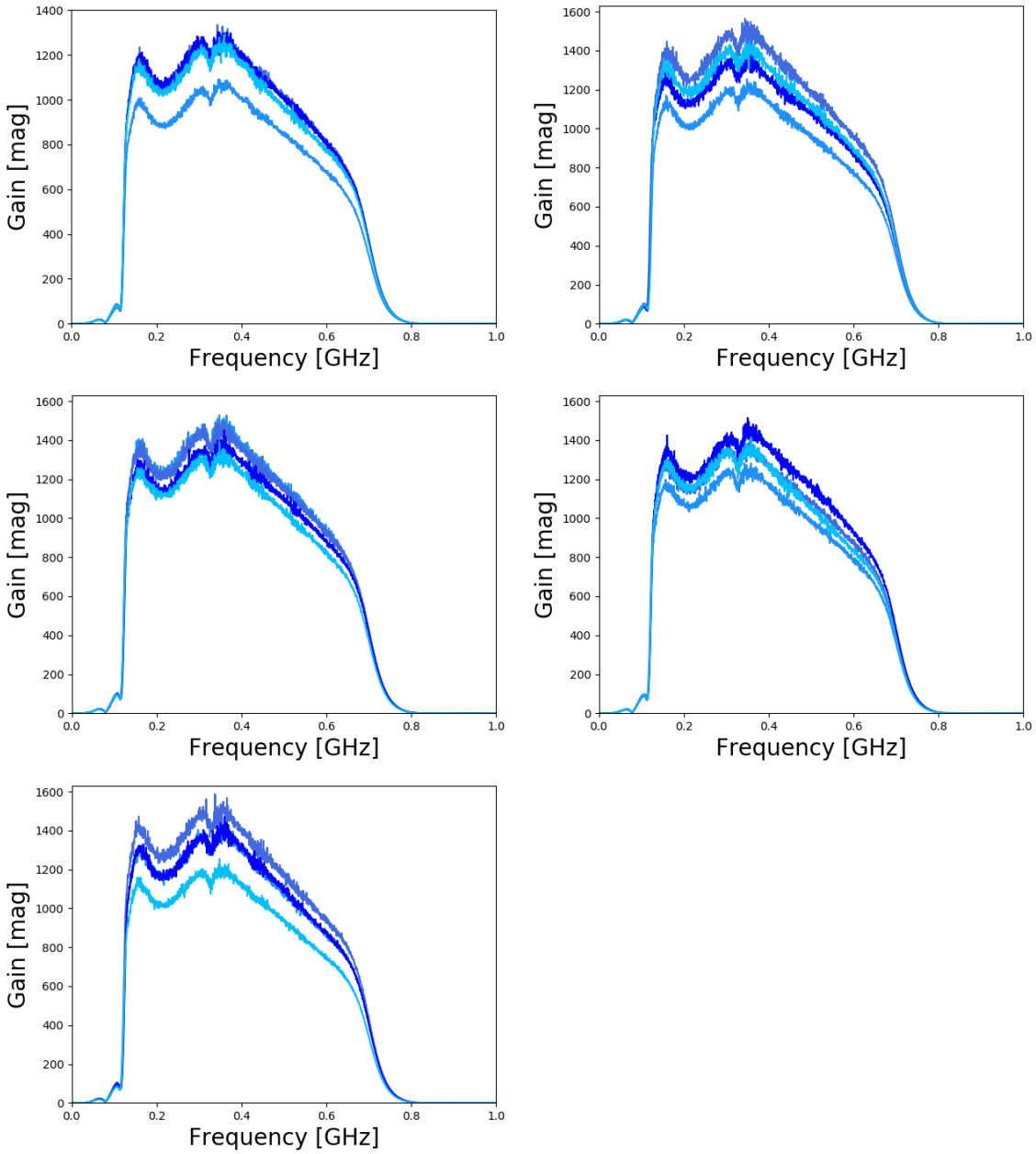

Figure 6.4: Gain of DRABs [mag]: Board A0019-A0023.

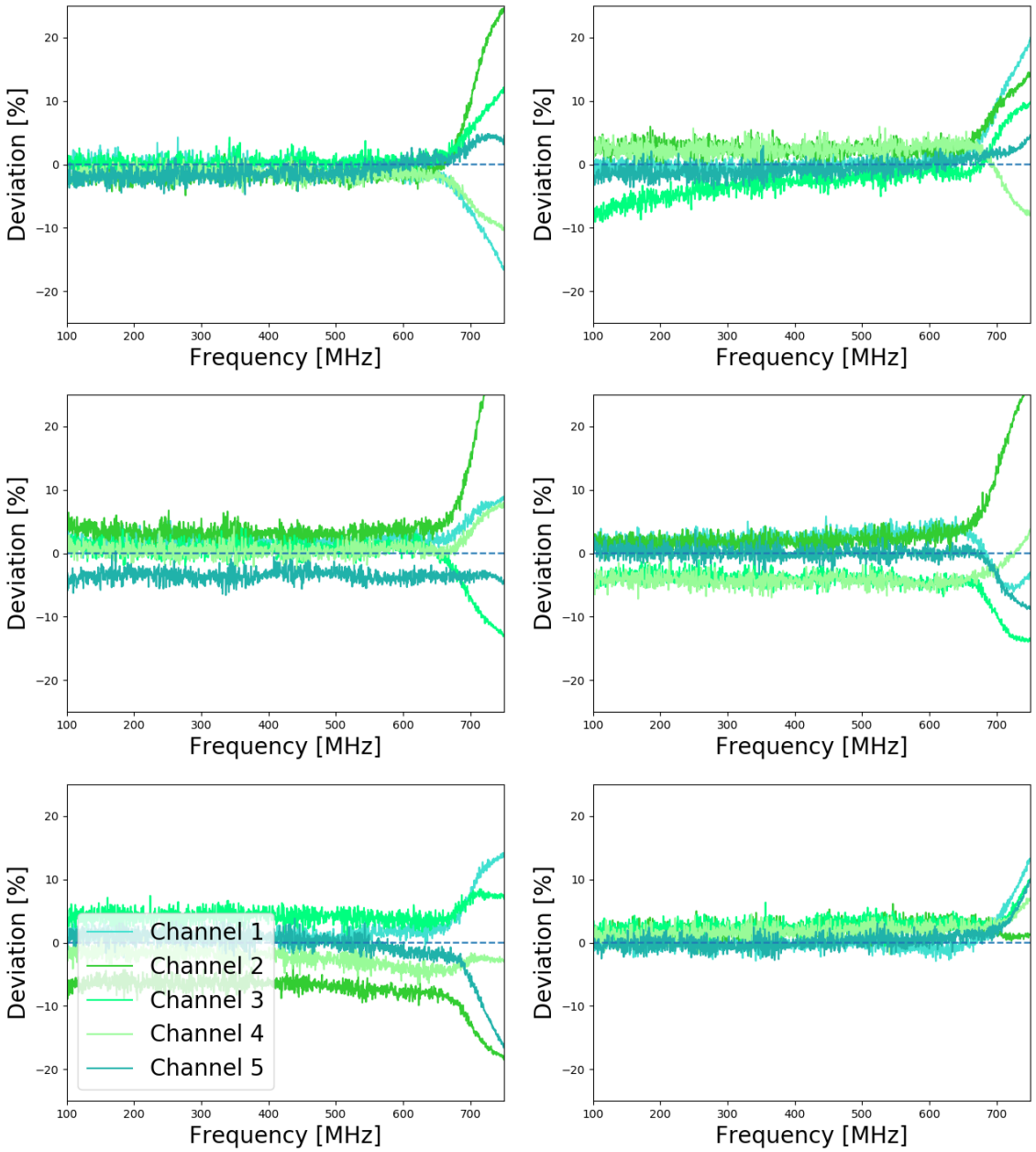

Figure 6.5: Deviation from the average [%]: Board A0001-A0006.

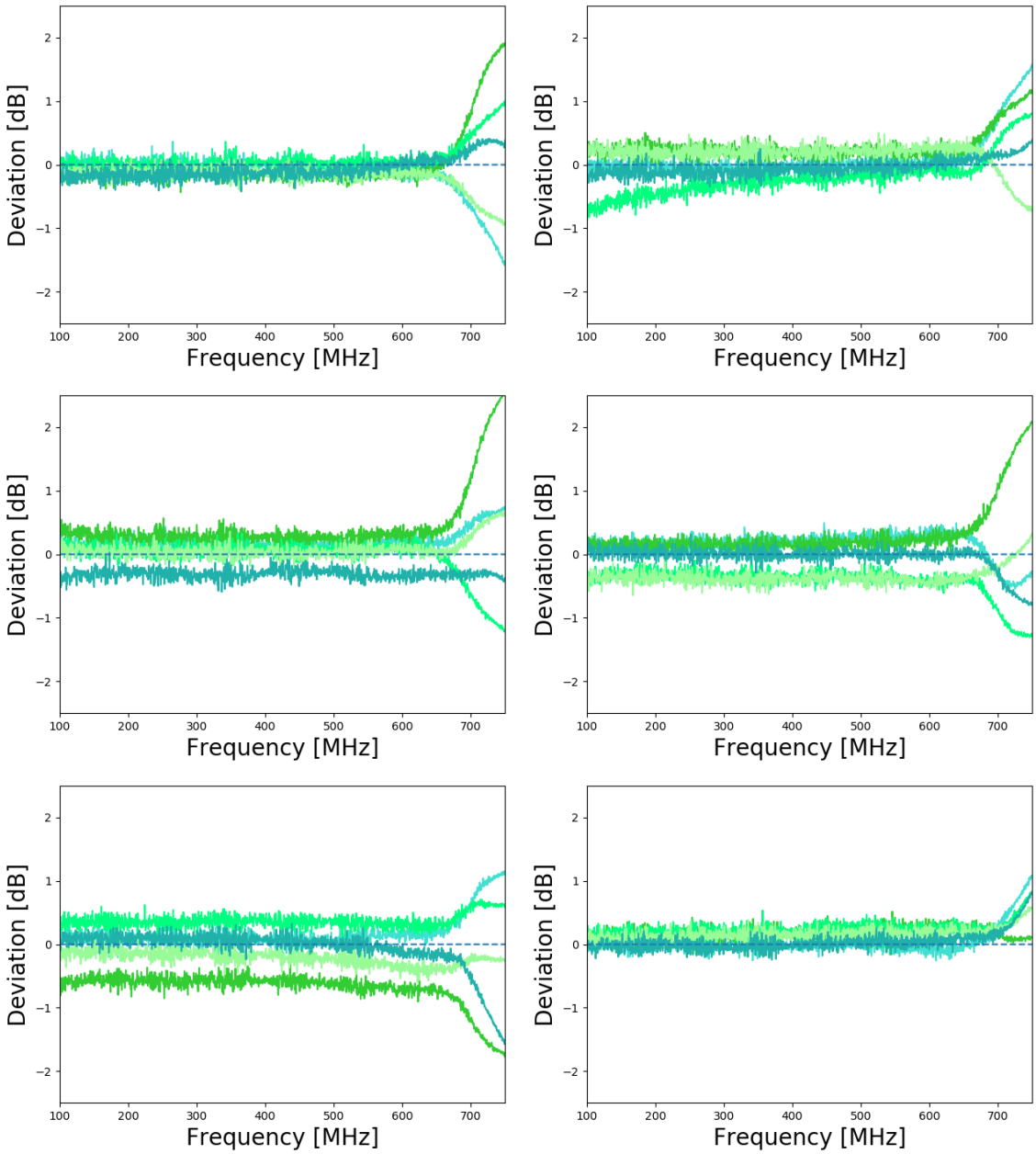

Figure 6.6: Deviation from the average [dB]: Board A0001-A0006.

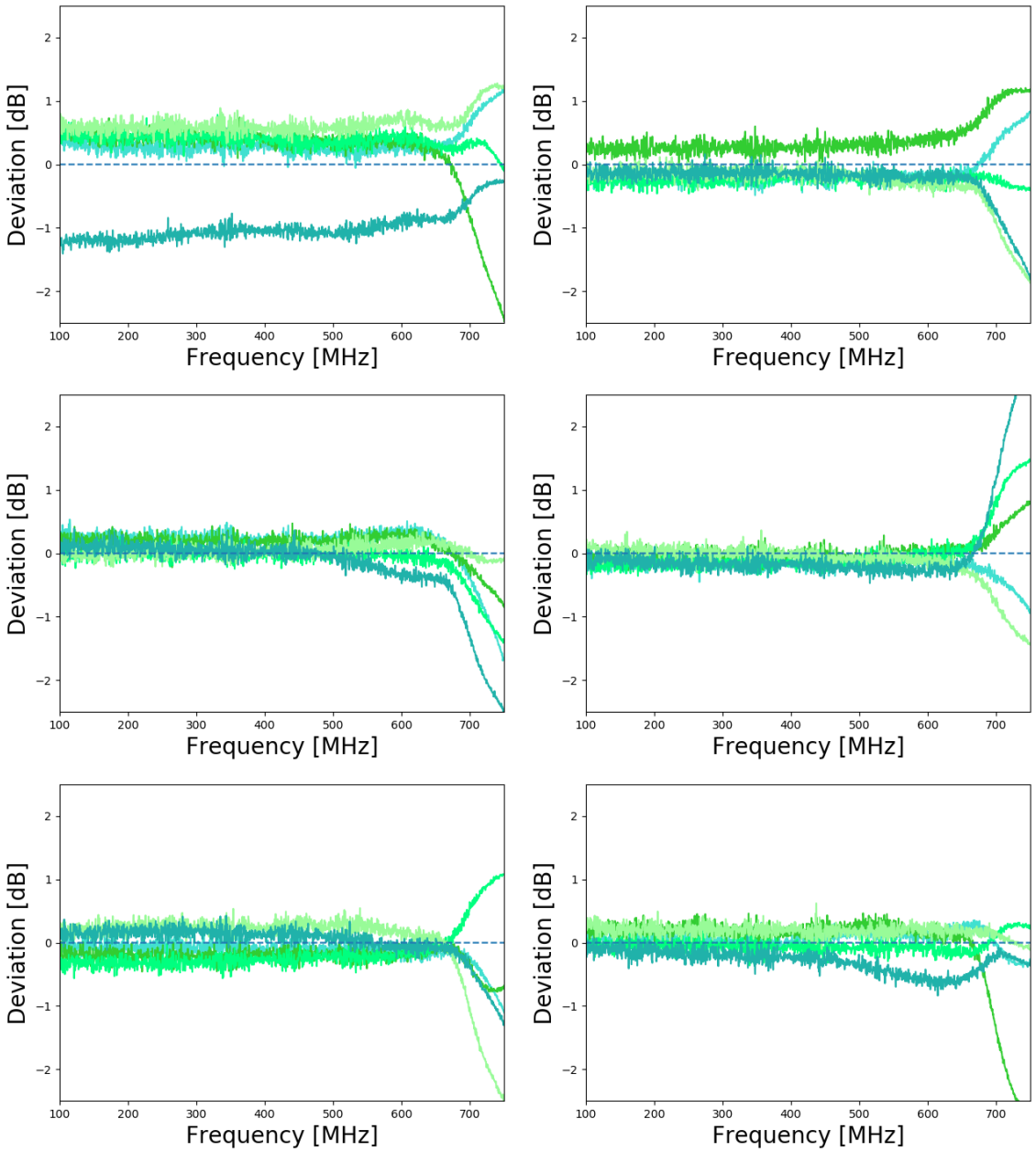

Figure 6.7: Deviation from the average [dB]: Board A0007-A0012.

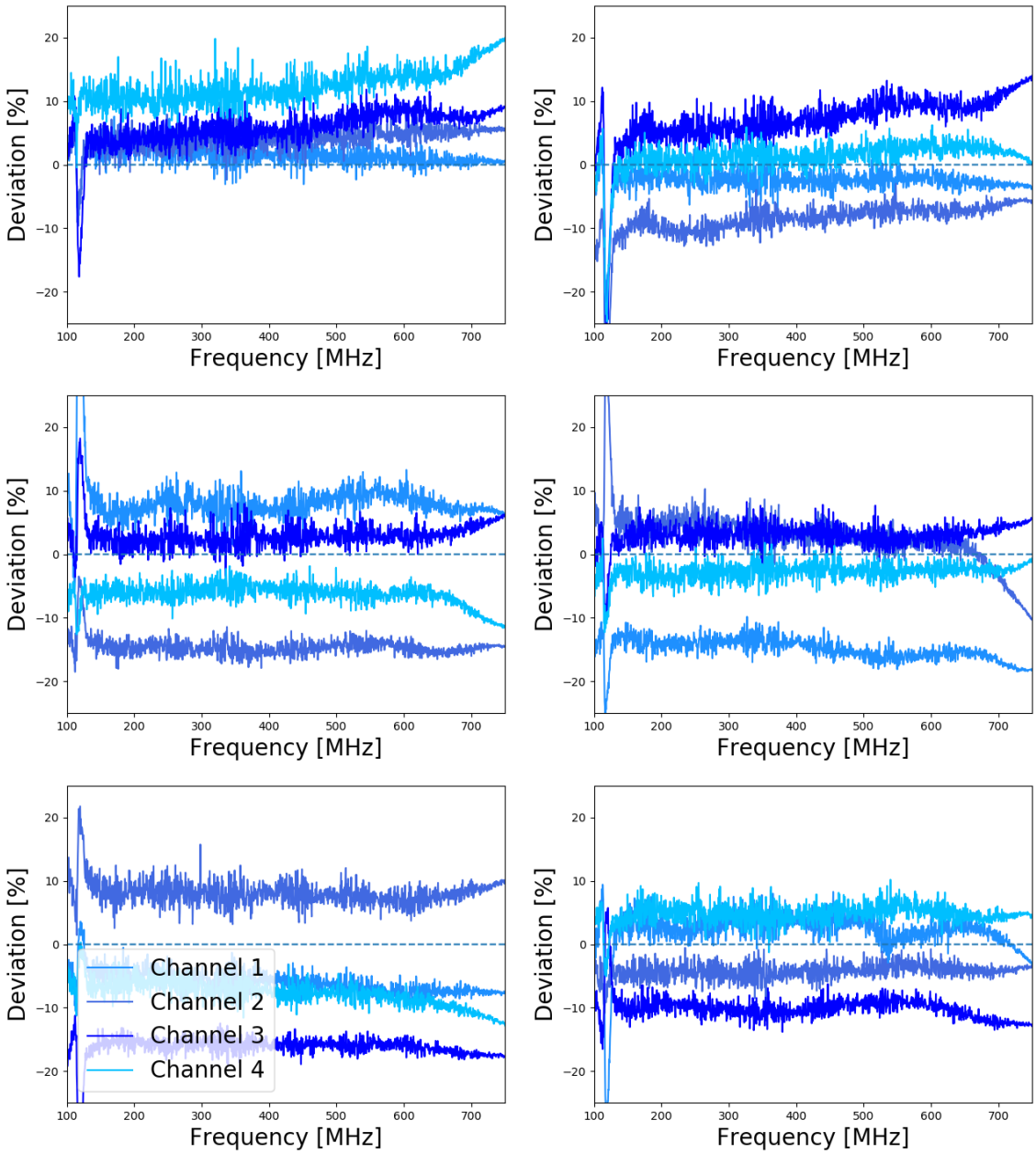

Figure 6.8: Deviation from the average [%]: Board A0001-A0006.

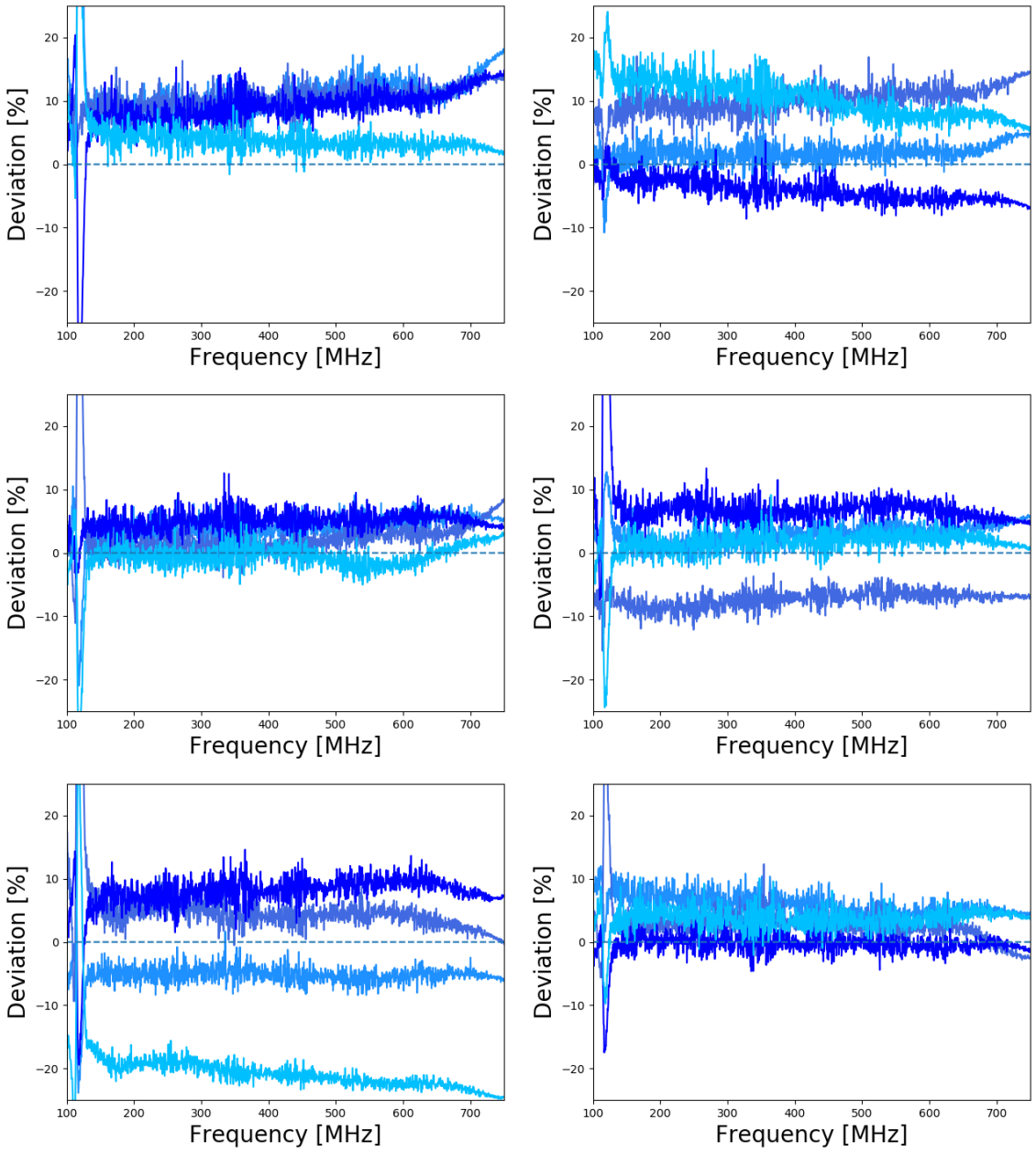

Figure 6.9: Deviation from the average [%]: Board A0007-A0012.

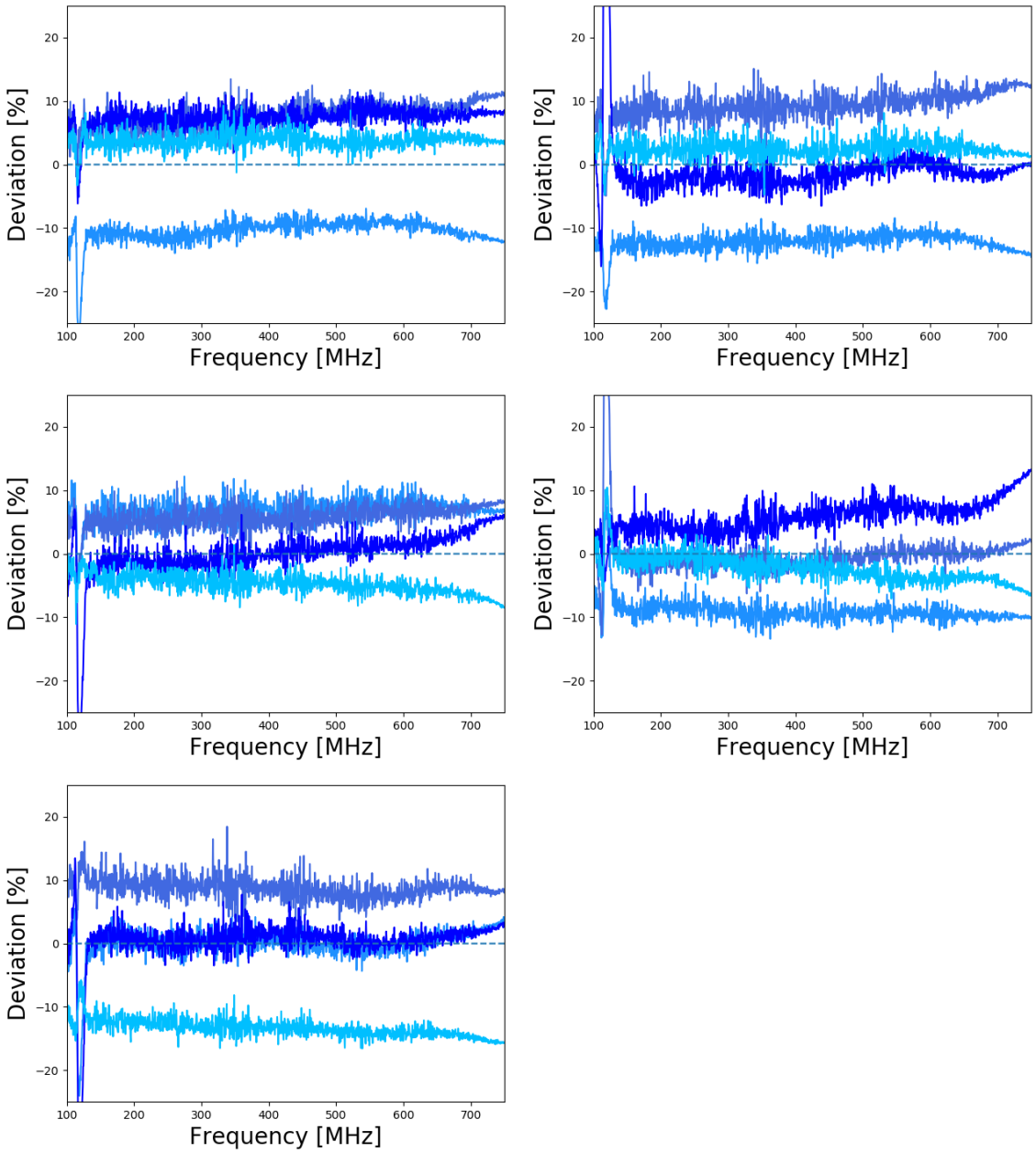

Figure 6.10: Deviation from the average [%]: Board A0019-A0023.

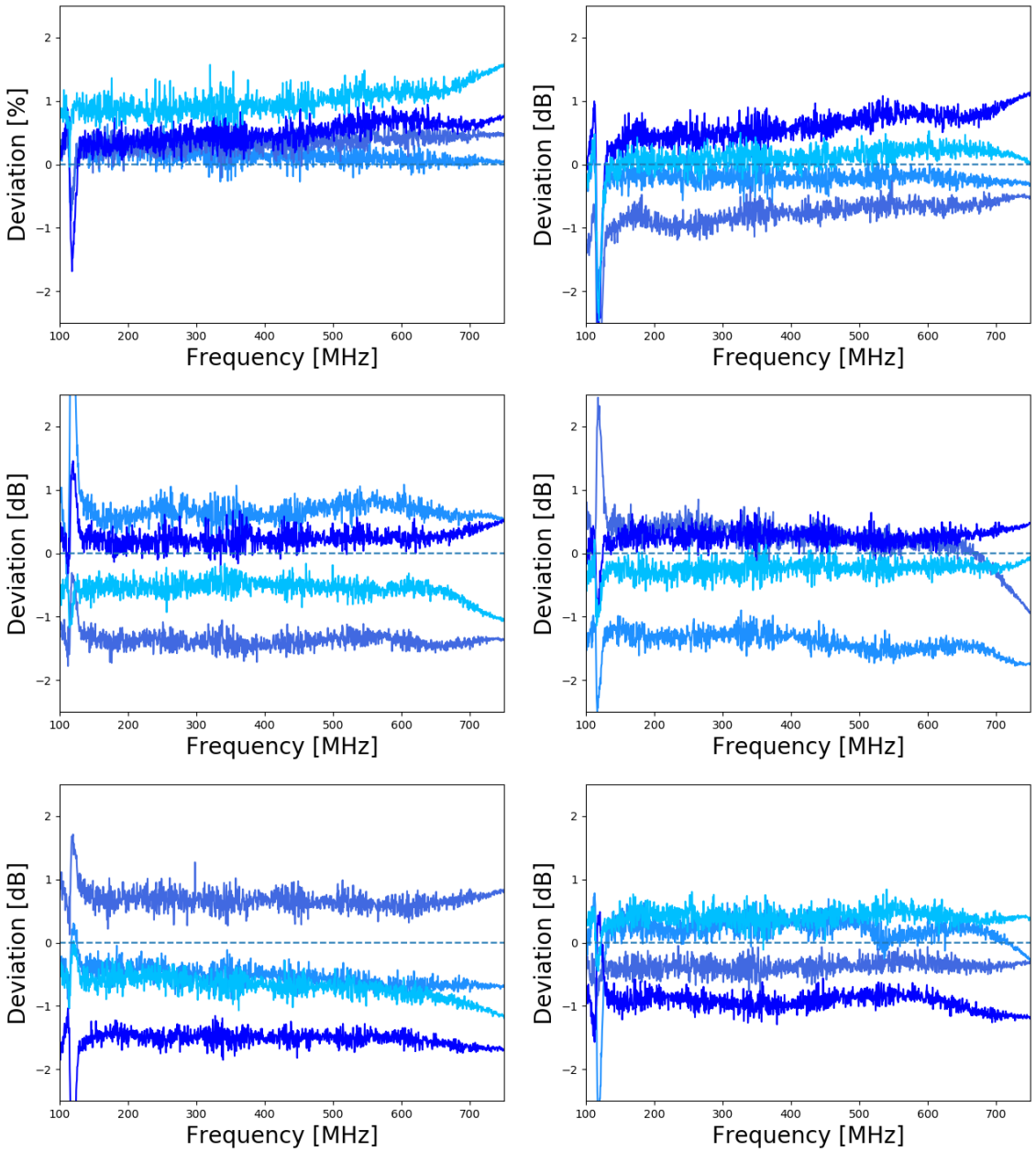

Figure 6.11: Deviation from the average [dB]: Board A0001-A0006.

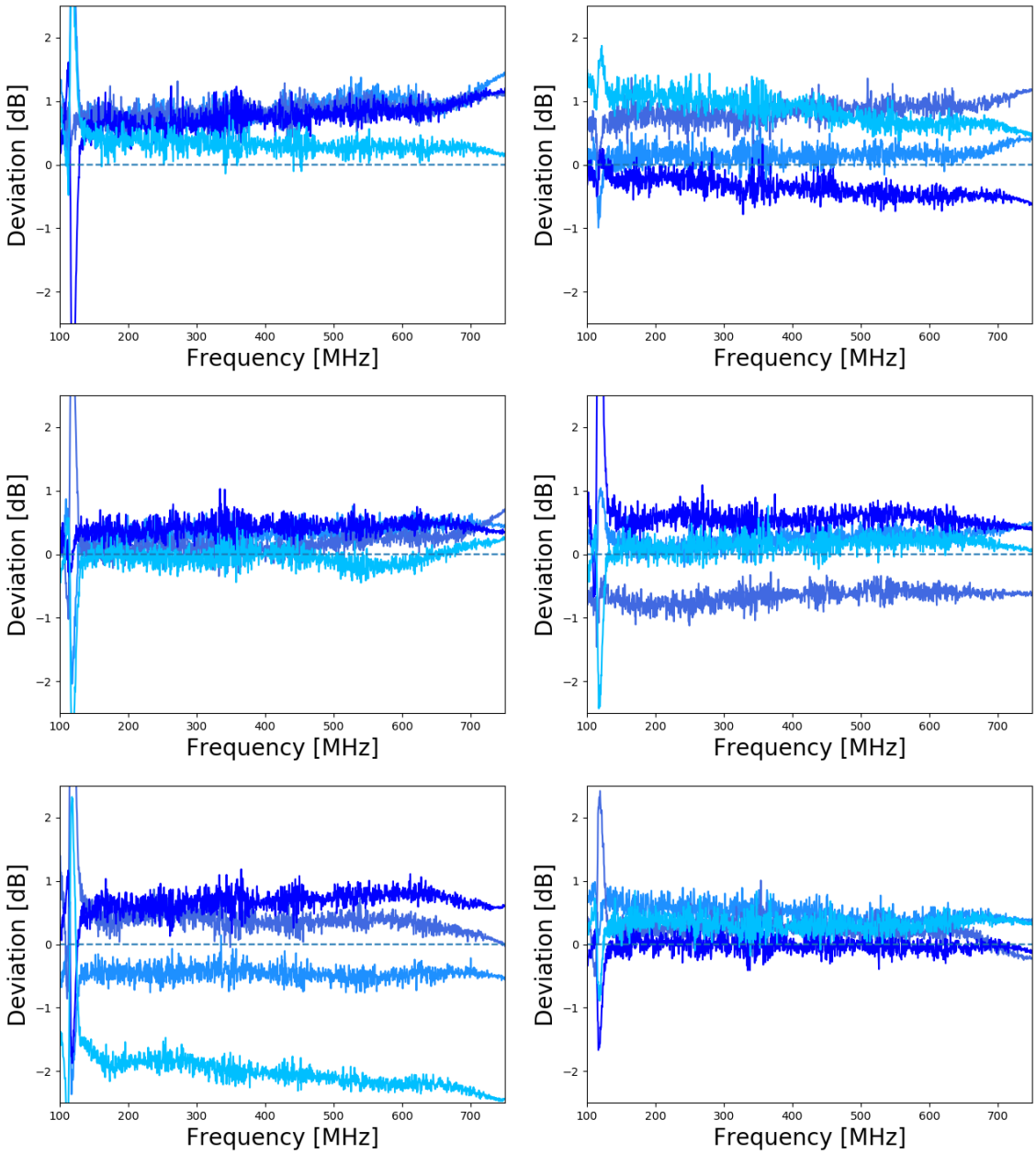

Figure 6.12: Deviation from the average [dB]: Board A0007-A0012.

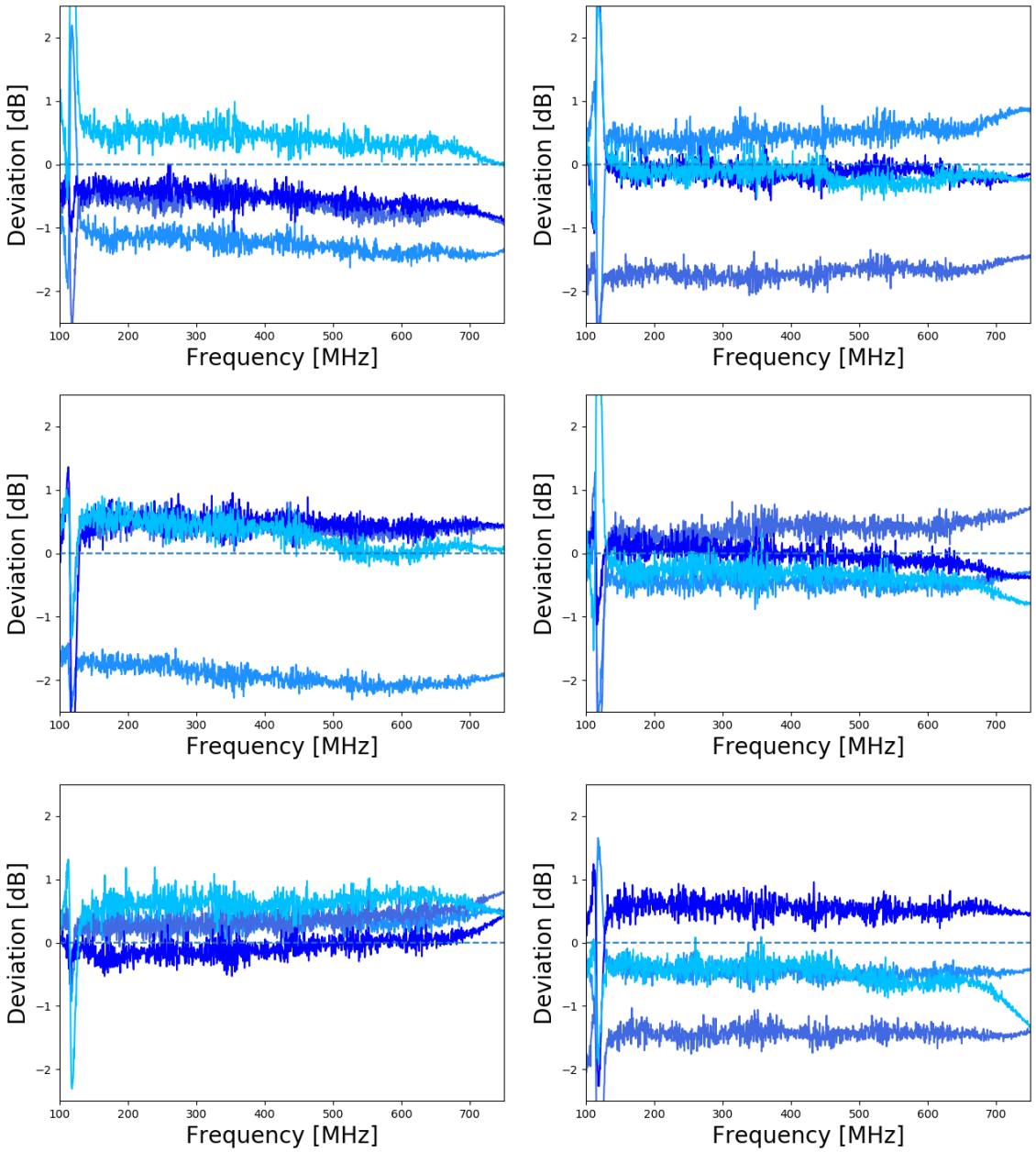

Figure 6.13: Deviation from the average [dB]: Board A0013-A0018.

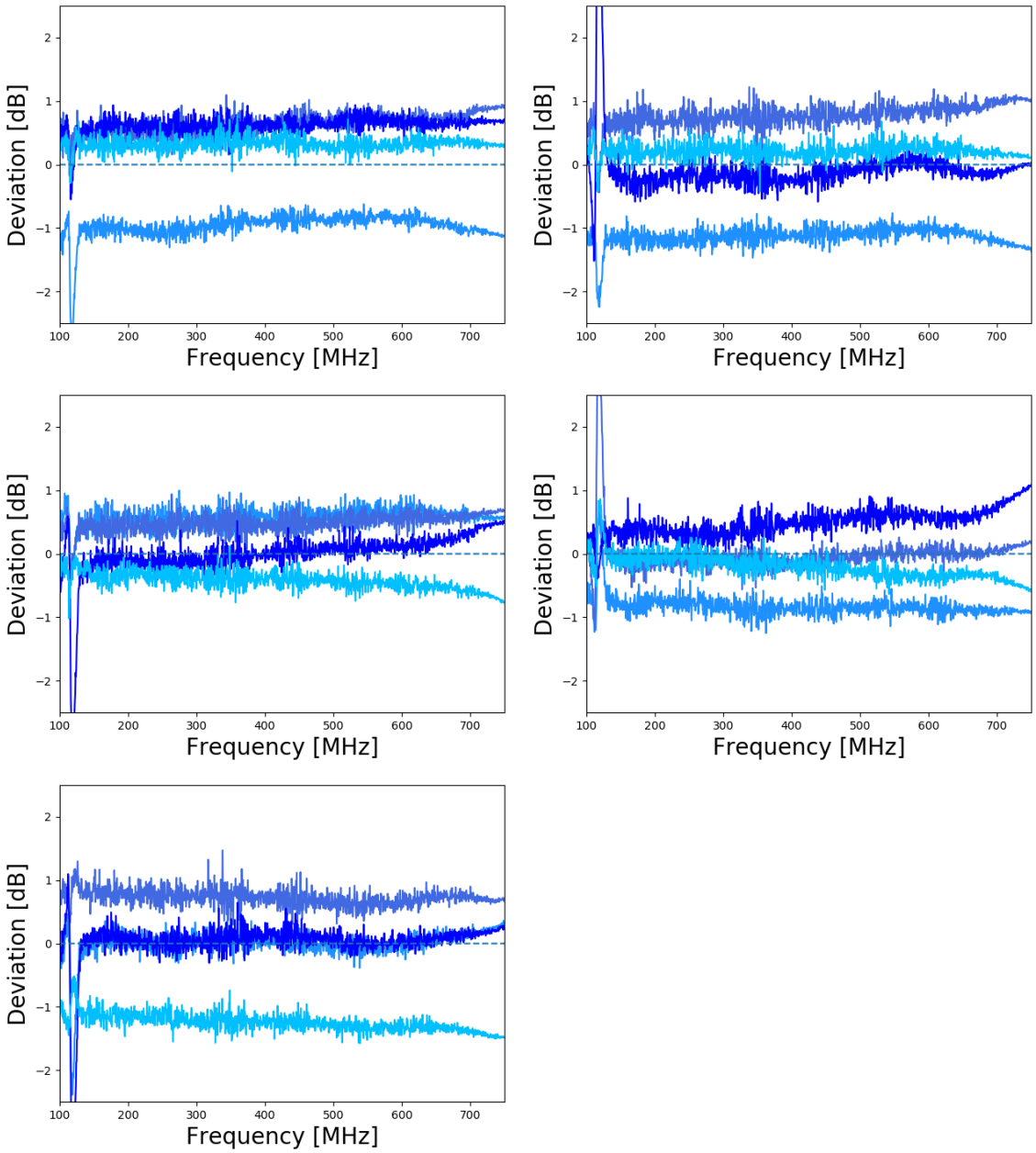

Figure 6.14: Deviation from the average [dB]: Board A0019-A0023.

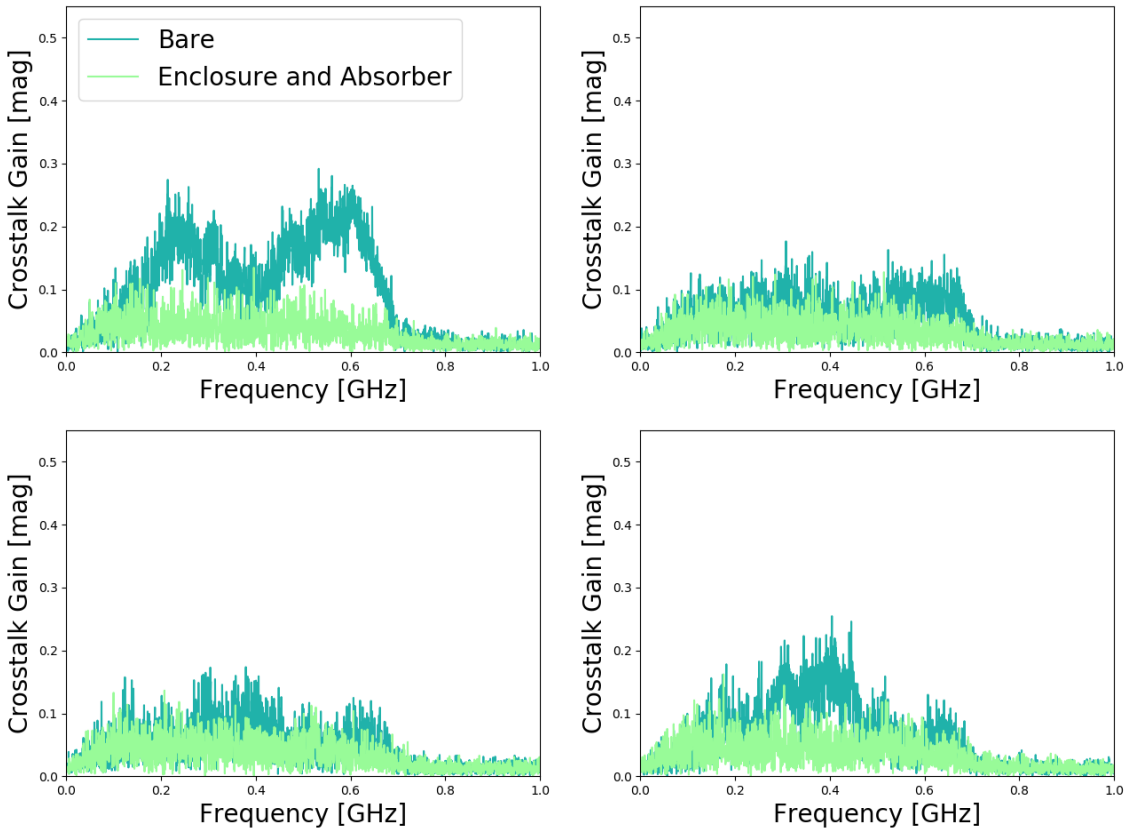

Figure 6.15: Crosstalk SURFACE board: gain measurement of channel 2, channel 3, channel 4 and channel 5. While a signal was applied to channel 1, the output of the other channels was measured.

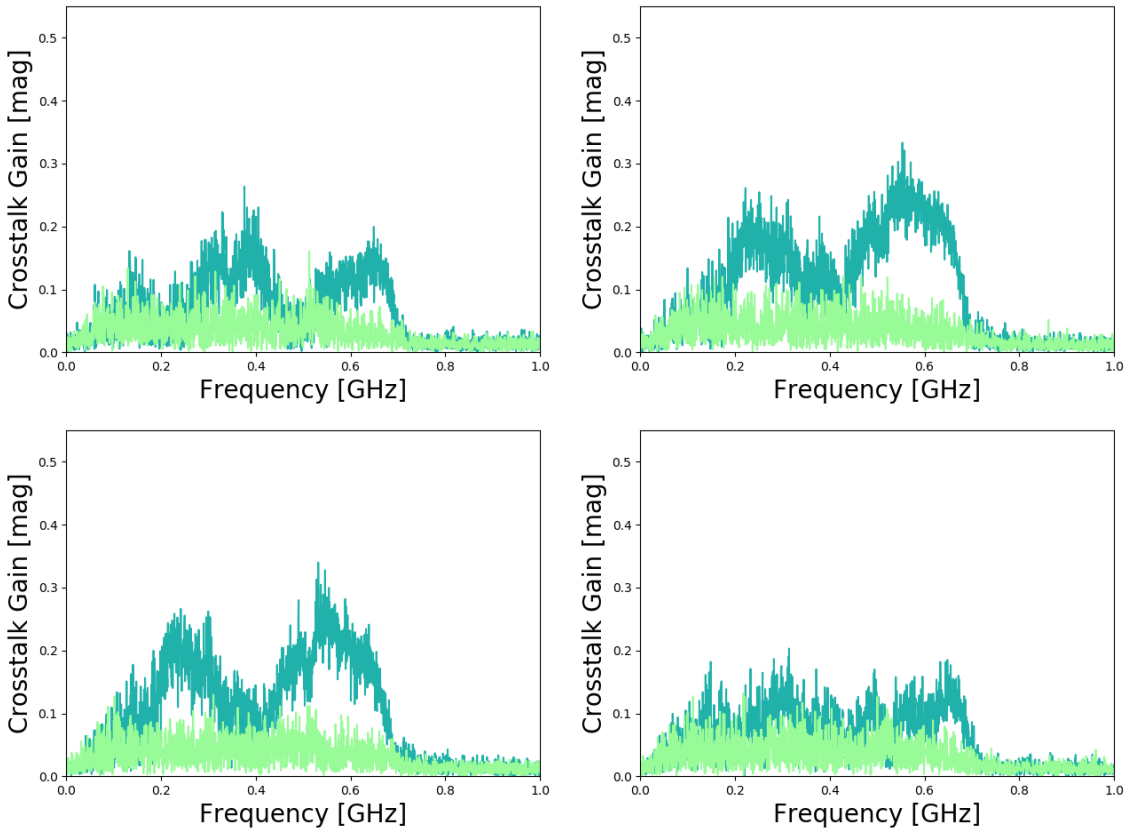

Figure 6.16: Crosstalk SURFACE board: gain measurement of channel 1, channel 2, channel 4 and channel 5. While a signal was applied to channel 3, the output of the other channels was measured.

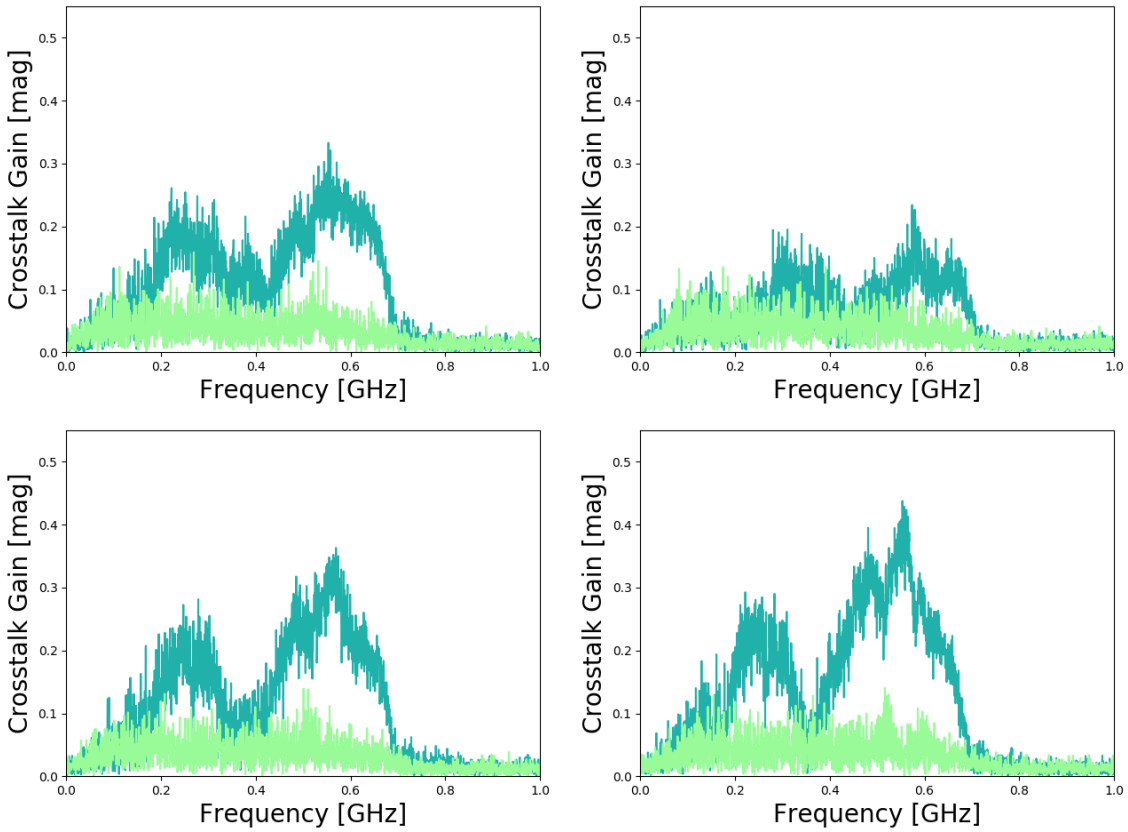

Figure 6.17: Crosstalk SURFACE board: gain measurement of channel 1, channel 2, channel 3 and channel 5. While a signal was applied to channel 4, the output of the other channels was measured.

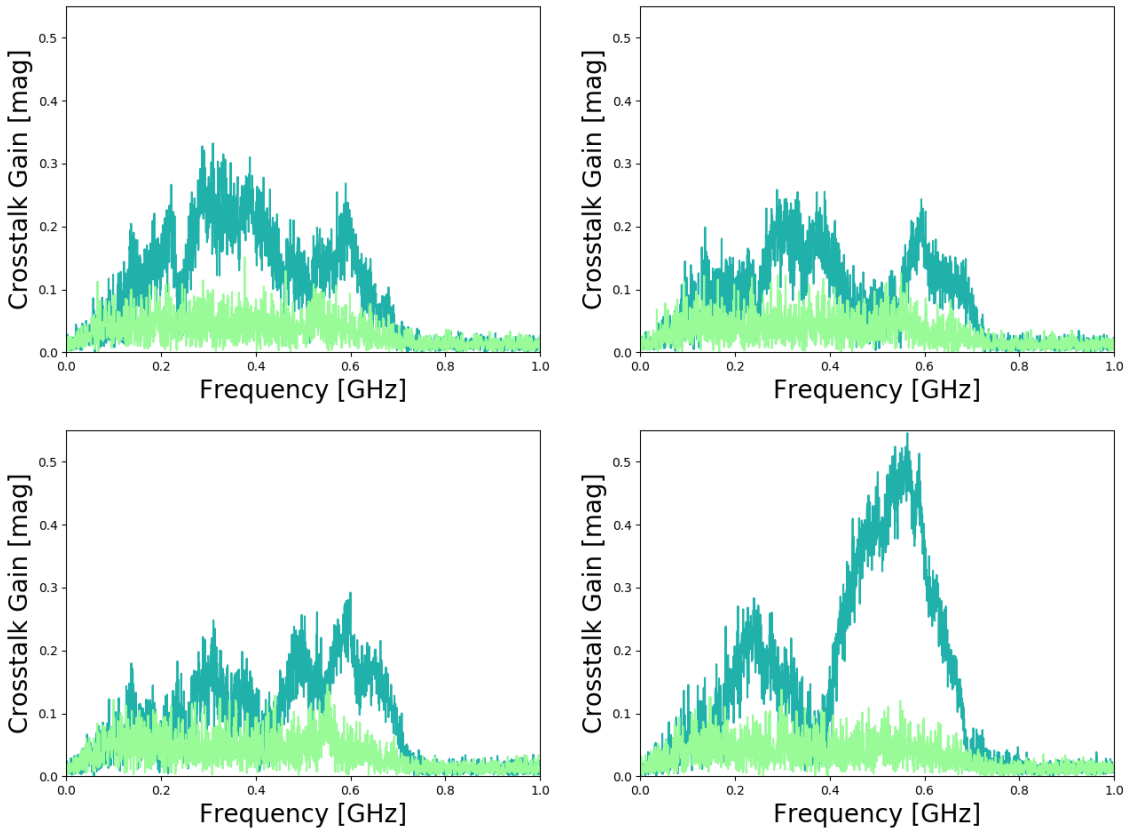

Figure 6.18: Crosstalk SURFACE board: gain measurement of channel 1, channel 2, channel 3 and channel 4. While a signal was applied to channel 5, the output of the other channels was measured.

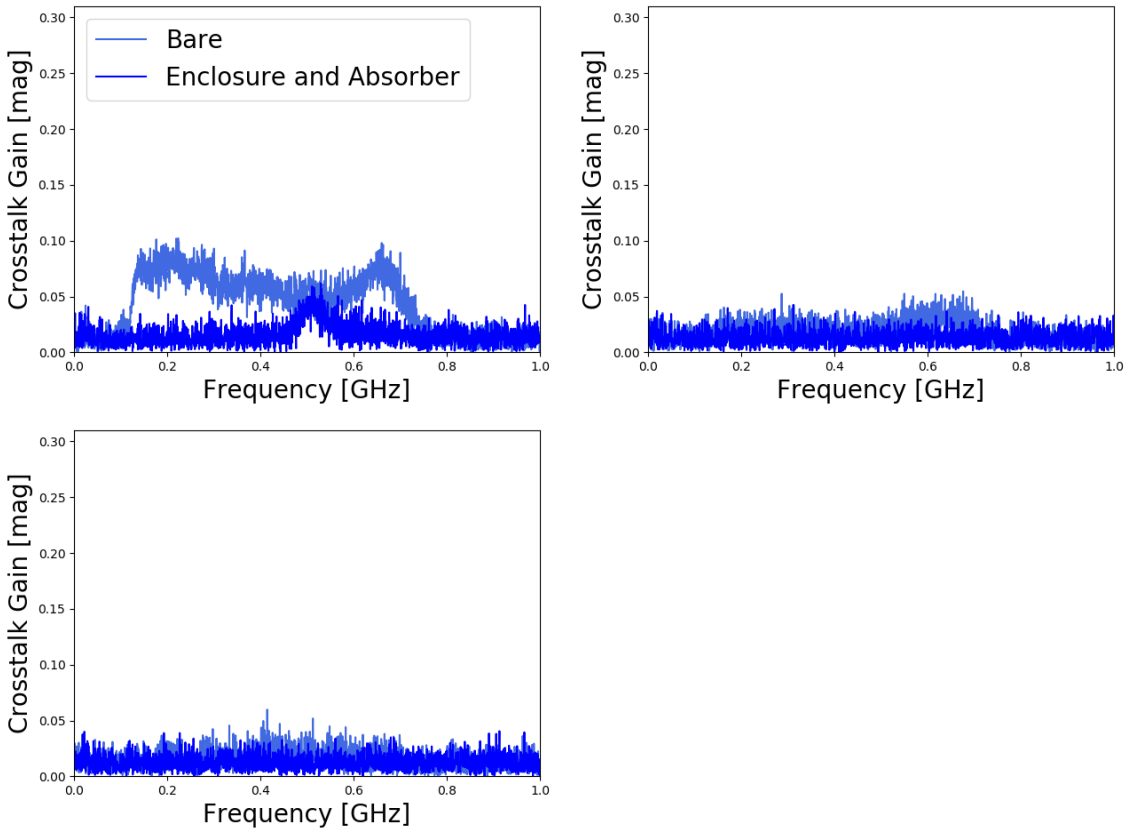

Figure 6.19: Crosstalk DRAB: gain measurement of channel 2, channel 3 and channel 4. While a signal was applied to channel 1, the output of the other channels was measured.

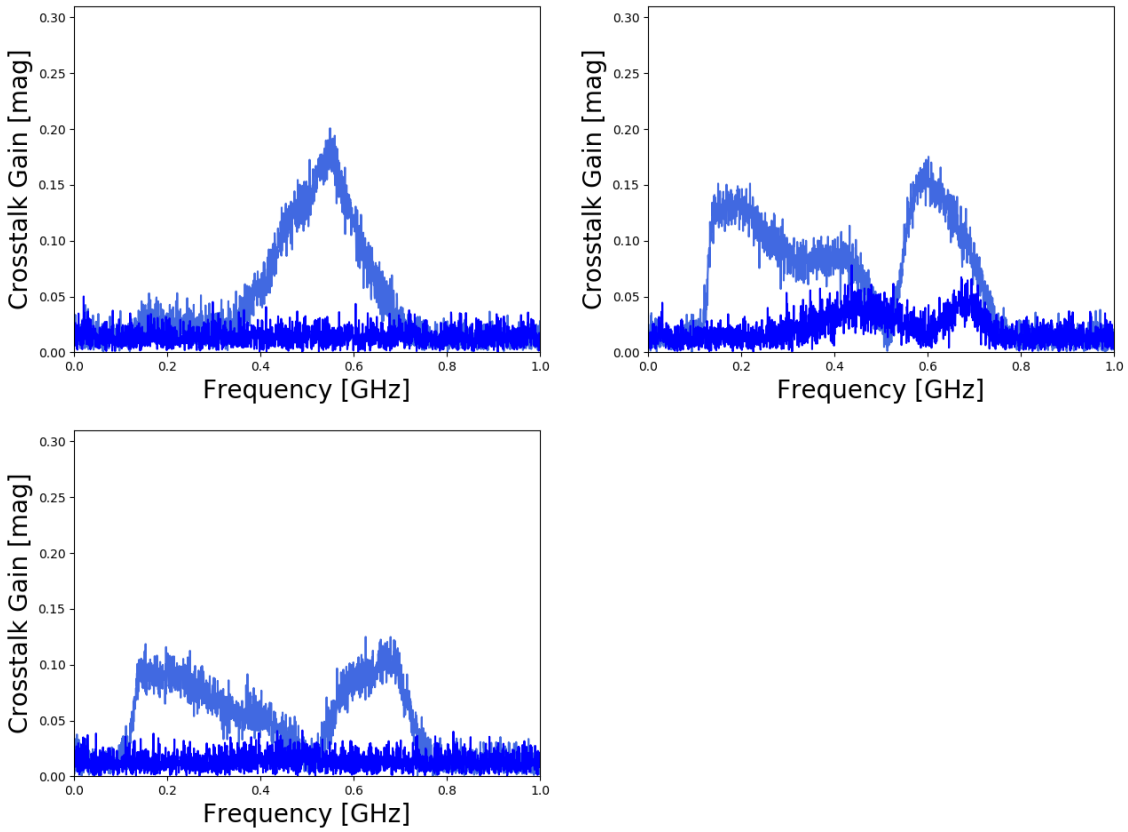

Figure 6.20: Crosstalk DRAB: gain measurement of channel 1, channel 2 and channel 4. While a signal was applied to channel 3, the output of the other channels was measured.

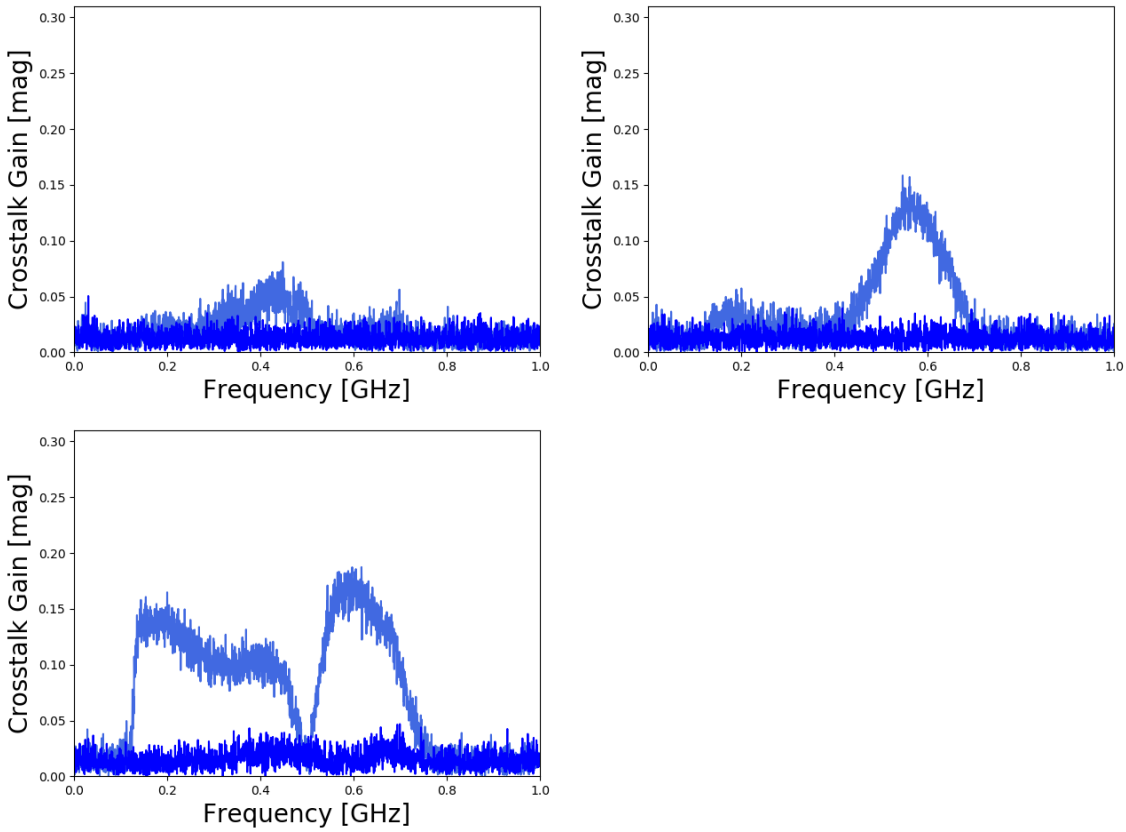

Figure 6.21: Crosstalk DRAB: gain measurement of channel 1, channel 2 and channel 3. While a signal was applied to channel 4, the output of the other channels was measured.

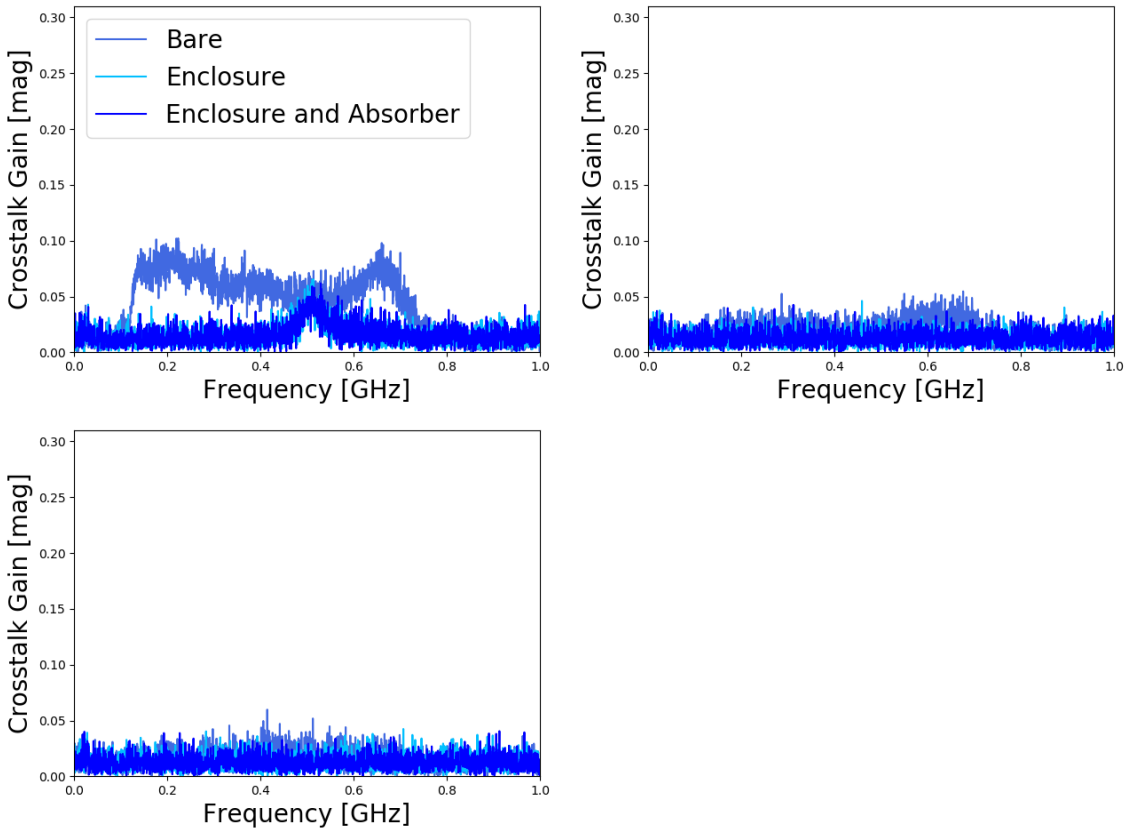

Figure 6.22: Crosstalk DRAB, absorber test: gain measurement of channel 2, channel 3 and channel 4. While a signal was applied to channel 1, the output of the other channels was measured.

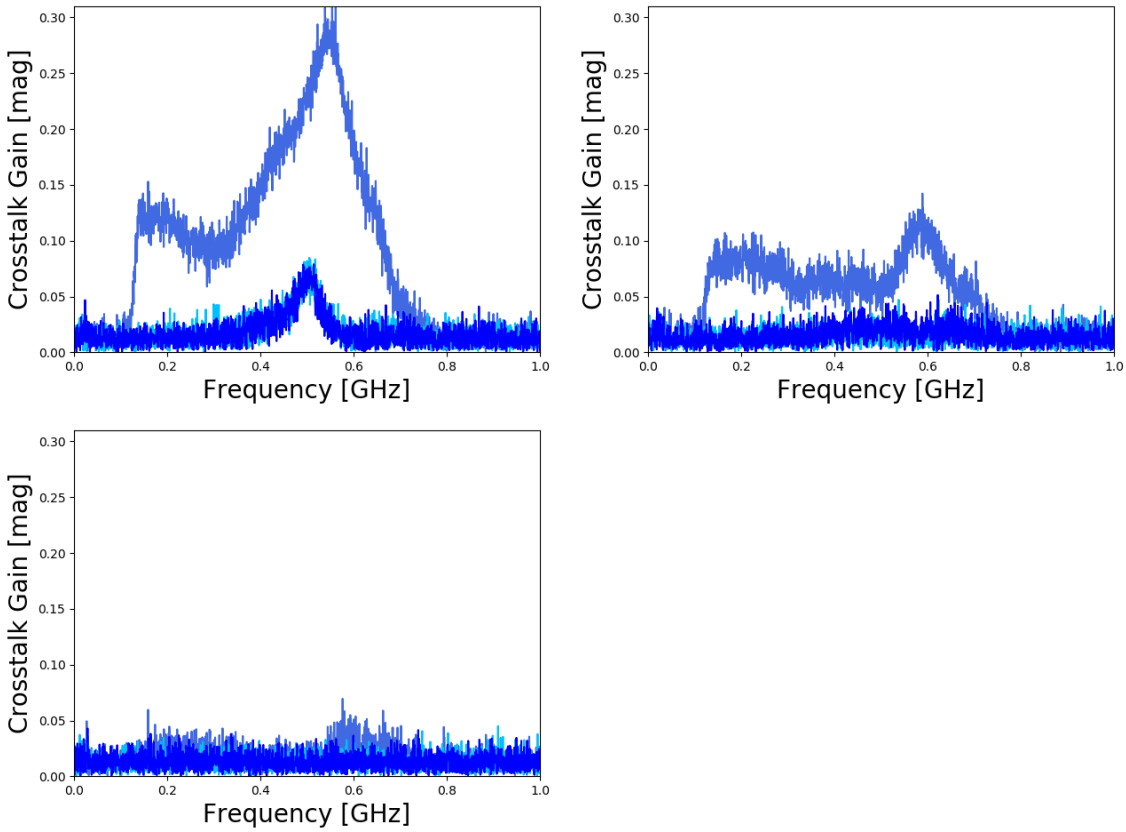

Figure 6.23: Crosstalk DRAB, absorber test: gain measurement of channel 1, channel 3 and channel 4. While a signal was applied to channel 2, the output of the other channels was measured.

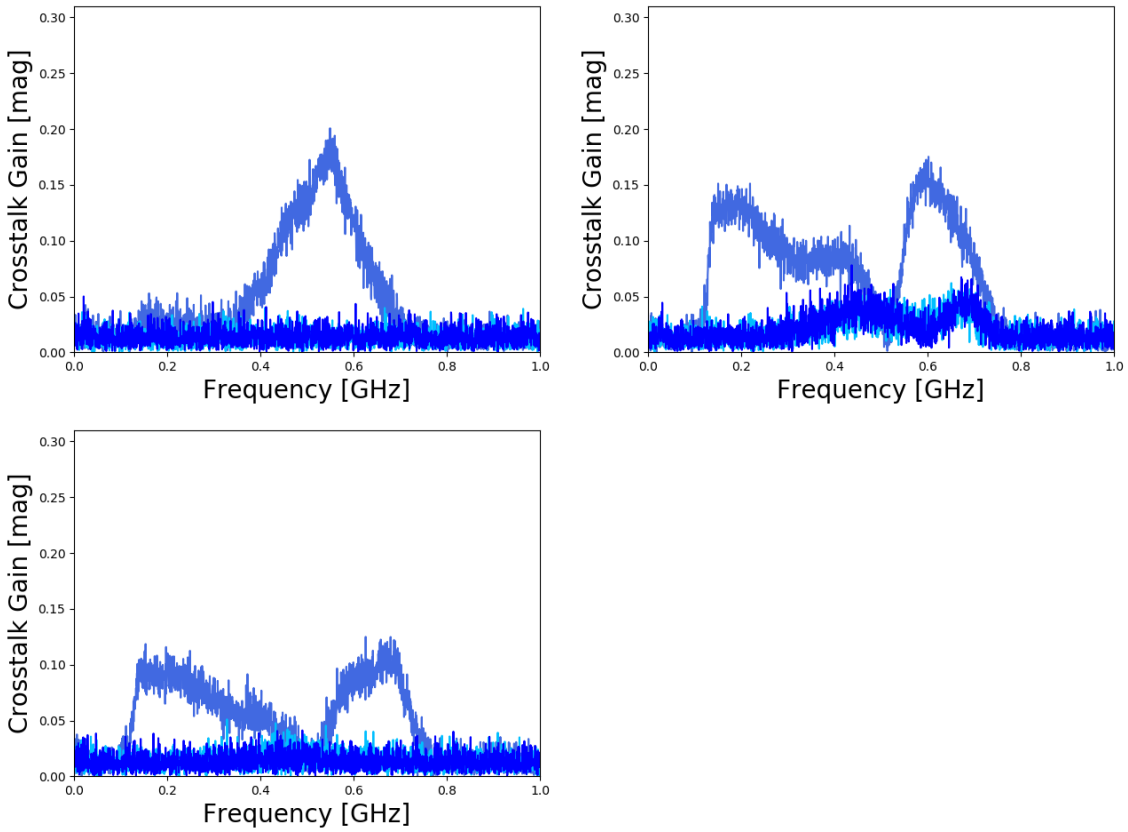

Figure 6.24: Crosstalk DRAB, absorber test: gain measurement of channel 1, channel 2 and channel 4. While a signal was applied to channel 3, the output of the other channels was measured.

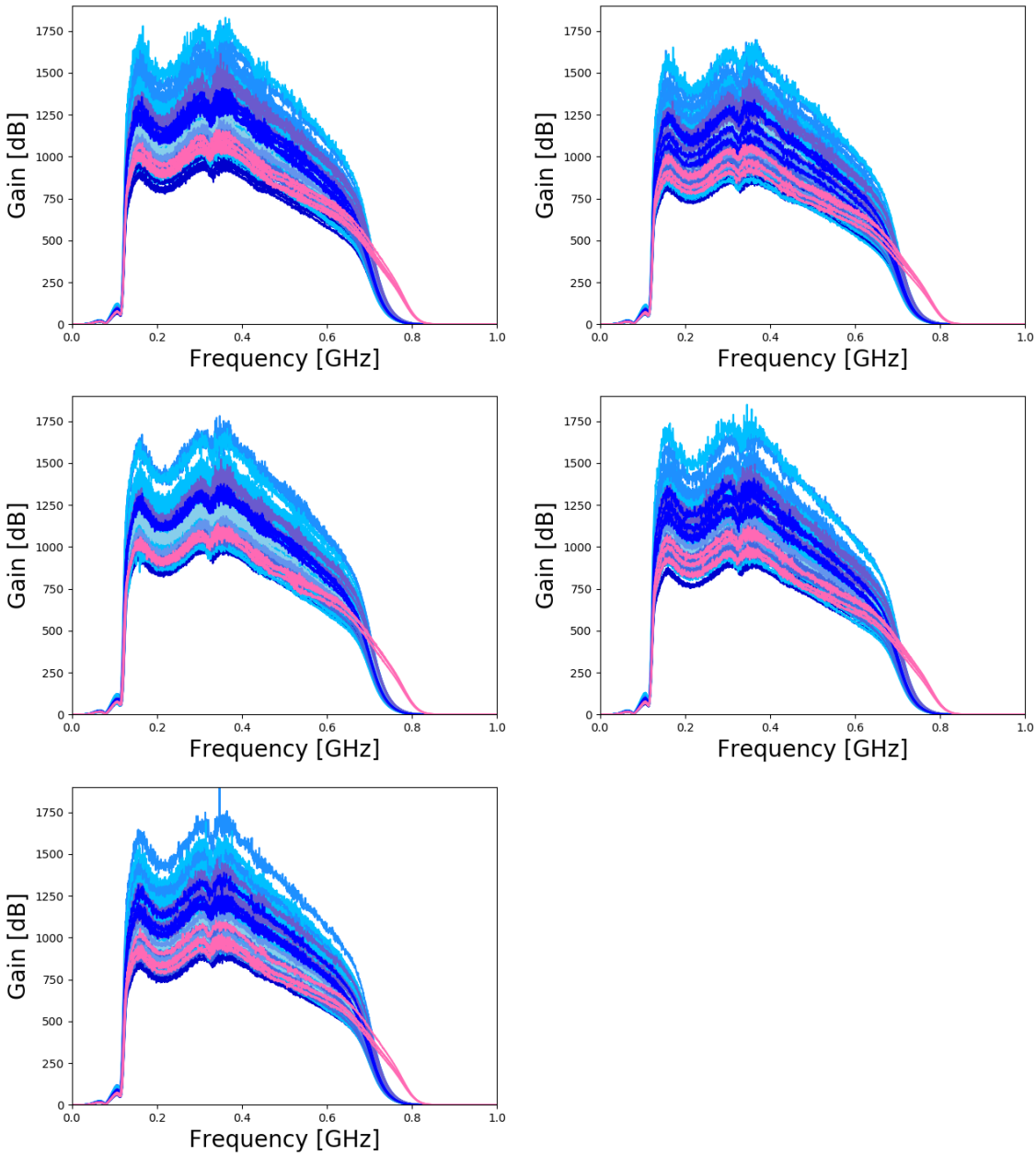

Figure 6.25: IGLU influence on measured gain [mag]. Gain of five different DRABs measured with all IGLU boards displayed in linear form. In pink the only IGLU to have a higher low-pass cutoff.

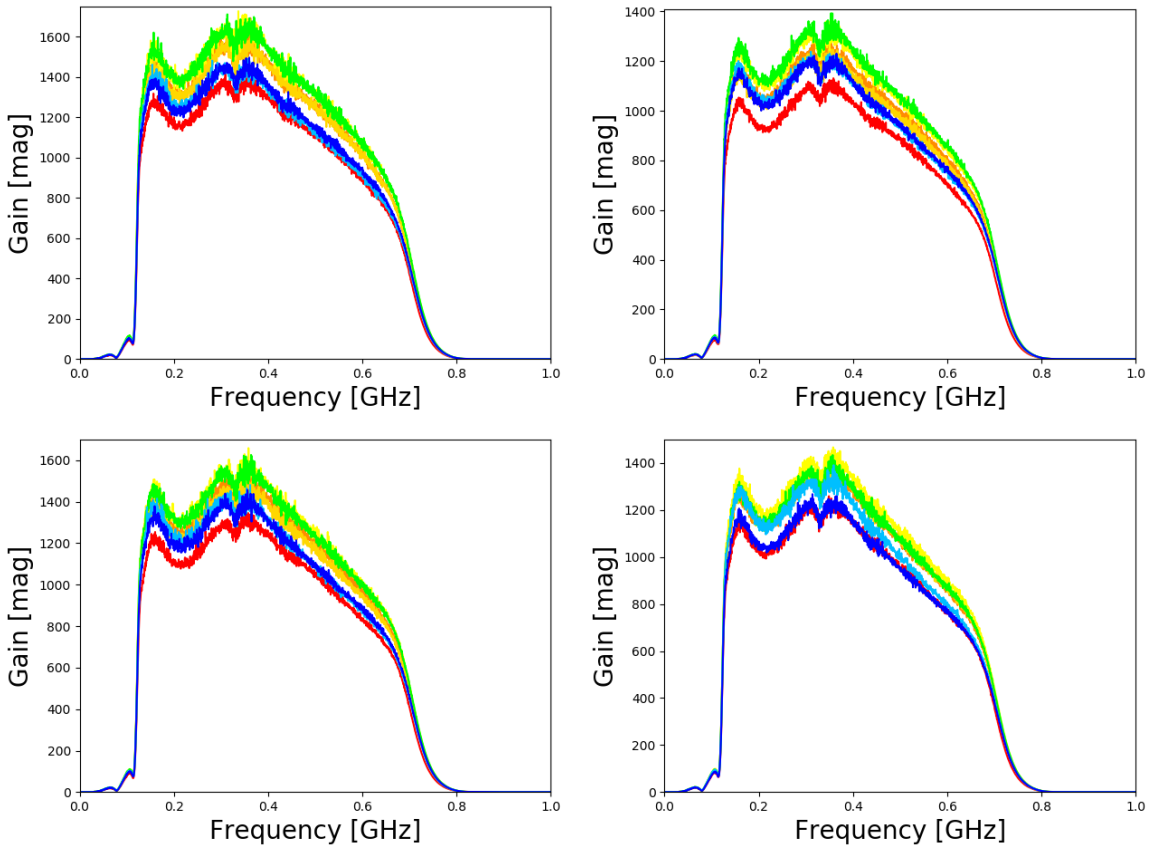

Figure 6.26: Gain measurements of all channels of one DRAB (DRAB A0003) while the IGLU was cooled down to different temperatures and the DRAB and fiber stayed outside the temperature chamber.

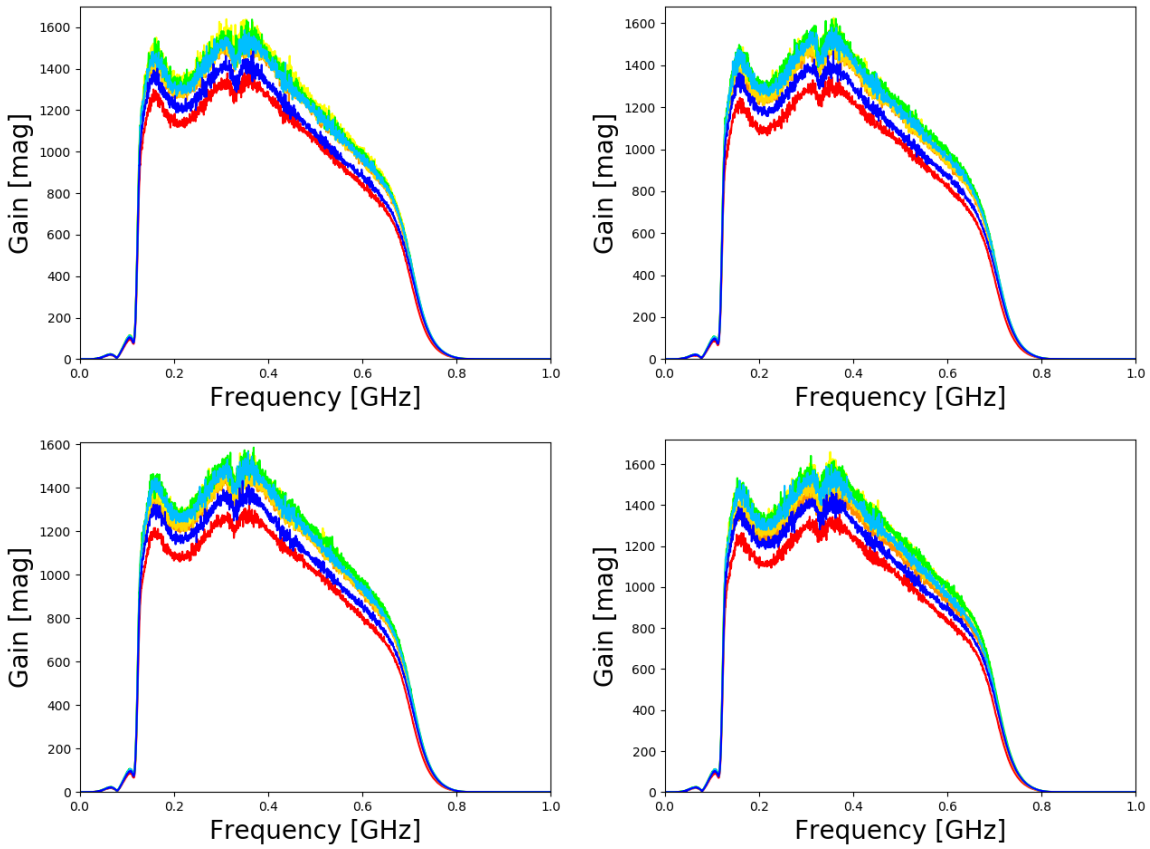

Figure 6.27: Gain measurements of all channels of one DRAB (DRAB A0012) while the IGLU was cooled down to different temperatures and the DRAB and fiber stayed outside the temperature chamber.

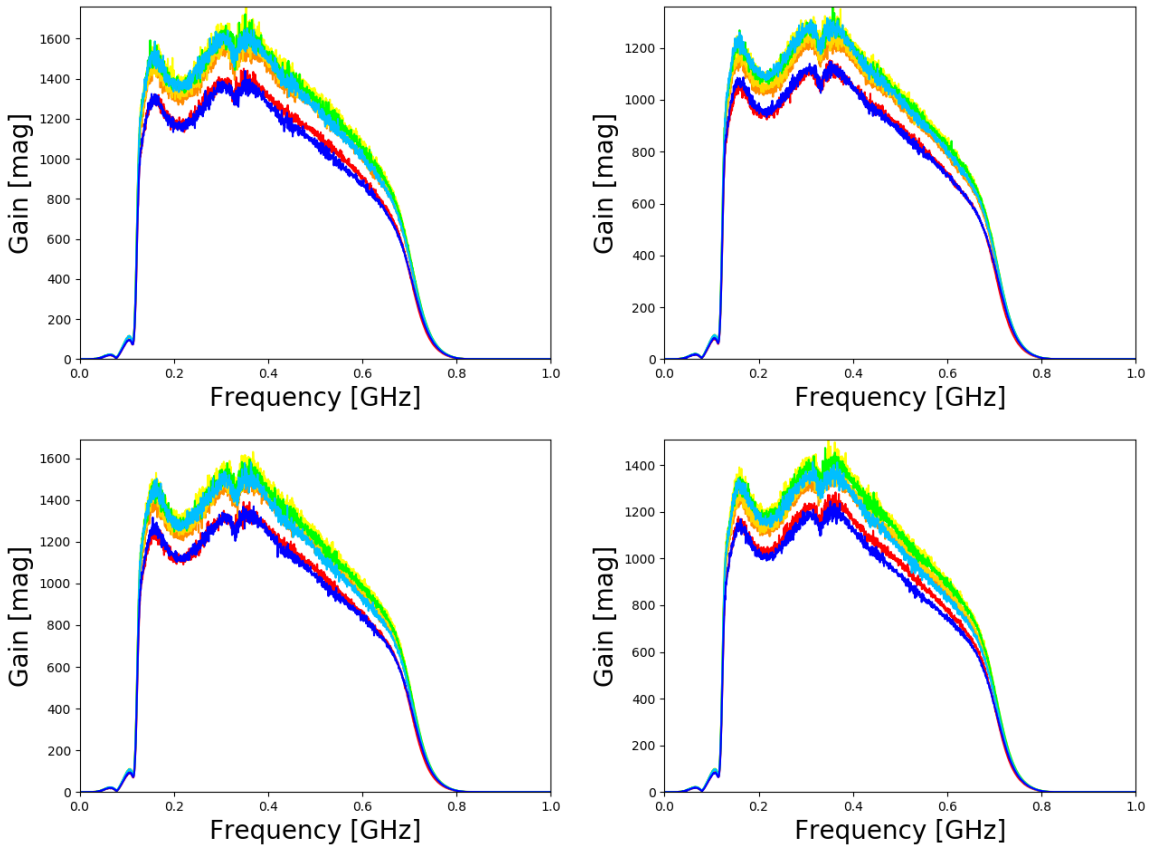

Figure 6.28: Gain measurements of all channels of one DRAB (DRAB A0003) while the IGLU and the fiber was cooled down to different temperatures and only the DRAB stayed outside the temperature chamber.

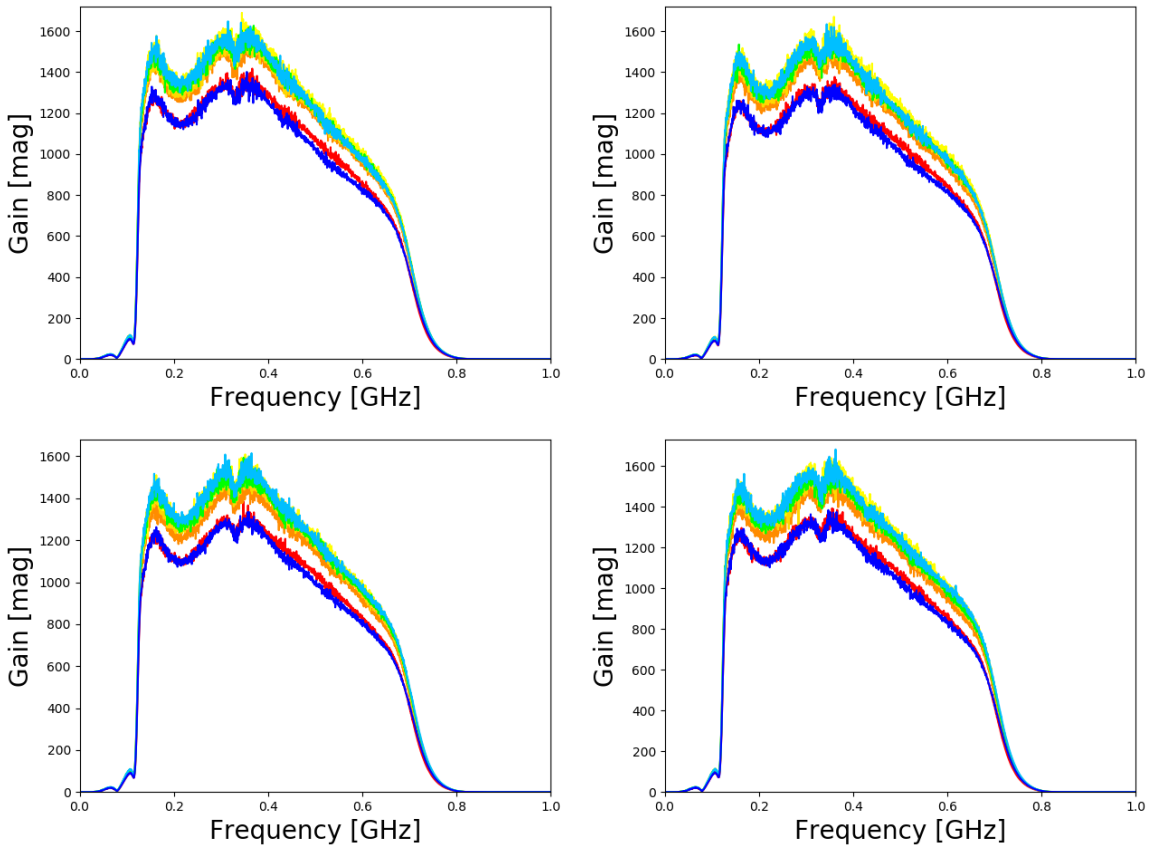

Figure 6.29: Gain measurements of all channels of one DRAB (DRAB A0012) while the IGLU and the fiber was cooled down to different temperatures and only the DRAB stayed outside the temperature chamber.

7 Bibliography

[1] G. Rajasekaran, *The Story of the Neutrino* (2016) [1606.08715].

[2] CERN, *Facts and figures about the LHC*, URL: https://home.cern/resources/faqs/facts-and-figures-about-lhc, retrieved March 19th, 2020.

[3] O. Deligny for the Pierre Auger and Telescope Array Collaborations, *The energy spectrum of ultra-high energy cosmic rays measured at the Pierre Auger Observatory and at the Telescope Array*, *PoS* **ICRC2019** (2020) 234 [2001.08811].

[4] V. Hess, *On the Observations of the Penetrating Radiation during Seven Balloon Flights* (translated and commented by A. De Angelis and C. Arcaro b. Schultz), *Physikalische Zeitschrift* **13** (1912) 1084–1091 [1808.02927].

[5] Pierre Auger collaboration, *The Pierre Auger Observatory: Contributions to the 34th International Cosmic Ray Conference (ICRC 2015)*, *PoS* **ICRC2015** (2015) [1509.03732].

[6] H.E.S.S. Collaboration, *GRB Observations with H.E.S.S. II*, *PoS* **ICRC2017** (2017) 636 [1708.01088].

[7] IceCube collaboration, *Differential limit on the extremely-high-energy cosmic neutrino flux in the presence of astrophysical background from nine years of IceCube data*, *Phys. Rev. D* **98** (2018) 062003 [1807.01820].

[8] J. F. Beacom, N. F. Bell, D. Hooper, S. Pakvasa and T. J. Weiler, *Decay of High-Energy Astrophysical Neutrinos*, *Phys. Rev. Lett.* **90** (2003) 181301 [hep-ph/0211305].

[9] M. Bustamante, J. F. Beacom and W. Winter, *Theoretically palatable flavor combinations of astrophysical neutrinos*, *Phys. Rev. Lett.* **115** (2015) 161302 [1506.02645].

[10] A. Cooper-Sarkar, P. Mertsch and S. Sarkar, *The high energy neutrino cross-section in the Standard Model and its uncertainty*, *JHEP* **08** (2011) 042 [1106.3723].

[11] D. Hooper, D. Morgan and E. Winstanley, *Lorentz and CPT invariance violation in high-energy neutrinos*, *Phys. Rev. D* **72** (2005) 065009 [hep-ph/0506091].

[12] J. L. Feng, *Dark Matter Candidates from Particle Physics and Methods of Detection*, *Ann. Rev. Astron. Astrophys.* **48** (2010) 495 [1003.0904].

[13] K. Ioka and K. Murase, *IceCube PeV–EeV neutrinos and secret interactions of neutrinos*, *PTEP2014* (2014) 061E01 [1404.2279].

[14] A. Connolly and A. G. Vieregg, *Radio Detection of High Energy Neutrinos*, *Neutrino Astronomy - Current Status, Future Prospects, Eds. T. Gaisser and A. Karle (World Scientific)* (2017) 217 [1607.08232].

[15] Liverpool Telescope, MAGIC, H.E.S.S., AGILE, Kiso, VLA/17B-403, INTEGRAL, Kapteyn, Subaru, HAWC, Fermi-LAT, ASAS-SN, VERITAS, Kanata, IceCube, Swift NuSTAR collaboration, *Multimessenger observations of a flaring blazar coincident with high-energy neutrino IceCube-170922A*, *Science* **361** (2018) eaat1378 [1807.08816].

[16] IceCube collaboration, *Neutrino emission from the direction of the blazar TXS 0506+056 prior to the IceCube-170922A alert*, *Science* **361** (2018) 147 [1807.08794].

[17] D. Petry for the MAGIC Telescope collaboration, *The MAGIC Telescope - Prospects for GRB research*, *Astron. Astrophys. Suppl. Ser.* **138** (1999) 601 [astro-ph/9904178].

[18] P.Michelson et al., *Fermi Gamma-ray Space Telescope: High-Energy Results from the First Year*, *Rept. Prog. Phys.* **73**: 074901 (2010) [1011.0213].

[19] IceCube collaboration, *Observation and Characterization of a Cosmic Muon Neutrino Flux from the Northern Hemisphere using six years of IceCube data*, *Astrophys. J.* **833** (2016) 3 [1607.08006].

[20] Fermi-LAT collaboration, *The spectrum of isotropic diffuse gamma-ray emission between 100 MeV and 820 GeV*, *Astrophys. J.* **799** (2015) 86 [1410.3696].

[21] RNO-G collaboration, *Design and Sensitivity of the Radio Neutrino Observatory in Greenland (RNO-G)* to be submitted for *JINST* (2020) [2010.12279].

[22] J. Cronin, T. Gaisser and S. Swordy, *Cosmic Rays at the Energy Frontier*, *Scientific American* (1997).

[23] J. Blümer, R. Engel and J. R. Hörandel, *Cosmic rays from the knee to the highest energies*, *Progress in Particle and Nuclear Physics* **63** (2009), 293–338. [0904.0725].

[24] D. Allard, E. Parizot and A. V. Olinto, *On the transition from galactic to extragalactic cosmic-rays: Spectral and composition features from two opposite scenarios*, *Astroparticle Physics* **27** (2007), pp. 61–75. [astro-ph/0512345].

[25] A. Palladino, M. Spurio and F. Vissani, *Neutrino telescopes and high-energy cosmic neutrinos*, *Universe* (2020), 6(2), 30 [2009.01919].

[26] O. Pisanti, *Astrophysical neutrinos: theory*, *Journal of Physics: Conference Series* **1263** Number 1 (2019) [1906.12258].

[27] V. Beresinsky and G. Zatsepin, *Cosmic rays at ultra high energies (neutrino?)*, *Phys. Lett. B* **28** (1969) 423.

[28] K. Fang et al., *Testing the Newborn Pulsar Origin of Ultrahigh Energy Cosmic Rays with EeV Neutrinos*, *Phys. Rev. D* **90** (2014) 103005 [1311.2044].

[29] K. Murase, Y. Inoue and C. D. Dermer, *Diffuse Neutrino Intensity from the Inner Jets of Active Galactic Nuclei: Impacts of External Photon Fields and the Blazar Sequence*, *Phys. Rev. D* **90** (2014) 023007 [1403.4089].

[30] D. Boncioli, D. Biehl and W. Winter, *On the common origin of cosmic rays across the ankle and diffuse neutrinos at the highest energies from low-luminosity Gamma-Ray Bursts*, *Astrophys. J.* **872** (2019) 110 [1808.07481].

[31] K. Murase, *High energy neutrino early afterglows gamma-ray bursts revisited*, *Phys. Rev. D* **76** (2007) 123001 [0707.1140].

[32] C. Righi, A. Palladino, F. Tavecchio and F. Vissani, *EeV Astrophysical neutrinos from FSRQs?*, accepted at *AA* (2020) [2003.08701].

[33] K. Fang and K. Murase, *Linking High-Energy Cosmic Particles by Black-Hole Jets Embedded in Large-Scale Structures*, *Nature Phys.* **14** (2018) 396 [1704.00015].

[34] X. Rodrigues, J. Heinze, A. Palladino, A. van Vliet and W. Winter, *Blazar origin of the UHECRs and perspectives for the detection of astrophysical source neutrinos at EeV energies* (2020) [2003.08392].

[35] IceCube collaboration, *Probing the origin of cosmic-rays with extremely high energy neutrinos using theIceCube Observatory*, *Phys. Rev. D* **88** (2013) 112008 [1310.5477].

[36] A. Müller, *GZK-cutoff*, *Spektrum der Wissenschaft: Lexikon der Astronomie* (2014).

[37] CERNCOURIER, *Event view of highest energy neutrino detected by IceCube*, September 25th, 2015.

[38] K. Greisen, *End to the Cosmic-Ray Spectrum?*, *Phys. Rev. Lett. 16*, 748 (1966).

[39] G. Zatsepin and V. Kuzmin, *Upper Limit of the Spectrum of Cosmic Rays*, *JETP Letters* **4**, p.78 (1966).

[40] M. Ahlers and F. Halzen, *Minimal cosmogenic neutrinos*, *Phys. Rev. D* **86** (2012) 083010 [1208.4181].

[41] D. Bergmann for the Telescope Array Collaboration, *Combined fit of the spectrum and composition from telescope array*, *PoS* **ICRC2019** (2019) 190.

[42] Pierre Auger collaboration, *Combined fit of spectrum and composition data as measured by the Pierre Auger Observatory*, *JCAP 2017* (2017) 038 [1612.07155].

[43] O. Deligny for the Pierre Auger and Telescope Array Collaborations, *Telescope Array collaboration, The energy spectrum of ultra-high energy cosmic rays measured at the Pierre Auger Observatory and at the Telescope Array*, *PoS* **ICRC2019** (2020) 234 [2001.08811].

[44] A. van Vliet, R. Alves Batista and J. R. Hörandel, *Determining the fraction of cosmic-ray protons at ultra high energies with cosmogenic neutrinos*, *Phys. Rev. D* **100** (2019) 021302 [1901.01899].

[45] M. Ackermann et al., *Fundamental physics with high-energy cosmic neutrinos*, *Bull. Am. Astron. Soc.* **51** (2019) 215 [1903.04333].

[46] G. Askar'yan, *Excess negative charge of an electron-photon shower and its coherent radio emission*, *Sov. Phys. JETP* **14** (1962) 441.

[47] D. Saltzberg et al., *Observation of the Askaryan effect: Coherent microwave Cherenkov emission from charge asymmetry in high-energy particle cascades*, *Phys. Rev. Lett.* **86** (2001) 2802 [hep-ex/0011001].

[48] P. W. Gorham et al., *Accelerator measurements of the Askaryan effect in rock salt: A Road map toward teraton underground neutrino detectors*, *Phys. Rev. D* **72** (2005) 023002 [astro-ph/0412128].

[49] ANITA collaboration, *Observations of the Askaryan effect in ice*, *Phys. Rev. Lett.* **99** (2007) 171101 [hep-ex/0611008].

[50] Pierre Auger collaboration, *Probing the radio emission from air showers with polarization measurements*, *Phys. Rev. D* **89** (2014) 052002 [1402.3677].

[51] J. Alvarez-Munizet et al., *Askaryan radiation from neutrino-induced showers in ice*, Accepted in *Phys. Rev. D* (2020) [2003.09705].

[52] D. García-Fernández, C. Glaser and A. Nelles, The signatures of secondary leptons in radio-neutrino detectors in ice (2020) [2003.13442].

[53] C. James et al., *The lunar Askaryan technique with the Square Kilometre Array*, *PoS* **ICRC2015** (2015) 291 [1608.02408].

[54] E. Zas, F. Halzen and T. Stanev, *Electromagnetic pulses from high-energy showers: Implications for neutrino detection*, *Phys. Rev. D* **45** (1992) 362.

[55] ARA collaboration, *Design and Initial Performance of the Askaryan Radio Array Prototype EeV Neutrino Detector at the South Pole*, *Astropart. Phys.* **35** (2012) 457 [1105.2854].

[56] ANITA collaboration, *In situ radioglaciological measurements near Taylor Dome, Antarctica and implications for UHE neutrino astronomy*, *Astropart. Phys.* **29** (2008) 130 [astro-ph/0703413].

[57] J. Avva et al., *An in situ measurement of the radio-frequency attenuation in ice at Summit Station, Greenland*, *J. Glaciol.* **61** (2015) 1005 [1409.5413].

[58] K. Fang and B. D. Metzger, *High-Energy Neutrinos from Millisecond Magnetars formed from the Merger of Binary Neutron Stars*, *Astrophys. J.* **849** (2017) 153 [1707.04263].

[59] S. S. Kimura, K. Murase, I. Bartos, K. Ioka, I. S. Heng and P. Mészáros, *Transejecta high-energy neutrino emission from binary neutron star mergers*, *Phys. Rev. D* **98** (2018) 043020 [1805.11613].

[60] C. Lunardini and W. Winter, *High Energy Neutrinos from the Tidal Disruption of Stars*, *Phys. Rev. D* **95** (2017) 123001 [1612.03160].

[61] D. Biehl et al., *Tidally disrupted stars as a possible origin of both cosmic rays and neutrinos at the highest energies*, *Sci. Rep.* **8** (2018) 10828 [1711.03555].

[62] A. Ishihara for the IceCube collaboration, *The IceCube Upgrade – Design and Science Goals*, *PoS* **ICRC2019** (2020) 1031 [1908.09441].

[63] RICE collaboration, *Performance and simulation of the RICE detector*, *Astropart. Phys.* **19** (2003) 15 [astro-ph/0112372].

[64] I. Kravchenko et al., *RICE limits on the diffuse ultrahigh energy neutrino flux*, *Phys. Rev. D* **73** (2006) 082002 [astro-ph/0601148].

[65] ARIANNA collaboration, *A First Search for Cosmogenic Neutrinos with the ARIANNA Hexagonal Radio Array*, *Astropart. Phys.* **70** (2015) 12 [1410.7352].

[66] ARIANNA collaboration, *Performance of the ARIANNA Hexagonal Radio Array*, *PoS* **ICRC2015** (2016) 1149 [1509.00109].

[67] ANITA collaboration, *The Antarctic Impulsive Transient Antenna Ultra-high Energy Neutrino Detector Design, Performance, and Sensitivity for 2006-2007 Balloon Flight*, *Astropart. Phys.* **32** (2009) 10 [0812.1920].

[68] ANITA collaboration, *Observational Constraints on the Ultra-high Energy Cosmic Neutrino Flux from the Second Flight of the ANITA Experiment*, *Phys. Rev. D* **82** (2010) 022004 [1003.2961].

[69] ARA collaboration, *Performance of two Askaryan Radio Array stations and first results in the search for ultrahigh energy neutrinos*, *Phys. Rev. D* **93** (2016) 082003 [1507.08991].

[70] ARA collaboration, *Constraints on the Diffuse Flux of Ultra-High Energy Neutrinos from Four Years of Askaryan Radio Array Data in Two Stations*, *Phys. Rev. D* **102**, 043021 (2020) [1912.00987].

[71] F. D. Kahn and I. Lerche, *Radiation from cosmic ray air showers*, *Proceedings of the Royal Society* **A289** (1966).

[72] H. Allan, *Low frequency radio emission from extensive air showers*, *Nature* **237** (1972) 384.

[73] ARA collaboration, *First Constraints on the Ultra-High Energy Neutrino Flux from a Prototype Station of the Askaryan Radio Array*, *Astropart. Phys.* **70** (2015) 62 [1404.5285].

[74] keysight technologies, *S-Parameter Measurements - Basics for High Speed Digital Engineers* (2019).

[75] Ian Poole for electronic-notes.com, *What is a Vector Network Analyzer, VNA: the basics*, URL: https://www.electronics-notes.com/articles/test-methods/rf-vector-network-analyzer-vna/what-is-a-vna.php, retrieved November 1st, 2020.

[76] Anne Marie Helmenstine for thoughtCo.com, *Random Error vs. Systematic Error - Two Types of Experimental Error*, URL: https://www.thoughtco.com/random-vs-systematic-error-4175358, retrieved November 1st, 2020.

[77] keysight technologies, *Measurement Errors*, URL: http://na.support.keysight.com/vna/help/latest/S3_Cals/Errors.htm, retrieved November 1st, 2020.

[78] Microwaves101.com, *S-parameters*, URL: https://www.microwaves101.com/encyclopedias/s-parameters, retrieved November 1st, 2020.

[79] Joseph Creech for Analog Dialogue, *S-Parameters Allow High-Frequency Verification of RF Switch Models*, URL: https://www.analog.com/en/analog-dialogue/articles/s-parameters-allow-hi-freq-verification.html, retrieved November 1st, 2020.

[80] keysight technologies, *Network Analyzer Basics*, retrieved November 2nd, 2020.

[81] Franz Sischka, *Basics of S-Parameters* (2002).

[82] keysight technologies, *Small Signal Gain and Flatness*, URL: http://na.support.keysight.com/pna/help/latest/Tutorials/Gain_Flat.htm, retrieved November 1st, 2020.

[83] allaboutcircuits.com, *Amplifier Gain: Chapter 1 - Amplifiers and Active Devices*, URL: https://www.allaboutcircuits.com/textbook/semiconductors/chpt-1/amplifier-gain/, retrieved November 2nd, 2020.

[84] Steve Arar for allaboutcircuits.com, *Design Examples of FIR Filters Using the Window Method*, URL: https://www.allaboutcircuits.com/technical-articles/design-examples-of-fir-filters-using-window-method/, retrieved November 2nd, 2020.

[85] Iowa Hills Software - Digital and Analog Filters, *What is Group Delay*, URL: http://www.iowahills.com/B1GroupDelay.html, retrieved November 2nd, 2020.

[86] keysight technologies, *Group Delay*, URL: http://na.support.keysight.com/pna/help/latest/Tutorials/Group_Delay6_5.htm, retrieved November 2nd, 2020.

[87] thefreedictionary.com, *crosstalk*, URL: https://www.thefreedictionary.com/crosstalk, retrieved November 3rd, 2020.

[88] nihtila.com, *Understanding audio measurements: Crosstalk*, URL: http://nihtila.com/2017/01/08/understanding-audio-measurements-crosstalk/, retrieved November 3rd, 2020.

[89] bldrdoc.gov, *crosstalk (XT)*, URL: https://www.its.bldrdoc.gov/fs-1037/dir-009/_1340.htm, retrieved November 3rd, 2020.

[90] electronic-notes.com, *What is Noise Figure - measurement formula*, URL: https://www.electronics-notes.com/articles/radio/radio-receiver-sensitivity/what-is-noise-figure-measurement-calculation-formula.php, retrieved November 3rd, 2020.

[91] ARIANNA collaboration, *Radio detection of air showers with the ARIANNA experiment on the Ross Ice Shelf*, *Astropart. Phys* **90** (2017) [1612.04473].

[92] Microwave101.com, *Power Amplifiers*, URL: https://www.microwaves101.com/encyclopedias/power-amplifiers, retrieved November 3rd, 2020.

[93] ARIANNA collaboration, *A First Search for Cosmogenic Neutrinos with the ARIANNA Hexagonal Radio Array*, *Astropart. Phys.* **70** (2015) 12-26 [1410.7352].

[94] isaaffik.org, *Isaaffik - the arctic gateway*, URL: https://www.isaaffik.org/summit-station, retrieved October 1st, 2020.

[95] maximintegrated.com, *Noise Figure Measurement Methods and Formulas*, URL: https://www.maximintegrated.com/en/design/technical-documents/tutorials/2/2875.html, retrieved November 1st, 2020.

Acknowledgments

The exciting journey that began six years ago when I started studying physics is now actually coming to an end. I am grateful for the help and support I have received from so many people.

First of all, I would like to thank everyone who supported me in writing this master's thesis.

Special thanks go to my supervisor Anna Nelles, to whom I would like to express my great appreciation. She never got tired of patiently answering numerous questions and finding solutions to any problem that might arise. Her dedication to her work and her passion for physics are an inspiration. One could not have wished for better and more committed support.

I would also like to thank the whole RNO-G collaboration, based in Europe and the United States, for helping me take my first steps into the world of astroparticle research. Adrian and Eric in particular helped me learn so much about hardware.

All ECAP employees and students ensured a very friendly working atmosphere. I especially enjoyed lunch and coffee breaks with Katrin, Nicole and Tim. Many thanks also to Robert, who was very supportive when I started at ECAP and answered all my questions, and to Carina for the pleasant working atmosphere in our office.

The COVID-19 pandemic is affecting all of our daily lives as I write these last sentences of my thesis. I would have preferred to spend more time discussing physics with people at ECAP in person, taking a coffee break together, or just having company while I work in the lab or office. But I also appreciate the fact that, despite some uncertainties and plan changes, I didn't have to face any serious problems. Thanks to many employees at FAU and ECAP, new concepts have been developed and support has been provided to help students like me to continue and finish their courses and theses. And at least I was able to take part in the radio group meetings, since they were now online, and I am very grateful for the warm welcome from the radio group of DESY Zeuthen: Thanks to you, I felt part of this group despite the great distance. Thank you very much, Ilse, Lilly, Christoph, Daniel, Zack and Steffen!

I will look back fondly on the many wonderful memories of the past few years at the university and on the many great people I have met. But I also have to thank my friends outside the world of science: They were understanding in times when I didn't have much time for them and they were of great help when I needed a distraction. And last but not least, to my parents and my sister: You were always there when I needed you, thank you so much for everything.

Statutory Declaration

I hereby declare that I am the sole author of this master's thesis and that I have not used any sources other than those listed in the bibliography and identified as references. I further declare that I have not submitted this thesis at any other institution in order to obtain a degree.

Erlangen, December 16th 2020

Nora Feigl